Study of relativistic effects in non-linear interaction between molecules andXUV/soft X-ray short laser pulses

Arturo Sopena Moros

THÈSE PRÉSENTÉE

POUR OBTENIR LE GRADE DE

DOCTEUR

DE L'UNIVERSITÉ DE BORDEAUX

ET

DE LA UNIVERSIDAD AUTONÓMA DE MADRID

ECOLE DOCTORALE DES SCIENCES PHYSIQUES ET DE L'INGÉNIEUR

SPÉCIALITÉ: LASERS, MATIÈRE, NANOSCIENCES

Par **Arturo SOPENA MOROS**

Etude des effets relativistes en régime d'interaction non-linéaire entre les molécules et les impulsions laser brèves dans les domaines de fréquences XUV et X mous

Sous la direction de : **Henri BACHAU**
Co-directeur : **Fernando MARTÍN GARCÍA**

Soutenue le 26 mars 2021
Membres du jury :

M. Ignacio SOLA REIJA	Directeur de Recherche à la Universidad Complutense de Madrid	Président
M. José Luis SANZ VICARIO	Directeur de Recherche à la Universidad de Antioquia	Rapporteur
M. Antonio PICÓN ÁLVAREZ	Professeur à la Universidad Autónoma de Madrid	Examinateur
M. Jérémie CAILLAT	Maître de Conference à Sorbonne Université LCPMR	Rapporteur
M. Philippe TAMARAT	Professeur à l'Université de Bordeaux LP2N	Examinateur

A mis amigos y a mi familia, porque han hecho que se note menos la distancia que nos separaba.

A Berta, por todo.

'This book was written using 100% recycled words.'

Terry Pratchet, Wyrd Sisters

UNIVERSIDAD AUTÓNOMA DE MADRID
UNIVERSITÉ DE BORDEAUX

Abstract

Study of relativistic effects in non-linear interaction between molecules and XUV/soft X-ray short laser pulses

by Arturo Sopena Moros

The development of intense XUV sources through free-electron lasers (FELs) and high-order harmonic generation (HHG) in the femtosecond (fs) and sub-fs domains provides a unique tool to investigate non-linear ultrafast laser-matter interaction. In the study of the dynamics of molecular photoionization at ultrashort timescales, the Time-Dependent Schrödinger Equation (TDSE) has been crucial for the interpretation of experimental observations. In this thesis, we present results for *ab initio* calculations of H_2 photoionization with UV/X-ray ultrashort laser pulses. We focus on the study of non-linear processes involving two photons and their role in the coupled electron-nuclear dynamics they induce and their study beyond the dipole approximation (DA).

Our theoretical approach is based on a spectral method, which requires determining the quantum states of the field-free molecule. These states are calculated in the Born-Oppenheimer approximation employing a configuration interaction scheme together with multichannel scattering theory to determine for the treatment of continuum states, and the Feshbach partitioning formalism to account for autoionization. We resort to a multipolar expansion of the vector potential in the Coulomb gauge, from which we keep the terms corresponding to DA and retardation effects up to $\mathcal{O}(1/c)$, to account for the interaction with radiation. Finally, we make use of perturbative and non-perturbative propagation schemes to obtain transition amplitudes from which we can extract cross-sections, photoelectron spectra (PES), and molecular frame angular distributions (MFPADs).

In the first part of the results, we demonstrate the coherent control of ionization and dissociation achieved by filtering the higher harmonics in an attosecond pulse train (APT) in an XUV pump-UV probe scheme. By solving the TDSE in DA including electronic and nuclear motion, we are able to extract nuclear and electronic kinetic energy release (KER) spectra to analyze the main ionization pathways as a function of the delay between pump and probe. We then discuss the effect of harmonic filtering in manipulating one-photon against two-photon ionization yields, dissociative ionization channels, and asymmetries in the MFPADs.

In the second part of the results of the thesis, we report the first calculations of Stimulated Raman Scattering (SRS) and Stimulated Compton Scattering (SCS) in H_2 with intense X-ray laser fields. These non-linear phenomena consist in the absorption of a photon and the subsequent stimulated emission of a less energetic one leaving the molecule in an excited state (SRS) or effectively ionizing it (SCS). Theoretically, the inclusion of effects beyond DA becomes mandatory. We begin by investigating the relative role of the dipole ($\boldsymbol{A} \cdot \boldsymbol{P}$) and non-dipole ($\boldsymbol{A}^2$) interaction terms through a perturbative study of the Raman cross-section. The role of the high energy electronic continuum in the partial cancellation of the dipole contribution is also analyzed. We then present results from SRS and SCS calculations using

ultra-short pulses in which we compare the relative contribution of the dipole and non-dipole routes as a function of the photon energy. We assert the validity of perturbation theory by directly comparing SRS calculations with results obtained by solving the TDSE. In SCS, the interference between dipole and non-dipole routes produces asymmetries in the MFPADs, which we analyze. Special attention is given to the effect of molecular orientation.

Finally, we study SCS with two colors, focusing on the effect of the angle between the pulse propagation directions. As seen in atoms, non-dipole effects are enhanced for counter-propagating pulses. We also investigate the effect of color separation in energy.

Keywords: Free-electron lasers, High-order harmonic generation, Hydrogen molecule, Born-Oppenheimer, Attosecond physics, Non-dipole effects, Raman scattering, Compton scattering

UNIVERSIDAD AUTÓNOMA DE MADRID
UNIVERSITÉ DE BORDEAUX

Resumen

Estudio del efecto relativista en la interacción no lineal entre moléculas y pulsos láser cortos de UV y rayos X blandos

por Arturo Sopena Moros

El desarrollo de fuentes de luz de XUV intensas a través de láseres de electrones libres y de la generación de armónicos de alto orden con duraciones de femtosegundos (fs) y sub-fs proporciona una herramienta única para investigar la interacción no lineal entre láseres ultrarrápidos y la materia. En el estudio dinámico del proceso de fotoionización en moléculas a escalas de tiempo ultracortas, la ecuación de Schrödinger dependiente del tiempo ha demostrado ser crucial para la interpretación de observaciones experimentales. En esta tesis presentamos resultados para cálculos *ab initio* de fotoionización en H_2 con pulsos láser ultracortos UV y de rayos X. Nos centramos en el estudio de procesos no lineales que involucran a dos fotones, a su papel en la dinámica nuclear acoplada resultante y a su estudio más allá de la aproximación dipolar.

Nuestro enfoque teórico se basa en un método espectral el cual requiere la determinación de los estados cuánticos de la molécula aislada. Estos estados se calculan en el marco de la aproximación Born-Oppenheimer empleando un esquema de interacción de configuraciones junto con la teoría de *scattering* multicanal para determinar el cálculo de estados del continuo. Para tratar los procesos de autoionización recurrimos al formalismo desarrollado por Feshbach para el cálculo de resonancias en el continuo. Utilizamos una expansión multipolar del vector potencial en el *gauge* de Coulomb, de la cual mantenemos los términos correspondientes a la aproximación dipolar y a los efectos de retardo de orden $\mathcal{O}(1/c)$, para tratar interacción con la radiación. Finalmente, empleamos métodos de propagación perturbativos y no perturbativos para obtener amplitudes de ionización de las que podemos extraer secciones eficaces, espectros de fotoelectrón y distribuciones angulares de fotoelectrón en el marco molecular.

En la primera parte de los resultados demostramos la posibilidad de control coherente en el proceso de ionización y disociación gracias al filtrado de los armónicos superiores en un tren de pulsos de attosegundos en un esquema VUV *pump*-UV *probe*. Al resolver la ecuación de Schrödinger dependiente del tiempo en la aproximación dipolar, incluyendo movimiento electrónico y nuclear, podemos extraer probabilidades de ionización diferenciales en energía cinética nuclear y electrónica para analizar las principales vías de ionización en función del desfase entre *pump* y *probe*. A continuación, discutimos el efecto del filtrado de armónicos en la manipulación de las diferentes rutas de ionización con un fotón o dos fotones, de los canales de ionización disociativos y de las asimetrías en las distribuciones angulares.

En la segunda parte de los resultados de la tesis presentamos los primeros cálculos de dispersión Raman estimulada (DRE) y de dispersión Compton estimulada (DCE) en H_2 con campos láser intensos de rayos X. Estos fenómenos no lineales consisten en la absorción de un fotón y la posterior emisión estimulada de otro fotón menos energético, dejando la molécula en un estado excitado (DRE) o ionizándola

(DES). La descripción teórica de estos fenómenos requiere de un tratamiento más allá de la aproximación dipolar. Comenzamos investigando el papel de los términos de interacción dipolar ($\boldsymbol{A} \cdot \boldsymbol{P}$) y no dipolar ($\boldsymbol{A}^2$) a través de un estudio perturbativo de la sección eficaz Raman. También se analiza el papel de los estados del continuo electrónico a altas energías en la cancelación parcial de la contribución dipolar. A continuación, presentamos los resultados de cálculos de DRE y DES utilizando pulsos ultracortos en los que comparamos la contribución relativa de las rutas dipolar y no dipolar en función de la energía del fotón. Confirmamos la validez de la teoría de perturbaciones comparando directamente cálculos de DRE con resultados obtenidos al resolver la ecuación de Schrödinger dependiente del tiempo. En la DCE, la interferencia entre las rutas dipolar y no dipolar produce asimetrías en los *MFPADs*, las cuales analizamos con especial atención al efecto de la orientación molecular.

Finalmente, estudiamos la DCE con dos colores, centrándonos en el efecto del ángulo entre las direcciones de propagación de los pulsos. Al igual que en átomos, los efectos no dipolares se ven incrementados para pulsos con direcciones de propagación opuestas. También investigamos el efecto de la separación energética entre los pulsos.

Palabras clave: Láseres de electrones libres, Generación de armónicos de alto orden, Molécula de hidrógeno H_2, Born-Oppenheimer, Física de attosegundos, Efectos no dipolares, Efecto Raman, Efecto Compton

UNIVERSIDAD AUTÓNOMA DE MADRID
UNIVERSITÉ DE BORDEAUX

Résumé

Etude des effets relativistes en régime d'interaction non-linéaire entre les molécules et les impulsions laser brèves dans les domaines de fréquences XUV et X mous

par Arturo Sopena Moros

Le développement des sources XUV intenses du type laser à électrons libres (LEL) et génération d'harmoniques d'ordre élevé (GHOE) en régime femtoseconde (fs) et sub-fs permet l'investigation des processus non-linéaires ultra rapides dans l'interaction laser-matière. Dans le contexte de l'étude de la dynamique de la photo-ionisation moléculaire aux temps ultra-brefs, la résolution directe de l'équation de Schrödinger dépendante du temps (ESDT) s'est révélée cruciale pour l'interprétation des observations expérimentales. Dans cette thèse, nous présentons des calculs *ab-initio* pour la photo-ionisation de H_2 en impulsion ultra-brève UV et X. On s'intéressera plus particulièrement aux processus non-linéaires impliquant deux photons, à leur rôle dans le couplage dynamique électron-noyaux ainsi qu'aux effets liés aux corrections à l'approximation dipolaire (AD).

Notre approche théorique est basée sur la méthode spectrale, elle nécessite la détermination des états quantiques de la molécule isolée. Ces états sont calculés dans l'approximation Born-Oppenheimer (BO) dans le contexte de la méthode d'interaction de configuration, en s'appuyant sur la théorie des collisions pour traiter les continua et sur le formalisme de Feshbach pour calculer les états autoionisants. Dans le traitement de l'interaction avec le rayonnement, nous nous basons sur un développement multipolaire du vecteur potentiel du champ en jauge de Coulomb, dont nous conservons les termes correspondant à l'AD et aux effets de retard jusqu'à l'ordre $\mathcal{O}(1/c)$. Finalement, nous utilisons des approches perturbatives et non-perturbatives pour obtenir l'amplitude de transition liée à l'ionisation, à partir de laquelle on calcule les sections efficaces, les spectres de photoélectrons et les distributions angulaire dans le référentiel de la molécule.

En première partie des résultats, nous démontrons comment le contrôle cohérent est réalisé en dynamique moléculaire en filtrant les harmoniques les plus élevées d'un train d'impulsion attoseconde dans un schéma pompe XUV et sonde UV. En résolvant l'ESDT dans l'AD et en prenant en compte les mouvements électroniques et nucléaires on extrait les spectres en énergie correspondants, après l'interaction, afin d'analyser les voies principales d'ionisation en fonction du délai entre les impulsions pompe et sonde. Nous discutons ensuite l'effet du filtrage des harmoniques sur le contrôle des voies d'ionisation à un ou deux photons, des canaux d'ionisation dissociative et des asymétries dans les distributions angulaires.

Dans la seconde partie des résultats de cette thèse, nous présentons les premiers calculs sur les effets Raman et Compton stimulé (ERS et ECS) dans H_2 en champ laser intense dans le domaine X. Ces processus non-linéaires reposent sur l'absorption d'un photon et l'émission stimulée d'un autre photon de moindre énergie laissant la molécule dans un état excité (ERS) ou ionisé (ECS). L'inclusion des effets non-dipolaires est requise dans la théorie. Nous débutons par l'analyse du rôle relatif

des couplages dipolaire ($\boldsymbol{A} \cdot \boldsymbol{P}$) et non-dipolaire ($\boldsymbol{A}^2$) via l'étude de la section efficace Raman en régime perturbatif. Le rôle des états du continu de haute énergie dans l'annulation partielle des contributions dipolaires est aussi analysé. Nous présentons des calculs des processus Raman et Compton stimulés en impulsion ultra brève et les contributions des couplages dipolaire et non-dipolaire sont comparées en fonction de l'énergie du photon. La validité de la théorie des perturbations est vérifiée en comparant les résultats avec les calculs ESDT pour l'ERS. Concernant l'ECS, les interférences entre les amplitudes associées aux couplages dipolaire et non-dipolaire produisent des asymétries dans les distributions angulaires des électrons émis, elles sont analysées en fonction de l'orientation de la molécule.

Finalement, l'étude de l'ECS «deux couleurs» est présentée, avec en particulier l'effet lié à la direction de propagation relative des deux impulsions.

Mot clés : Lasers à électrons libres, Génération d'harmoniques d'ordre élevé, Molécule d'hydrogène, Born-Oppenheimer, Physique attoseconde, Effets non dipolaires, Effet Raman, Effet Compton

UNIVERSIDAD AUTÓNOMA DE MADRID
UNIVERSITÉ DE BORDEAUX

Résumé long

Etude des effets relativistes en régime d'interaction non-linéaire entre les molécules et les impulsions laser brèves dans les domaines de fréquences XUV et X mous

par Arturo Sopena Moros

Le développement de sources XUV intenses du type laser à électrons libres (LEL) et génération d'harmoniques d'ordre élevé (GHOE) en régime femtoseconde (fs) et sub-fs permet l'investigation des processus non-linéaires ultra rapides dans l'interaction laser-matière. Certains processus fondamentaux, comme la photoionisation des atomes et des molécules, sont actuellement réexaminés afin de mieux comprendre leur dynamique à l'échelles des temps ultra-brefs. En plus de la durée de l'impulsion, l'augmentation de l'intensité des sources GHOE et LEL offre désormais la possibilité d'observer les effets non-linéaires (c'est à dire, l'émission/absorption cohérente de plusieurs photons) dans les domaines XUV et X. Le développement des sources GHOE et LEL alimente une intense activité en physique atomique et moléculaire tant sur le plan expérimental que théorique. Dans ce contexte, la théorie joue un rôle crucial dans l'interprétation des résultats des expériences et aussi pour la suggestion de nouvelles voies de recherche. La résolution directe de l'équation de Schrödinger dépendant du temps (ESDT) s'est avérée être une technique très puissante dans ce contexte. Mais résoudre l'ESDT en trois dimensions pour tous les degrés de liberté électroniques dans le cas atomique multi-électronique (auxquels il faut ajouter la dimension vibrationnelle pour les molécules) est encore un défi ouvert, même si des progrès ont été réalisés. Dans cette thèse, nous présentons les résultats de calculs *ab initio* de photoionisation de H_2 en impulsions laser ultra-brèves UV et X. On s'intéressera plus particulièrement aux processus non-linéaires impliquant deux photons, à leur rôle dans le couplage dynamique électron-noyaux ainsi qu'aux effets liés aux corrections à l'approximation dipolaire (effets de retard liés à la vitesse finie de la lumière).

Ce manuscrit est structuré en trois parties. Dans la Partie I, nous décrivons l'ensemble des outils théoriques utilisés pour étudier la photoionisation de H_2 avec des impulsions ultra-brèves. Notre approche est basée sur la méthode spectrale, elle nécessite la détermination des états quantiques de la molécule isolée, ici dans une représentation non-relativiste. Nous commençons dans le Chapitre 1 par une explication des méthodes appliquées pour calculer les fonctions d'onde des électrons et des noyaux de la molécule isolée dans l'approximation Born-Oppenheimer (BO). Tout d'abord, nous décrivons comment construire les niveaux d'énergie monoélectroniques de l'ion moléculaire H_2^+ grâce à une expansion de la partie radiale sur des fonctions B-splines et sur des harmoniques sphériques pour la partie angulaire. Pour obtenir les états électroniques H_2 liés, nous diagonalisons l'Hamiltonien total à deux électrons en développant la fonction d'onde sur la base des états mono-électroniques H_2^+, dans le contexte de la méthode d'interaction configuration. Cependant, la diagonalisation directe de l'Hamiltonien sans champ ne donne pas une description correcte du continuum électronique et des états autoionisants, qui jouent un rôle crucial

dans la photoionisation. De plus, étant donné que les durées de vie d'autoionisation sont de l'ordre du temps caractéristique du mouvement nucléaire, un traitement au-delà de BO devient obligatoire. Pour éviter ces problèmes, nous nous appuyons sur le formalisme de Feshbach qui permet le calcul des états doublement excités et du continuum électronique. Pour ces derniers, nous imposons des conditions limites asymptotiques correctes grâce à l'utilisation de la théorie de la diffusion en présence de plusieurs canaux d'ionisation (théorie « multicanaux »). A la fin de ce chapitre, nous détaillons les étapes nécessaires pour calculer les fonctions d'onde vibrationnelles utilisées pour construire les états propres vibroniques dans l'approximation BO.

Dans le Chapitre 2, nous décrivons l'approche semi-classique de la photoionisation dans laquelle le champ électromagnétique est traité classiquement et la molécule de façon quantique. Nous recourons à la construction d'un Hamiltonien de couplage minimal où le vecteur potentiel est exprimé dans la jauge de Coulomb. La dépendance simultanée des coordonnées spatiales et temporelles du vecteur potentiel conduit généralement à un problème insoluble. Pour cette raison, il est habituel de recourir à un développement de Taylor du vecteur potentiel dans lequel on ne retient que le premier ordre, obtenant ainsi l'approximation dipolaire bien connue. Nous discutons les limites d'applicabilité de l'approximation dipolaire en fonction de l'intensité et de la fréquence du champ, en les reliant à l'apparition d'effets relativistes. Nous terminons avec la dérivation de l'Hamiltonien complet représentant l'interaction entre la molécule H_2 et le rayonnement, y compris les effets de retard jusqu'à l'ordre $\mathcal{O}(1/c)$ correspondant au deuxième ordre de du développement de Taylor.

Dans le Chapitre 3, nous commençons par introduire les bases de notre traitement de l'interaction laser-molécule, nous discutons ensuite les différents schémas de propagation dans les approches perturbatives et non perturbatives employées dans le manuscrit. L'approche non perturbative est basée sur la résolution de l'ESDT avec une méthode spectrale, comme mentionné précédemment. Pour le traitement perturbatif, nous introduisons les éléments de matrice de transition du premier et du second ordre. Nous discutons également la méthodologie employée pour extraire différentes quantités mesurables telles que les sections efficaces d'ionisation, les spectres de photoélectrons (PES en anglais pour « PhotoElectron Spectrum ») et les distributions angulaires des photoélectrons dans le référentiel moléculaire (MF-PAD en anglais pour « Molecular Frame Photoelectron Angular Distribution ») à partir des calculs perturbatifs et non perturbatifs.

Après avoir posé les bases de notre méthode, nous présentons la première partie des résultats de la thèse dans laquelle nous démontrons le contrôle cohérent obtenu en filtrant les harmoniques supérieures dans un train d'impulsions attoseconde (TIA), dans un schéma pompe-sonde. De cette façon, nous illustrons une application de notre méthode dans la région XUV où l'approximation dipolaire reste valide. Nous présentons des résultats pour des simulations en configuration expérimentalement réalisable dans laquelle un TIA XUV d'une durée de 6 fs déclenche la dynamique électron-nucléaire de la molécule. Cette dynamique est ensuite sondée au moyen d'une impulsion UV intense de même durée que la pompe. Pour étudier les effets du filtrage harmonique, nous analysons deux cas correspondant à deux trains d'impulsion différents. Le premier train inclut jusqu'à la 17ème harmonique d'un champ infrarouge (IR) de 800 nm, la 9ème harmonique étant la fréquence centrale du train. L'impulsion sonde utilisée correspond à la 3ème harmonique du même champ IR. Nous explorons ensuite le résultat de l'excitation et de la photoionisation en filtrant les harmoniques les plus élevées et en contrôlant le délai entre la pompe

et la sonde. En résolvant le TDSE dans l'approximation dipolaire et en prenant en compte les mouvement électroniques et nucléaires, nous sommes en mesure d'extraire les spectres en énergie électronique et nucléaire et d'analyser sur cette base les principales voies d'ionisation. Nous discutons ensuite de l'effet du filtrage des harmoniques sur le contrôle des voies d'ionisation à un ou deux photons, des canaux d'ionisation dissociatifs et de l'apparition des asymétries dans les distributions angulaires.

Nos calculs montrent que, pour les énergies et les intensités laser considérées dans l'étude, l'ionisation non dissociative est le processus d'ionisation dominant pour les cas filtrés et non filtrés. Pour ce processus, le filtrage harmonique réduit considérablement le rendement d'ionisation et, en supprimant la voie d'ionisation à un photon, nous pouvons contrôler l'ionisation en accordant le délai entre la pompe et la sonde.

Grâce à l'analyse des spectres en énergie cinétique nucléaire et électronique, nous avons mis en évidence les principales voies quantiques de l'ionisation non dissociative et dissociative. Pour le cas non filtré, l'ionisation dissociative se produit principalement par simple photo-absorption des harmoniques supérieures du train et par absorption à deux photons via "l'ionisation au-dessus du seuil" (ATI en anglais pour « Above Threshold Ionization »). Nous avons montré la possibilité de contrôler les canaux dissociatifs pour le cas non filtré en fonction du délai et avons observé que l'ATI joue un rôle clé. Pour le cas filtré, la seule contribution à l'ionisation dissociative provient de l'absorption à deux photons à travers les états excités de la molécule. Cette dernière contribution est également présente pour le cas non filtré, mais elle est obscurcie par la prédominance de l'absorption à un photon et de l'ATI. Nous avons observé que le filtrage harmonique ne modifiait pas l'évolution temporelle de la molécule excitée, donc cette technique peut être utilisée pour caractériser la dynamique sous-jacente des états excités de H_2.

Pour l'ionisation non dissociative, nous avons démontré qu'en filtrant les harmoniques supérieures de la pompe, nous pouvons contrôler l'ionisation par interférence entre les paquets d'ondes vibroniques formés dans les états excités $B^1\Sigma_u^+$ et $B'^1\Sigma_u^+$ de H_2.

Enfin, nous montrons que des asymétries dans les MFPAD sont produites dans le cas non filtré, du fait de la présence d'états de symétrie différente par rapport au centre d'inversion de la molécule. Nous avons également montré que le contrôle de la direction d'éjection de l'électron avec le délai est possible. En éliminant la voie d'ionisation à un photon, l'interférence entre des états de parité différente n'est plus possible, nous avons donc observé que le filtrage harmonique permet d'extraire les MFPAD symétriques.

Nous consacrons Part III à l'étude des effets non dipolaires dans la diffusion inélastique des photons X par la molécule H_2. Nous nous concentrons sur l'étude de l'effet Raman stimulé (ERS) et de l'effet Compton stimulé (ECS) dans H_2 (dans l'approximation non relativiste pour la représentation du Hamiltonien de la molécule isolée mais en incluant les effets de retard en $1/c$ dans l'interaction avec le champ). Ces phénomènes consistent en l'absorption d'un photon de haute énergie et l'émission stimulée simultanée d'un photon de moindre énergie laissant la molécule dans un état excité (ERS) ou ionisé (ECS). L'observation de ces phénomènes nécessite des longueurs d'onde dans la gamme XUV ou X, des intensités élevées telle que celles générées dans les sources LEL sont nécessaires pour obtenir une magnitude importante pour ces processus (les probabilités liées à l'ERS et l'ECS étant proportionnelles au carré de l'intensité en régime perturbatif). Dans ce régime de fréquence, l'inclusion d'effets au-delà de l'approximation dipolaire devient obligatoire

dans la théorie. En raison de la haute énergie obtenue par l'électron et donc du grand nombre d'états électroniques à inclure dans les calculs, et afin de maintenir ces calculs réalisables d'un point de vue computationnel, la molécule H_2 a été traitée dans l'approximation des noyaux fixes à la distance d'équilibre. Cette approximation se justifie aussi physiquement compte tenu de la durée ultra-brève de l'impulsion laser. Le Chapitre 5 se concentre sur l'étude de l'ERS, plus précisément sur le rôle relatif du terme dipolaire ($\boldsymbol{A} \cdot \boldsymbol{P}$) et du terme non-dipolaire ($\boldsymbol{A}^2$) dans l'interaction laser-molécule. Ces contributions sont analysées dans le contexte de la théorie des perturbations dépendante du temps (TPDT) en calculant la section efficace Raman, avec une attention particulière sur l'annulation partielle de la contribution dipolaire. Pour calculer cette section efficace, nous présentons une dérivation des éléments de matrice de Kramers-Heisenberg-Waller caractérisant les effets Raman et Compton. En raison de la sensibilité numérique de l'annulation partielle évoquée plus haut et en tenant compte des grandes énergies des photons impliqués, une description précise des états du continuum d'énergie élevée est nécessaire. Nous réalisons d'abord une étude de convergence du calcul des états du continuum à hautes énergies sur la base de l'évaluation de la section efficace de photo-ionisation à un photon. Cela nous permet de présenter une paramétrisation du continuum électronique jusqu'à 2000 eV d'énergie électronique. Notre analyse de la section efficace Raman montre que l'annulation partielle de la contribution dipolaire est produite par l'interférence destructive des amplitudes de transition du second ordre associées aux chemins d'excitation d'ordre direct et inverse.

Dans la dernière partie du Chapitre 5, nous avons développé plusieurs méthodes perturbatives pour étudier l'ERS avec des impulsions ultra-courtes dans le contexte de l'approche TPDT, les résultats sont comparés aux valeurs obtenues en résolvant l'ESDT. Nous présentons les résultats de calculs ERS dans le cadre de l'TPDT en utilisant une impulsion de forme gaussienne avec une largeur à mi-hauteur (FWHM en anglais pour « Full Witdth at Half Maximum ») de 68 as, une intensité de 10^{18} W/cm^2, une direction de propagation de la lumière selon x, une direction de polarisation selon z et des fréquences allant de 5 a.u. à 60 a.u. Nous analysons les problèmes numériques associés aux états résonants du continuum intermédiaire dans le cadre de divers schémas perturbatifs. Pour le calcul non-perturbatif, nous avons étendu avec succès la méthode détaillée dans le Chapitre 3 pour étudier les effets de retard et nous avons présenté les résultats des calculs pour l'ERS. L'accord entre les résultats obtenus en résolvant l'ESDT et notre schéma basé sur l'approche TPDT valide l'utilisation de la théorie des perturbations comme un outil approprié pour étudier les effets de retard dans l'ERS. Nous avons observé deux mécanismes d'excitation différents, l'un à faibles énergies photoniques dominé par la contribution dipolaire et l'autre à hautes énergies dominé par des effets non dipolaires. En raison de la présence de deux mécanismes d'excitation différents, des états liés de symétries différentes sont peuplés. On démontre que les probabilités d'excitation résultantes varient comme $(1/\omega)^N$ selon deux lois de puissance en N différentes, la contribution dipolaire décroissant beaucoup plus rapidement que la contribution non-dipolaire.

Dans le Chapitre 6, nous présentons la première étude non perturbative de l'ECS dans H_2 au-delà de l'approximation dipolaire en utilisant des impulsions ultra-courtes. Notre analyse est basée sur l'examen des spectres photoélectroniques et des MF-PADs. Dans ce type de calcul, les couplages continuum-continuum jouent un rôle clé et leur description appropriée au contexte de la théorie « multicanaux » entraîne un paramétrage numérique supplémentaire. Poursuivant l'étude de convergence du chapitre précédent, nous présentons une analyse du rôle des seuils d'ionisation plus élevés dans la description « multicanaux » des états impliqués dans l'ECS. Pour

cette analyse, nous avons effectué des calculs en utilisant une impulsion de forme gaussienne avec les mêmes paramètres que dans le chapitre précédent avec une fréquence de 20 a.u., correspondant à la région de basse énergie des rayons X mous. Une attention particulière est portée à la région d'énergie électronique E_e allant de 0 à 2,5 a.u., associée à l'effet Compton. Nous montrons que la contribution non dipolaire domine le PES sur toute la plage du pic ECS pour la configuration de propagation et de polarisation considérée plut haut. En raison de l'interférence cohérente entre les voies d'ionisation dipolaires et non-dipolaires, nous avons observé des asymétries dans les MFPADs intégrés en énergie. Nous montrons que l'inclusion seule du premier seuil d'ionisation dans les calculs suffit pour le calcul des PESs et des MFPADs, les autres seuils d'ionisation conduisant à des corrections faibles. Cela n'est pas surprenant si l'on prend en compte la différence entre les sections efficaces associées aux premier et second seuils d'ionisation présentée au Chapitre 5.

Enfin, nous présentons une analyse des effets d'orientation moléculaire dans l'étude de l'ECS. Nous avons effectué des calculs avec trois configurations d'impulsions différentes associées à des orientations de la molécule le long des trois axes cartésiens pour une configuration d'impulsion fixe. Pour chaque configuration d'impulsion étudiée, nous avons utilisé la même impulsion de forme gaussienne que précédemment et nous présentons des résultats pour trois énergies de photons différentes ; $\omega = 20$, 40 et 60 a.u. En étudiant les PESs, nous montrons que la contribution non-dipolaire domine la contribution dipolaire lorsque l'énergie du photon augmente, pour toutes les orientations moléculaires étudiées. Ceci est associé à l'annulation partielle de la contribution dipolaire, évoquée dans le cas de l'ERS. Pour les cas de la polarisation perpendiculaire, nous avons constaté que les transitions dipolaires peuplent préférentiellement ${}^1\Sigma_g^+$ et que la contribution de ${}^1\Delta_g$ peut être négligée. On observe des différences dans l'évolution de la contribution relative non-dipolaire en fonction des énergies photoniques dans les PESs pour les différentes orientations moléculaires étudiées. Une explication de cette tendance en termes de poids plus important des composantes perpendiculaires a été donnée. Nous présentons les MFPADs totaux, intégrés dans la région énergétique associée à l'ECS, et les contributions dipolaires et non-dipolaires pour les trois orientations différentes étudiées. Nous observons que les effets non-dipolaires se manifestent dans les MFPADs de manière plus accentuée comparé aux PESs, produisant ainsi des asymétries alignées avec la direction de propagation pour toutes les orientations étudiées, même pour les contributions relatives faibles des transitions dipolaires. Nous avons remarqué une diminution de l'asymétrie avec l'énergie des photons, elle est due à l'augmentation du poids relatif des effets non-dipolaires par rapport aux effets dipolaires. Une asymétrie directe (émission des électrons dans la direction de propagation du champ) est produite quand le plan formé par les vecteurs de propagation et de polarisation du champ contient l'axe internucléaire. En revanche, lorsque ce plan est perpendiculaire à l'axe internucléaire, une asymétrie vers l'arrière de l'émission électronique se produit. Ceci est associé à la phase relative des contributions dipolaires et non-dipolaires dans le calcul des MFPADs. Lors de l'analyse des MFPADs pour des énergies données E_e de l'électron émis, nous avons remarqué une diminution de la magnitude avec E_e et ω en accord avec les PESs. Pour le cas de la propagation de l'impulsion parallèle à l'axe internucléaire avec une polarisation perpendiculaire à celui-ci, nous montrons une forte dépendance de l'asymétrie des MFPADs avec l'énergie des photoélectrons, pour toutes les énergies des photons. On observe dans ce cas l'apparition d'ondes partielles plus élevées pour les contributions dipolaires et non-dipolaires. Après avoir analysé les MFPADs correspondant au cas où la polarisation et la propagation sont perpendiculaires à l'axe internucléaire, nous concluons

que, lorsque les contributions dipolaires et non-dipolaires sont en concurrence, des asymétries plus fortes sont produites si la contribution dominante provient d'effets non-dipolaires.

Unité de Recherche

Centre Lasers Intenses et Applications (CELIA), UMR 5107
Université de Bordeaux, CNRS, CEA
43 rue Pierre Noailles, 33400, Talence, France

Departamento de Química
Facultad de Ciencias, Universidad Autónoma de Madrid
Calle Francisco Tomás y Valiente 7, 28049, Madrid, Spain

Acknowledgements

I would like to thank all the people that have helped me during these last years and without whom this thesis would have not been possible.

To my supervisors Fernando Martín and Henri Bachau, for trusting me to do this job, for teaching me so many things, and for making it so easy for me to go back home to see my friends and family.

To Alicia Palacios, my co-supervisor, for spending so much time on teaching me, even when she had none.

To Fabrice Catoire, my other co-supervisor, for the corrections on the manuscript and for being always available next door.

To all my good friends from UB, for all the visits, laughs, and support. Especially to Guillem and Sergi, my brothers in arms.

To Rafa and Lucas, for so many years of friendship.

To Anna, the person with the biggest heart I know.

To Jan, Sara, Marta, and Mariona, for making it so easy to be part of their life.

To Marc and Aleix, who adopted me in the middle of the pandemic, for all the good times we spent during lockdown.

To my office mates at UAM, Nestor and Manuel, for their help at the beginning of my thesis.

To my fellow master, PhD students, and postdocs at UAM, especially to Fernando, Pablo, Paula, Eva, Guille, Ransel, Marcos, Vani, Jorge, Enrique, Octavio, and Dario, for so many laughs and stories.

To all the people at CELIA, especially to Luke, Sandra, and Pedro, for the good times at the office and outside of it.

To my roommates, Luis and Marcos, two dear friends who helped me so much adapting to my new life in Madrid and Bordeaux, I will always remember those world-changing conversations.

To the Casanovas-Bayo-Manso family, especially to Isabel, Victor, Maria, and Borja, for taking me into the family.

To my family, especially to my father, mother, brother, and sister, for all the love and support over the years and for making me the person I am today.

To my late grandfathers, Ramon and Eduardo, for inculcating in me the value of studying and learning, and to my grandmothers, Esther and Amparín, for taking care of me both as a child and as an adult.

And to Berta, my partner, because no other person has endured more the distance, the constant traveling, and the self-doubt and the stress that this thesis has caused me. Thank you for being always by my side supporting me.

Contents

List of Figures

List of Abbreviations

APT	**A**ttosecond **P**ulse **T**rain
ATI	**A**bove-**T**hreshold **I**onization
BO	**B**orn-**O**ppenheimer
CI	**C**onfiguration **I**nteraction
COLTRIMS	**Co**ld **T**arget **R**ecoil-**I**on **M**omentum **S**pectroscopy
DA	**D**ipole **A**pproximation
EKE	**E**lectron **K**inetic **E**energy
FEL	**F**ree **E**lectron **L**aser
FNA	**F**ixed **N**uclei **A**pproximation
FWHM	**F**ull-**W**idth **H**alf **M**aximum
HHG	**H**igh-order **H**armonic **G**eneration
KHW	**K**ramers-**H**eisenberg-**W**aller
KER	**K**inetic **E**nergy **R**elease
MFPAD	**M**olecular-**F**rame **P**hotoelectron **A**ngular **D**istribution
NKE	**N**uclear **K**inetic **E**nergy
PES	**P**hoto**E**lectron **S**pectrum
PT	**P**erturbation **T**heory
SAP	**S**ingle **A**ttosecond **P**ulse
SCS	**S**timulated **C**ompton **S**cattering
SRS	**S**timulated **R**aman **S**cattering
STO	**S**later-**T**ype **O**rbital
TDFCC	**T**ime-**D**ependent **F**eshbach **C**lose-**C**oupling
TDPT	**T**ime-**D**ependent **P**erturbation **T**heory
TDSE	**T**ime-**D**ependent **S**chrödinger **E**quation
UCS	**U**ncoupled **C**ontinuum **S**tates
VC	**V**elocity **C**orrelation
VMI	**V**elocity **M**ap **I**maging
XFEL	**X**-ray **F**ree **E**lectron **L**aser

Introduction

The ability to observe the inner motion of atoms and molecules at their natural timescales is essential for a deep understanding of various important phenomena with applications in physics, chemistry, biology, or material sciences. Resolving the short timescales associated with these motions is one of the main reasons that motivated the development of new radiation sources capable of producing ultrashort laser pulses. With each new reduction of the pulse duration, new degrees of freedom became accessible. From picoseconds (1 ps = 10^{-12} s), related to rotations, and femtoseconds (1 fs = 10^{-15} s), related to vibrations and dissociation, to the attosecond (1 as = 10^{-18} s) time scale, related to electronic motion, each new breakthrough has made it possible to gain a deeper understanding of various essential processes in atoms and molecules. The attosecond regime, in particular, has seen significant developments in the past two decades, from the first demonstration of a measurement with attosecond resolution [1], to the generation of the first first train of attosecond pulses [2] and the first isolated attosecond pulse [3], down to the shortest pulse ever generated, with a duration of 47 attoseconds [4]. The advent of new technological capabilities in laser sources has also been accompanied by the development of novel detection techniques such as velocity map imaging (VMI) and cold target recoil ion momentum spectroscopy (COLTRIMS) [5,6].

Electronic motion is at the core of the description of the interaction between matter and visible, ultraviolet, and X-ray light. Thanks to the unprecedented time resolution offered by attosecond pulses, some fundamental processes, like the photoionization of atoms and molecules, are now being reinvestigated in order to get a better comprehension of their dynamics at ultrashort timescales. An example of this is the measurement of photoemission time delays between different atomic orbitals [7], a process assumed to occur instantly. Another example is the time-resolved measurement of Auger relaxation in krypton atoms using a sub-femtosecond soft X-ray pulse [8], performed shortly after the first measurement with attosecond resolution. Given the fundamental role that electron correlation plays in these processes, the study of electronic processes in the attosecond scale can help gain new insights into this matter. Of particular interest is the observation of ultrafast dynamics in molecular targets for its potential applications in chemistry, biology, and material sciences. The ability to image and control with attosecond pulses the motion of electrons in chemical bonds opens the way for performing chemistry in the attosecond domain [9]. This has been studied using a train of attosecond XUV pulses in combination with a femtosecond IR pulse to control dissociative ionization in O_2 [10]. For more complex systems, experiments with X-ray radiation have analyzed the ultrafast breakage of biomolecules [11], which is vital to understand X-ray radiation damage in living tissues.

In the interaction between attosecond pulses and large molecules, due to the broad spectral bandwidth of these pulses, a large number of states are populated, thus triggering a variety of processes in molecules. The complexity of the resulting dynamics requires theoretical modeling to support experiments. However, the role of theory does not merely limit to assisting with the interpretation of experimental

observations, as it has the potential to be a precursor of experiments. Theoretical works on multielectron wave packet propagation [12] preceded the detection of ultrafast charge migration in polyatomic molecules [13] by almost ten years. Something similar occurred for the first attempted XUV-pump/XUV-probe experiment to explore the coupled electron and nuclear dynamics in the hydrogen molecule [14], which followed a scheme previously proposed in a theoretical work [15]. From both the experimental and theoretical point of view, the H_2 molecule has been the working horse to study ultrafast phenomena in molecules. This system has the advantage of being computationally manageable with few approximations, which has allowed the study of the coupled electron-electron and electron-nuclear dynamics induced by ultrashort laser pulses [16–18].

Regarding the generation of ultrashort pulses to study electron dynamics, the two main sources are HHG [19] and FELs [20]. The production of ultrashort pulses through HHG results from the interaction of an atom or molecule with an intense IR field ($I = 10^{13} - 10^{16}$ W/cm^2). The high intensity of the IR field allows for tunnel ionization to occur, the free electron is then accelerated by the driving electric field, which then returns it to the parent ion position where it recombines. As a result of excess kinetic energy gained by the electron due to the interaction with the laser, an attosecond XUV pulse is emitted upon recombination every half a period of the IR field. This semi-classical explanation of HHG constitutes the well-known three-step model and is based on the strong-field approximation. However, when it comes to X-rays ultrashort pulses, the low conversion efficiency of HHG in the X-ray regime makes FELs the only viable source of high-intensity pulses. To produce these pulses, a beam of electrons is accelerated to relativistic speeds. The electron beam then passes through an array of magnets with alternating polarization called ondulator, which produces a coherent ultrashort laser pulse through the process of self-amplified spontaneous emission (SASE). These facilities provide ultrashort pulses with unprecedented intensities of the order of 10^{20} W/cm^2, over a large range of photon energies going from VUV to the hard X-ray domain. As seen in figure I.1, X-ray FELs (XFELs) are still not able to produce sub-femtosecond pulses routinely, although important progress is being made to achieve this goal [21]. Extending X-ray in the attosecond domain is of crucial interest. For example, it allows resolving in time the dynamics of electronic rearrangement in atoms after core excitation or ionization, which is of the order of a few hundreds of attoseconds. The high intensity of XFELs also opens the way to the exploration of nonlinear processes in the X-ray regime, like direct two-photon ionization of Ne^{8+} [22] or nonlinear Compton scattering [23]. Although the typical intensities of the pulses generated by XFELs can be very large, their short wavelengths ensure a ratio between the ponderomotive energy (the quiver energy of the electron in the electromagnetic field, $U_p = I/4\omega^2$) and the photon energy is much less than 1, which ensures a negligible distortion of the molecular potentials. At the same time, the value of the Keldysh parameter, given by $\sqrt{I_p/U_p}$ where I_p is the ionization potential, is much greater than 1, making tunnel ionization unfavorable and allowing for a perturbative treatment of photoionization.

At the short wavelengths associated with X-rays, the upper limit of the dipole approximation is reached, and the spatial dependence of the electromagnetic field cannot be neglected anymore. Theoretical studies and experiments in atoms and molecules using XFEL radiation have shown that the inclusion of effects beyond the dipole approximation becomes mandatory [25, 26]. Although the study of non-dipole effects has been studied in the lower limit for long wavelengths in the framework of strong-field approximation [27], studies with molecules in the short wave limit are scarce. This case is of particular interest since the breakdown of the dipole

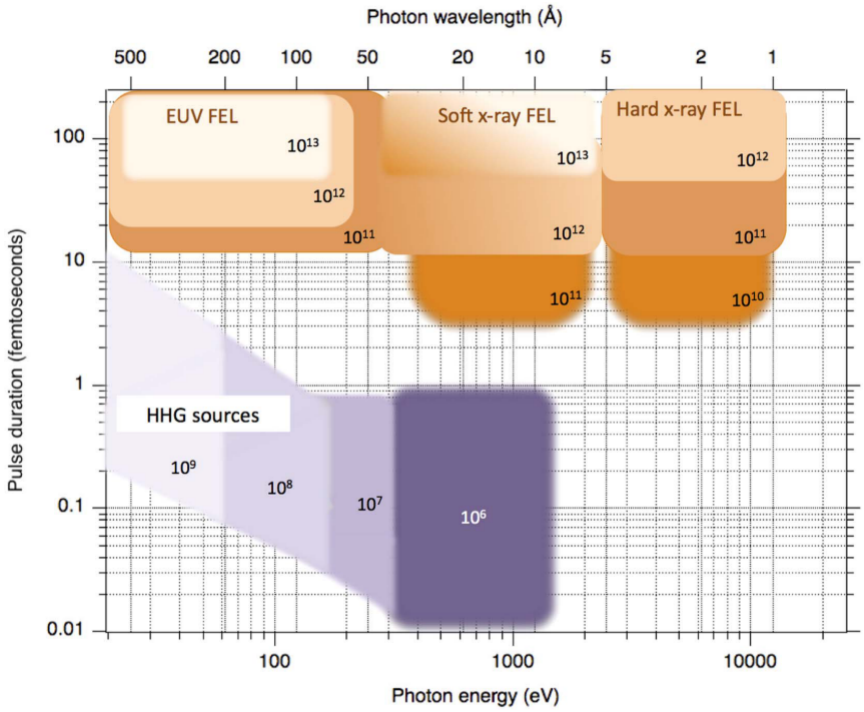

FIGURE I.1 – Figure from Ref. [24] showing the phase space covered by the XFEL and HHG sources discussed in the reference. For XFELs, the pulse duration represents that of a single pulse, whereas, for HHG, the range spans both single pulses and pulse trains spaced by the period of the driver laser. The numbers in each island indicate the number of photons/pulse/1% bandwidth.

approximation is associated with a forward/backward asymmetry in the PAD [28]. In the case of molecules, this introduces interesting perspectives due to the additional degrees of freedom with respect to atoms.

The goal of this thesis is to extend a theoretical approach extensively and successfully used in treating the interaction between XUV and IR pulses and the H_2 molecule [15, 29–32] to the soft X-ray domain and later to X-ray. This theoretical approach is based on the resolution of the TDSE with a spectral method where the total wave function is built as a linear combination of the field-free states of the molecule. To build these states, we make use of an expansion on a basis of B-splines radial functions and spherical harmonics. This type of basis has been extensively used in atomic and molecular physics with excellent results [33]. Even in a small system like H_2, the complexity of the photoionization process at ultrafast time scales is daunting. If one wishes to correctly describe dissociative ionization or autoionization, nuclear motion and electron correlation must be taken into account. We do so by calculating the field-free states through a CI expansion in the framework of the BO approximation. Since autoionization competes in time with nuclear motion, we need to resort to the $\mathcal{P}$ and $\mathcal{Q}$ orthogonal projectors of the Feshbach partitioning formalism to go beyond the BO approximation. One of the main advantages of our method is that thanks to the use of multichannel scattering theory, the coefficients of the expansion of our total wave function represent physical ionization amplitudes in the asymptotic limit. This makes the calculation of PES and MFPADs straightforward. We begin by studying the effects of harmonic filtering in a pump-probe scheme using an

APT to illustrate the application of our method in the XUV regime. To extend the applicability of our theoretical toolbox to higher photon energies, we study Compton and Raman scattering, two emblematic processes in the X-ray domain. These processes require to tackle the challenging task of describing the high energy continuum electronic states and the new ionization routes appearing due to the breakdown of the dipole approximation in the X-ray domain. Our theoretical approach probes to be successful in the description of these process in the fixed nuclei approximation (FNA) including retardation effects up to $\mathcal{O}(1/c)$ with the perspective in the future to include nuclear motion and include higher-order retardation effects.

This manuscript is structured in three main parts. In Part I, we describe the set of theoretical tools used to study photoionization of H_2 with ultrashort pulses. We begin in Chapter 1 with an exposition on the methods used to calculate the electron and nuclear wave functions in the BO framework of the different molecular field-free states. First, we describe how to build the one-electron H_2^+ orbitals needed in the CI expansion of the two-electron wave function. We introduce the Feshbach formalism that allows for the calculation of the doubly excited states and the electronic continuum. For these last, we impose the correct asymptotic boundary through the use of multichannel scattering theory. In Chapter 2, we describe our semi-classical approach to photoionization in which the electromagnetic field is treated classically. In the description of the electromagnetic field, we focus on the spatial dependence of the vector potential and discuss the limits of applicability of the dipole approximation as a function of the field intensity and frequency. We finish with the derivation of the full Hamiltonian representing the interaction between the H_2 molecule and radiation including retardation effects up to $\mathcal{O}(1/c)$ in a non-relativistic regime. In Chapter 3, we begin with the introduction of the interaction picture and then discuss the different perturbative and non-perturbative propagation schemes. Our non-perturbative approach is based on the resolution of the TDSE with a spectral method. We also discuss how to extract the different physical observables from both perturbative and non-perturbative calculations

Once we have laid the foundation of our method, we present the first results of this thesis in Part II. In Chapter 4, we demonstrate the coherent control achieved by filtering the higher harmonics in an XUV APT in a pump-probe scheme. The analysis of the effects of the time delay between pump and probe also shows that manipulation of dissociative ionization channels is possible and the effects of harmonic filtering are discussed. At the end of the chapter we present conclusions to this part.

We devote Part III to the study of non-dipole effects in the inelastic scattering of X-ray photons by the H_2 molecule. Chapter 5 focuses on the study of SRS, specifically on the relative role of the dipole and non-dipole contributions. These contributions are analyzed in the context of time-dependent perturbation theory (TDPT) through the calculation of the Raman cross-section, focusing on the partial cancellation of the dipole contribution. We present a convergence study in the calculation of continuum states at high energies based on the calculation of the one-photon cross-section. For the last part of this chapter, we developed several perturbative schemes to study SRS with ultrashort pulses in the context of TDPT, which we compare to results obtained by solving the TDSE. In Chapter 6 we present a study in SCS with ultrashort pulses. Continuing the convergence study of the previous chapter, we present an analysis of the role of higher ionization thresholds in the multichannel description of the states involved in SCS. By solving the TDSE, we are able to extract PESs, integrated MFPADs, and differential in photoelectron energy MFPADs. As a result of the inclusion of non-dipole effects, asymmetries appear in the MFPADs,

which we analyze as a function of the photon energy, the molecular orientation, and the photoelectron energy. At the end of this chapter we present conclusions to this part of the results. We finish with some general conclusions of the thesis as a whole, future perspectives and an Appendix A detailing some aspects of the modeling of the pulses used throughout the thesis. Atomic units ($m_e = \hbar = e = 1$) are used across this thesis unless stated otherwise.

Part I

Theoretical Methods

Chapter 1

Electronic and nuclear structure of H_2

For the theoretical study of photoionization in molecules we make use of a spectral method to solve the TDSE. The first step is then to find stationary solutions for the field-free evolution of the molecule, which implies solving the eigenvalue equation that is the time-independent Schrödinger equation:

$$\mathcal{H}_0(\boldsymbol{r},\boldsymbol{R})\Psi(\boldsymbol{r},\boldsymbol{R}) = E\,\Psi(\boldsymbol{r},\boldsymbol{R}). \tag{1.1}$$

Since we are interested in the electronic and vibrational motion induced by a photoionization event we have to take into account both electronic and nuclear degrees of freedom, $\boldsymbol{r}$ and $\boldsymbol{R}$ respectively. In the previous equation, $\mathcal{H}_0(\boldsymbol{r},\boldsymbol{R})$ represents the total non-relativistic Hamiltonian for the internal motion of a diatomic molecule. This Hamiltonian takes the following form when taking the coordinate origin to be the geometrical center of the nuclei:

$$\begin{aligned}\mathcal{H}_0 = \sum_{i=1}^{n}\left[-\frac{1}{2}\nabla^2_{\boldsymbol{r}_i} - \frac{Z_A}{|\boldsymbol{r}_i-\boldsymbol{R}_A|} - \frac{Z_B}{|\boldsymbol{r}_i-\boldsymbol{R}_B|}\right] + \sum_{i>j}\frac{1}{|\boldsymbol{r}_j-\boldsymbol{r}_i|} + \frac{Z_A Z_B}{R} \\ - \frac{1}{2\mu}\nabla^2_{\boldsymbol{R}} - \sum_{i=1}^{n}\frac{1}{8\mu}\nabla_i^2 - \sum_{i>j}\frac{1}{2M_T}\nabla_i\nabla_j - \frac{1}{2}\left(\frac{1}{M_A}-\frac{1}{M_B}\right)\sum_{i=1}^{n}\nabla_{\boldsymbol{R}}\nabla_i,\end{aligned} \tag{1.2}$$

where A and B refer to the two nuclei located at $\boldsymbol{R}_A$ and $\boldsymbol{R}_B$, with masses M_A and M_B and nuclear charges Z_A and Z_B. The total and reduced masses of the molecule are $M_T = M_A + M_B$ and $\mu = M_A M_B / M_T$ respectively, and $R = |\boldsymbol{R}| = |\boldsymbol{R}_A - \boldsymbol{R}_B|$ is the internuclear distance[1].

Given that, for H_2, $M_A = M_B$ and that $M_T, \mu \gg 1$, the mass polarization term $\frac{1}{2M_T}\nabla_i\nabla_j$, the $\frac{1}{8\mu}\nabla_i^2$ term and the last term of the previous Hamiltonian can all be neglected. This chapter will focus on obtaining the set of eigenstates of this Hamiltonian, which are used for the study of photoionization of H_2 with our spectral method.

1.1 The Born-Oppenheimer approximation

Since the problem of diagonalizing a Hamiltonian that simultaneously depends on electronic and nuclear coordinates is generally unmanageable, the usual approach is to separate the full molecular Hamiltonian into a nuclear and an electronic part.

$$\mathcal{H}_0(\boldsymbol{r},R) = \mathcal{H}_{el}(\boldsymbol{r};R) + T_N(R) \tag{1.3}$$

[1] All bold letters denote vectors throughout this thesis unless stated otherwise.

In this separation, the second term corresponds to the nuclear kinetic energy operator, acting on the nuclear coordinates. The first is the electronic Hamiltonian, which encompasses the rest of the terms of 1.2 and depends on the electronic coordinates parameterized by the nuclear configuration. The resulting operators have the following form:

$$\mathcal{H}_{el}(\boldsymbol{r};R) = -\frac{1}{2}\sum_i \nabla^2_{r_i} - \sum_i \frac{Z_A}{|\boldsymbol{r}_i - \boldsymbol{R}_A|} - \sum_i \frac{Z_B}{|\boldsymbol{r}_i - \boldsymbol{R}_B|} + \sum_{i>j} \frac{1}{|\boldsymbol{r}_j - \boldsymbol{r}_i|} + \frac{Z_A Z_B}{R}, \tag{1.4a}$$

$$T_N(R) = -\frac{1}{2\mu}\nabla^2_R. \tag{1.4b}$$

To decouple the diagonalization of the two operators the following *ansatz* for the wave function is proposed:

$$\Psi(\boldsymbol{r},R) = \frac{\chi(R)}{R}\psi(\boldsymbol{r};R). \tag{1.5}$$

This allows us to first diagonalize the electronic Hamiltonian at each nuclear configuration to obtain the set of electronic eigenstates $\{\psi_n\}$ associated with a potential energy curve $E_n(R)$ by solving:

$$\left[\mathcal{H}_{el}(\boldsymbol{r};R) - E_n(R)\right]\psi_n(\boldsymbol{r};R) = 0. \tag{1.6}$$

If *non-adiabatic* effects, responsible for the coupling of different electronic states through nuclear motion, are neglected, the set of vibrational states $\{\chi_{\nu_n}\}$ can then be calculated by solving the eigenvalue equation:

$$\left[T_N(R) + (E_n(R) - W_{n\nu_n})\right]\chi_{\nu_n}(R) = 0 \tag{1.7}$$

where

$$T_N(R) = -\frac{1}{2\mu}\left[\frac{d^2}{dR^2} - \frac{J(J+1)}{R^2}\right]. \tag{1.8}$$

Neglecting non-adiabatic effects is a reasonable assumption based on the different mass of the electrons with respect to the nuclei. Since electrons are much lighter than protons, their motion time scale is much shorter compared to the one of the nuclei. This suggests that electrons instantaneously adapt to any change in the nuclear configuration, what is known as the *adiabatic Born-Oppenheimer approximation* (BO). Given our interest in phenomena happening in the sub-fs domain, this also allows us to completely neglect rotational degrees of freedom whatsoever. Within this approximation we can use a complete set of *vibronic* eigenstates $\{\psi_n \cdot \chi_{\nu_n}\}$ to expand our total wave function including electronic and nuclear degrees of freedom.

Although BO is a very powerful tool widely used in fields that require to perform large quantum many-body calculations, like in quantum chemistry, it is not infallible, and there are many cases in which it *breaks down*. For example, when the characteristic time scales of electronic and nuclear motion become comparable non-adiabatic effects must be taken into account.

1.2 The one-electron molecular wave function

We now proceed to calculate the total molecular two-electron wave function in the framework of the BO approximation. To begin, we start by calculating a set of molecular mono-electronic states in which the total two-electron wave function is expanded. The obvious choice for these mono-electronic functions are the orbitals of the H_2^+ molecular ion, which are obtained by solving the eigenvalue equation:

$$h_{el}\varphi_n = \epsilon_n(R)\varphi_n \tag{1.9}$$

where φ_n are the one-electron orbitals associated with the $\epsilon_n(R)$ potential energy curve, and h_{el} is the electronic Hamiltonian of H_2^+ defined as:

$$h_{el} = -\frac{1}{2}\nabla_{\boldsymbol{r}} - \frac{Z_A}{|\boldsymbol{r}-\boldsymbol{R_A}|} - \frac{Z_B}{|\boldsymbol{r}-\boldsymbol{R_B}|}. \tag{1.10}$$

Being the simplest molecule in the universe this system has been extensively studied, more so since it offers the possibility to solve it exactly, for a fixed internuclear distance, by using prolate spheroidal coordinates [34–37]. Nonetheless, we resort to a one-center expansion in terms of spherical harmonics as the description of continuum states using exact H_2^+ orbitals presents implementation difficulties [38]. Although the previous Hamiltonian does not commute with the total angular momentum operator, thanks to the loss of spherical symmetry with respect to atoms, its commutation with ℓ_z is ensured by virtue of the cylindrical symmetry of the molecule. This results in the azimuthal quantum number ℓ not being a good quantum number to characterize our wave function, whereas the quantum magnetic number m can be used for that purpose. This value corresponds to the projection of the angular momentum onto the internuclear axis, which is placed in the Z direction for convenience. The resulting mono-centric expansion of the H_2^+ orbitals reads as follows:

$$\varphi_n^m(\boldsymbol{r};R) = \sum_{\ell=0}^{\ell_{max}} \frac{U_{n\ell}(r;R)}{r}\mathcal{Y}_\ell^m(\theta,\phi), \tag{1.11}$$

where n corresponds to the quantum number associated with the energy level of the orbital. The use of a mono-centric expansion to describe our wave function may seem counter-intuitive *a priori* given the multi-center nature of molecules, especially if one takes into account that, for large internuclear distances, a considerable angular momentum expansion is needed. This is one of the reasons the usual approach in quantum chemistry is to use multi-centric expansions, which give excellent results for bound states. However, the difficulty to correctly reproduce true molecular continuum states with this kind of expansion, together with the parallelism between 1.11 and the familiar partial wave decomposition of scattering states, makes one-center expansions particularly well suited for the description of continuum states [39].

The radial function $U_{n\ell}(r;R)$ can, in turn, be expanded at each internuclear distance in a basis of B-splines as:

$$U_{n\ell}(r;R) = \sum_{i=1}^{N_B} c_i^{n\ell}(R)B_i^k(r), \tag{1.12}$$

where N_B is the dimension of the B-spline basis set. The B-spline functions, the constituents of the B-spline basis, are piecewise polynomials of order k defined in a

finite closed interval $[0, r_{max}]$ (a box). The junction points between the pieces define a sequence of knots $\{t_i\}_{i=1}^{N_B+k}$ within the box which, in addition, can be used to generate the B-spline basis set with the following recursion expression [40]:

$$B_i^1(r) = \begin{cases} 1 & t_i \leq r \leq t_{i+1} 0 \\ \text{elsewhere} \end{cases} \tag{1.13}$$

$$B_i^k(r) = \frac{r - t_i}{t_{i+k-1} - t_i} B_i^{k-1}(r) + \frac{t_{i+k} - r}{t_{i+k} - t_{i+1}} B_{i+1}^{k-1}(r). \tag{1.14}$$

One of the advantages of these functions is the flexibility they offer to choose the knot sequence in which they are supported. This fact, together with their ability to easily reproduce highly oscillating functions, makes them the perfect candidate to accurately describe the asymptotic behaviour of continuum states[2]. Using B-splines to expand continuum wave functions also grants them the mathematical properties of $\mathcal{L}^2$-integrable functions, characteristic of bound states. Another advantage they posses is that they produce banded matrices in one-electron problems. This greatly simplifies diagonalization and calculation of matrix elements from the computational perspective. All these traits have made B-splines very popular in the study of many problems in atomic and molecular physics over the years [33].

In order to find the eigenvalues of the H_2^+ Hamiltonian in terms of our basis we introduce the aforementioned expansion into 1.9 to obtain the secular equation

$$(\boldsymbol{h} - \epsilon \boldsymbol{S})\, \boldsymbol{c} = 0. \tag{1.15}$$

In the previous matrix equation, $\boldsymbol{c}$ is the vector representing $c_{i\ell}^n$ and $\boldsymbol{h}$ and $\boldsymbol{S}$ are the Hamiltonian and overlap matrices, respectively. Their corresponding matrix elements expressed in terms of the basis set $\left\{B_i^k \cdot \mathcal{Y}_\ell^m\right\}_{i=1,\ell=0}^{N_B,\ell_{\max}}$ read as follows:

$$h_{i\ell,j\ell'} = \int_0^{r_{max}} \int_0^{4\pi} B_i^k(r) \mathcal{Y}_\ell^{m*}(\Omega) h_{el} B_j^k(r) \mathcal{Y}_{\ell'}^m(\Omega) dr d\Omega \tag{1.16a}$$

$$S_{i\ell,j\ell'} = \delta_{\ell\ell'} \int_0^{r_{\max}} B_i^k(r) B_j^k(r) dr, \tag{1.16b}$$

where $\Omega = (\theta, \phi)$. The previous matrix elements are defined for a fixed value of magnetic quantum number m and internuclear distance R. The overlap matrix elements, which appear as result of the B-spline basis set not being orthonormal, are easily calculated thanks to them having minimal support with respect to their degree[3].

Looking at 1.16a, one notices that the Hamiltonian couples different values of ℓ. As mentioned before, the loss of spherical symmetry of the system causes the Hamiltonian to not commute with the angular momentum operator anymore and, as a result, different values of ℓ are coupled via the electron-nucleus interaction potential. This is known as *inter-channel coupling* and plays a major role in the description of the electronic continua. Regarding the description of this electron-nucleus interaction potential, a more convenient way to express the two-center Coulombic

[2] Boundary conditions at the edges of the box, $U_{n\ell}(0) = U_{n\ell}(r_{max}) = 0$, can be fulfilled by just removing the first $B_1^k(r)$ and last $B_{N_B}^k(r)$ B-splines from the set.

[3] This property ensures that $B_i^k(r) \cdot B_j^k(r) = 0$ for $|i - j| \geq k$

potential when using a one-center expansion is in terms of spherical coordinates:

$$V^{(q)} = \frac{1}{|\boldsymbol{r} - \boldsymbol{R}_q|} = \sum_{\ell=0}^{\infty} \frac{r_<^\ell}{r_>^{\ell+1}} \frac{4\pi}{2\ell+1} \sum_{m=-\ell}^{\ell} \mathcal{Y}_\ell^{m*}(\Omega_q)\, \mathcal{Y}_\ell^m(\Omega), \tag{1.17}$$

where $r_< = \min(r, R_q)$, $r_> = \max(r, R_q)$ and Ω_q refers to the angular coordinates of the nucleus q. Taking the origin of our one-center expansion to be the center of mass of the molecule and substituting the Coulomb potential expressed in spherical coordinates into 1.10 we can rewrite our H_2^+ electronic Hamiltonian as:

$$h_{el} = -\frac{1}{2}\frac{d^2}{dr^2} + \frac{\ell(\ell+1)}{2r^2} - \sum_{q=A}^{B} Z_q \sum_{\ell_q=0}^{\infty} \frac{4\pi}{2\ell_q+1} \times \frac{r_<^{\ell_q}}{r_>^{\ell_q+1}} \sum_{m_q=-\ell_q}^{m_q=\ell_q} \mathcal{Y}_{\ell_q}^{m_q*}(\Omega_q)\, \mathcal{Y}_{\ell_q}^{m_q}(\Omega). \tag{1.18}$$

The corresponding matrix elements then take the form:

$$h_{i\ell,j\ell'} = t_{i\ell,j\ell'} + \sum_{q=A}^{B} v^q_{i\ell,j\ell'}, \tag{1.19}$$

with the kinetic energy term

$$t_{i\ell,j\ell'} = \left(-\frac{1}{2}\int_0^{r_{max}} B_i^k(r)\frac{d^2 B_j^k(r)}{dr^2}dr + \frac{\ell(\ell+1)}{2}\int_0^{r_{\max}} \frac{B_i^k(r)B_j^k(r)}{r^2}dr \right)\delta_{\ell\ell'}, \tag{1.20}$$

and the electron nuclear interaction

$$v^q_{i\ell,j\ell'} = -Z_q \sum_{\ell_q=0}^{\infty} \frac{4\pi}{2\ell_q+1} \int_0^{r_{max}} B_i^k(r)\frac{r_<^{\ell_q}}{r_>^{\ell_q+1}} B_j^k(r)dr \times \sum_{m_q=-\ell_q}^{+\ell_q} \mathcal{Y}_{\ell_q}^{m_q*}(\Omega_q) \int \mathcal{Y}_\ell^{m*}(\Omega)\mathcal{Y}_{\ell_q}^{m_q}(\Omega)\mathcal{Y}_{\ell'}^{m}(\Omega)d\Omega. \tag{1.21}$$

where the angular integral with respect to Ω is the usual double integral over solid angle. Computation of the previous matrix elements is straightforward. To begin, our choice of orientation of the molecule along the Z axis with the origin located at the molecular center of mass makes the angular functions of the nuclei, $\mathcal{Y}_{\ell_A}^{m_A*}(\Omega_A)$ and $\mathcal{Y}_{\ell_B}^{m_B*}(\Omega_B)$, to be zero or constant since $(\theta_A, \phi_A) = (0,0)$ and $(\theta_B, \phi_B) = (\pi, 0)$. Then, the angular integrals can be solved analytically using Gaunt's formula which, additionally, enforces selection rules over the possible values ℓ_q effectively putting a cutoff at ℓ_{max}. This means that the quality of the inter-channel coupling will depend on the number of spherical harmonics included in our one-center expansion. Finally, the remaining radial integrals can be solved to machine accuracy using a Gauss-Legendre quadrature.

1.3 The two-electron wave function

Obtaining the two-electron wave function of H_2 is done by diagonalization of the full two-electron Hamiltonian:

$$\mathcal{H}_{el} = \sum_{i=1}^{n} \left[-\frac{1}{2}\nabla_{r_i}^2 - \frac{Z_A}{|\boldsymbol{r}_i - \boldsymbol{R}_A|} - \frac{Z_B}{|\boldsymbol{r}_i - \boldsymbol{R}_B|} \right] + \frac{Z_A Z_B}{R} + \sum_{i>j} \frac{1}{|\boldsymbol{r}_j - \boldsymbol{r}_i|}. \tag{1.22}$$

This Hamiltonian is analogous to the one shown in 1.10 except for the last term accounting for electron-electron repulsion. The appearance of this term adds a new layer of complexity to the problem which mandates that any diagonalization scheme that aspires to accurately describe the multi-electron wave function needs to account for electron correlation. This has been a recurring problem in quantum chemistry over the years and many methods have been proposed for this endeavour. One that has proven to be especially accurate is the *configuration interaction* (CI) method. This method proposes a linear expansion of the total wave function in terms of configuration state functions:

$$\psi^{\Lambda} = \sum_{n_1,n_2} C_{n_1,n_2}^{m_1,m_2} \Phi_{n_1,n_2}^{\Lambda;m_1,m_2}(\boldsymbol{x}_1, \boldsymbol{x}_2) \tag{1.23}$$

where $\Lambda = |M| = |m_1 + m_2|$ and $\boldsymbol{x}_i$ refer to the spatial and spin coordinates of the electron. These configurations state functions are built from antisymmetrized products of one-electron H_2^+ orbitals including spin as follows:

$$\Phi_{n_1,n_2}^{\Lambda;m_1,m_2}(\boldsymbol{x}_1, \boldsymbol{x}_2) = \frac{1}{\sqrt{2}} \left\{ \varphi_{n_1}^{m_1}(\boldsymbol{r}_1)\, \varphi_{n_2}^{m_2}(\boldsymbol{r}_2) \pm \varphi_{n_2}^{m_2}(\boldsymbol{r}_1)\, \varphi_{n_1}^{m_1}(\boldsymbol{r}_2) \right\} \times \frac{1}{\sqrt{2}} \{ \alpha(1)\beta(2) \mp \alpha(2)\beta(1) \}. \tag{1.24}$$

The spin of the electron is introduced by means of the $\alpha\,(\beta)$ spin function with quantum number $\frac{1}{2}\,(-\frac{1}{2})$. Depending on the value of the total spin of the molecule two different wave functions can be built from the same orbitals. For a singlet state with $S = 0$ the spin part of the configuration state function takes the antisymmetric form $\{\alpha(1)\beta(2) - \alpha(2)\beta(1)\}$. Whereas the triplet state with $S = 1$ is represented by its symmetric counterpart $\{\alpha(1)\beta(2) + \alpha(2)\beta(1)\}$. The symmetry of the corresponding spatial part must ensure the total wave function to be antisymmetric as imposed by the Pauli exclusion principle.

The use of a CI expansion also allows expressing two-electron matrix elements, excluding the contribution from electron-electron repulsion, in terms of products of the one-electron matrix elements described in the previous section. The remaining contribution can be calculated first, by expressing the electronic repulsion potential in spherical coordinates as we did for the interchannel-coupling:

$$\frac{1}{|\boldsymbol{r}_1 - \boldsymbol{r}_2|} = \sum_k \frac{r_<^k}{r_>^{k+1}} P_k\left(\cos\theta_{12}\right), \tag{1.25}$$

where θ_{12} is the angle between the position vectors of the two electrons. And then, by employing the auxiliary Z^k function method, standard in atomic calculations [41], to solve the integrals involving the radial coordinates.

With the methodology developed so far, we are able to calculate eigenstates of the H_2 Hamiltonian taking into account electronic and nuclear degrees of freedom, as

well as electron correlations on a basis of B-splines and spherical harmonics. However, with these eigenstates, an accurate description of the photoionization process in the sub-fs time scale is not possible. To achieve this goal different additional steps must be performed depending on the type of state we want to calculate. These types are basically three: bound states, autoionizing states, and continuum states. In the case of bound states, which are characterized by a higher electron density near the nuclei, additional Slater-type orbitals (STOs) are included in the CI expansion to improve its convergence. The inclusion of these states implies the loss of orthogonality and requires the calculation of overlaps. Nevertheless, they greatly improve the description of the ground state at equilibrium internuclear distance. These STOs are of the form:

$$r^n e^{-\gamma_{n\ell} r} \cdot \mathcal{Y}_\ell^m(\Omega) \tag{1.26}$$

with typical values of $n = 1 - 10$ and $\ell = 0 - 11$ and $\gamma_{n\ell} = 2.8$ for all n and ℓ.

The case of autoionizing and continuum states needs special attention given the key role they play in photoionization and the fact that a direct diagonalization of the electronic Hamiltonian using a standard CI expansion is not able to correctly describe any state above the first ionization threshold. Section 1.4 will be devoted to this issue but, before that, it is worth commenting on some properties associated with the symmetry with the two-electron wave function.

1.3.1 Symmetries of the wave function

Diatomic molecules like H_2 belong the $D_{\infty h}$ symmetry point group ($C_{\infty v}$ if they are heteronuclear) because of their axial symmetry. As pointed before, this makes M a good quantum number[4] to characterize the wave function because of the commutation between the Hamiltonian and $L_z = \ell_{1z} + \ell_{2z}$. The two-electron wave function is characterized by a Greek letter based on the absolute value of the z-component of the angular momentum as follows:

$$\begin{array}{rcccc} \text{Value of } \Lambda = |M| & 0 & 1 & 2 & 3 \\ & \updownarrow & \updownarrow & \updownarrow & \updownarrow \\ \text{Code letter} & \Sigma & \Pi & \Delta & \Phi, \end{array}$$

and for one-electron states:

$$\begin{array}{rcccc} \text{Value of } \lambda = |m| & 0 & 1 & 2 & 3 \\ & \updownarrow & \updownarrow & \updownarrow & \updownarrow \\ \text{Code letter} & \sigma & \pi & \delta & \phi. \end{array}$$

Another symmetry associated with the $D_{\infty h}$ point group is the reflection about the XZ plane, corresponding to the operation $y \to -y$ or $\phi \to -\phi$, represented by the operator A_y. This symmetry operation leaves the Hamiltonian invariant, *i.e.*, it commutes, and is related to L_z by $A_y L_z = -L_z A_y$. This implies that, for $M \neq 0$, A_y transforms the wave function into one characterized by the eigenvalue $-M$, which is degenerate in energy. On the other hand, for $M = 0$ there is no degeneracy, and two different Σ states with opposite behavior with respect to the transformation $y \to -y$ appear. To differentiate between the two the signs $\pm$ are used to characterize the wave function.

[4] We will use upper-case letters to refer to properties of the two-electron system and lower-case for the one-electron case

Another symmetry operation that leaves the Hamiltonian invariant is the center symmetry or inversion center, corresponding to the operation $\boldsymbol{r} \to -\boldsymbol{r}$ or $(r, \theta, \phi) \to (r, \pi - \theta, \phi + \pi)$, represented by the operator i. This symmetry operation also commutes with L_z so wave functions with a given value of M may be classified according to their behaviour under this operation. The two possible outcomes of applying this operator are to leave the wave function unchanged, *gerade* states (g), or changing its sign, *ungerade* states (u). Because of our one-center expansion, inversion symmetry only affects the spherical harmononic functions and, since spherical harmonics have defined parity ($\mathcal{Y}_l^m(\pi - \theta, \phi + \pi) = (-1)^\ell \mathcal{Y}_l^m(\theta, \phi)$), only even values of angular momentum contribute to *gerade* symmetry while the odd ones do so for *ungerade* symmetry.

These symmetry operations, the total spin of the molecule and the z component of the total spin of the molecule form the set of operators $\Omega \equiv \{S^2, S_z, L_z, A_y, i\}$ that, together with the Hamiltonian, form a complete set of commutable observables. Our wave function is built to simultaneously be an eigenstate of this set with eigenvalues $\Omega \equiv \{S(S+1), M_s, \pm\Lambda, \pm, g/u\}$. This allows us to perform a block diagonalization of the Hamiltonian for each set of eigenvalues.

1.4 Feshbach formalism

As indicated previously, in the study of photoionization, continuum states and resonances play a key role, even more so than bound states. For a correct description of states that lie above the first ionization threshold a direct diagonalization of the total Hamiltonian in an infinite domain, including all electronic and nuclear degrees of freedom, and including all ionization channels would be needed. In order to tackle this unmanageable task, we employed an adaptation of the stationary Feshbach theory [42, 43]. Originally developed for the study of nuclear reactions, Feshbach's projector operator formalism is now a key tool in the study of scattering processes in many-body systems. The method was first introduced in atoms by O'Malley *et al* [44] and later introduced in molecules by the seminal works of Bardsley [45] and Hazi, Rescigno and Kurilla [46]. Following their pioneering ideas, Martín *et al* developed a theoretical framework for the study of electron-nuclear coupled dynamics in photoionization of molecules [47–49], which is the method adopted in the present work.

In the calculation of continuum states and resonances in the continuum two problems emerge when diagonalizing the electronic Hamiltonian using a CI scheme like the one explained in the previous section. The first one stems from the impossibility to obtain the correct asymptotic behavior for continuum states since diagonalization is performed in a finite spatial domain. This problem, and the procedure to overcome it, will be detailed later. The second problem comes from the presence of Feshbach resonances, appearing as doubly excited states, which cannot be properly described in the context of the BO approximation. Doubly excited states are quasi-bound metastable states that appear in the continuum part of the spectrum of multi-electronic atoms and molecules. Being unstable, these states end up decaying into the continuum in a process called autoionization. The characteristic time of this process competes with that of nuclear motion, hence the reason they cannot be properly described in the BO framework. To solve this, Feshbach's formalism introduces two projection operators that allow treating the resonant and non-resonant contributions of the total wave-function separately. These projector operators fulfill the following properties:

- Completeness: $\mathcal{P} + \mathcal{Q} = \mathbb{1}$
- Idempotency: $\mathcal{P}^2 = \mathcal{P}, \quad \mathcal{Q}^2 = \mathcal{Q}$
- Orthogonality: $\mathcal{P}\mathcal{Q} = \mathcal{Q}\mathcal{P} = 0$

Applying these projectors to the total wave-function of the system, including electronic and nuclear degrees of freedom, we get:

$$|\Psi\rangle = \mathcal{Q}|\Psi\rangle + \mathcal{P}|\Psi\rangle, \tag{1.27}$$

where $\mathcal{P}|\Psi\rangle$ represents the scattering-like part and $\mathcal{Q}|\Psi\rangle$ the $\mathcal{L}^2$-integrable part of the total wave function with to the following asymptotic behaviour:

$$\lim_{r\to\infty} \mathcal{P}|\Psi\rangle = |\Psi\rangle \qquad \lim_{r\to\infty} \mathcal{Q}|\Psi\rangle = 0. \tag{1.28}$$

One advantage of this formalism is that non-adiabatic effects within each subspace are expected to be small [49], so the BO approximation remains valid if we restrict ourselves to operators coupling states of the same subspace. This issue will be further developed in Chapter 3 as well as the case of operators that couple the two different subspaces, which are responsible for autoionization.

1.4.1 Non-resonant electronic continuum

Eigenfunctions of the electronic Hamiltonian whose eigenvalues belong to the continuum part of the spectrum are called (electronic) continuum states and represent an ionization situation. Analogously, the continuum eigenfunctions of the nuclear Hamiltonian, continuum nuclear states, are associated with dissociation. This subsection will be devoted to the development of the necessary tools to describe electronic continuum states. The case of nuclear continuum states will be reviewed in the last section of this chapter when discussing nuclear motion.

Non-resonant continuum electronic states are equivalent to scattering states representing a free electron interacting with the remaining parent ion core. These states lay above the first ionization threshold of atoms and molecules and are eigenstates of the $\mathcal{P}$ projected Hamiltonian:

$$[\mathcal{P}\mathcal{H}_{el}\mathcal{P} - E]\, \psi_{\mu}^{\varepsilon_\mu}(\boldsymbol{r}; R) = 0, \tag{1.29}$$

where $\mu = (\alpha, \ell_\alpha)$ represents a particular ionization channel and $\epsilon_\mu = \varepsilon_\alpha$. This wave function represents a system with total energy $E = E_\alpha(R) + \varepsilon_\alpha$ composed of an ionized electron with kinetic energy ε_α and angular momentum ℓ_α leaving the core in the α ionic state, or the α ionization threshold of the molecule, with energy $E_\alpha(R)$. In our case, α are the different eigenstates of the electronic Hamiltonian of H_2^+, associated with given potential energy curve $E_\alpha(R)$, obtained from solving equation 1.9. To obtain the states belonging to the $\mathcal{P}$ subspace our approach does not resort to an explicit diagonalization of $\mathcal{P}\mathcal{H}_{el}\mathcal{P}$. Instead, we use multichannel scattering theory to evaluate electronic continuum states from a basis that spans the $\mathcal{P}$ subspace by solving the following equation:

$$[\mathcal{H}_{el} - E]\, \mathcal{P}\Psi_{\mu E}^{\Omega-}(\boldsymbol{r}, R) = 0, \tag{1.30}$$

where μ represents the collective index channel introduced earlier and E is the total energy of the system. The solutions to the previous equation are built to be eigenfunctions of the set of operators $\Omega \equiv \{S^2, S_z, L_z, A_y, i\}$ discussed in the last section of the previous chapter and satisfy incoming boundary conditions.

Ionization can be viewed as a half collision between an electron and its parent ion. In this context, quantum scattering theory becomes a very powerful tool to correctly describe the wave function of such a system. For a simple relation with experimentally measurable states scattering theory imposes incoming boundary conditions corresponding to an outgoing electron in a particular channel μ, characterized by the state of the ion and its coupling with the outgoing electron and by well-defined ionic and electronic energies [50]. These incoming boundary conditions are often portrayed by the following asymptotic behavior of the wavefunction [51]:

$$\Psi_E^- \underset{r\to\infty}{\sim} e^{i\boldsymbol{k}\cdot\boldsymbol{r}} + f^-(\theta,\phi)\frac{e^{-ikr}}{r}, \tag{1.31}$$

where $f^-(\theta,\phi)$ represents the usual scattering amplitude. These states reflect the fact that the free particle is associated with an outgoing flux and, as a result, have to be normalized to a Dirac delta function:

$$\langle \Psi_E^- | \Psi_{E'}^- \rangle = \delta(E - E'). \tag{1.32}$$

A common technique employed in scattering problems is to expand the scattering wave function in partial waves. This is based on the fact that, far from the interacting region, the motion of an ionized electron is mainly dictated by the radially symmetric Coulomb interaction with the remaining ion, whether it is of atomic or molecular origin. Because of the central nature of the potential in the asymptotic region, the wave function corresponding to that electron can be expanded in partial waves that conform to incoming-wave boundary condition as given by [52]:

$$\Psi_E^- \sim \sum_{\ell m} i^\ell e^{-i\sigma_\ell(E)} \mathcal{Y}_\ell^m(\Omega_r)\psi_{\ell m E}(r)\mathcal{Y}_\ell^{m*}(\Omega_k). \tag{1.33}$$

where $\psi_{\ell m E}(r)$ is the solution of the radial Schrödinger equation, $\Omega_r = (\theta_r, \phi_r)$ and $\Omega_k = (\theta_k, \phi_k)$ are the angles of the position and momentum vectors of the ionized electron, respectively, and all coordinates are referred to the laboratory frame. Our method makes use of this expansion in the calculation of the different ionization channel wave functions and, later, for the determination of molecular frame angular distributions (MFPADs). The similarities of this expansion with our one-center expansion of the H_2^+ orbitals also present many advantages from the implementation point of view.

Normalization of continuum states

The use of a finite box to diagonalize the Hamiltonian leads to a discretized spectrum. This is the reason why using B-splines to expand continuum wave functions grants them the mathematical properties of $\mathcal{L}^2$-integrable wave functions. Although this has many advantages when computing matrix elements, it gives continuum states a finite norm like the one bound states posses:

$$\langle \psi_i | \psi_j \rangle = \delta_{ij}. \tag{1.34}$$

As mentioned earlier, incoming boundary conditions impose the norm of continuum wave functions to be normalized in the distribution sense, as portrayed in equation 1.32. Discretized continuum states can acquire this normalization, under certain conditions defined later, by means of a multiplicative factor applied to the wave function obtained from the diagonalization process:

$$\psi_{E_n} = \rho(E_n)^{1/2}\psi_n. \tag{1.35}$$

This normalization factor is obtained from the density of states $\rho(E_n)$. One method to obtain this density of states is by direct comparison with exact solutions in the asymptotic region. This requires prior knowledge of the exact solutions and placing B-splines far away from the interaction region [53]. Another method is to use the discretized spectrum obtained from diagonalization to calculate the density of states. This method has been the subject of many studies [38] as it does not require previous knowledge of the exact solutions. Provided that the relationship between the eigenvalues E_n and their index n behaves like a monotonic function $E(n)$, the density of states can be expressed as:

$$\rho\left(E_n\right) = \left|\frac{\partial E_{n'}}{\partial n'}\right|^{-1}_{n'=n}. \tag{1.36}$$

Through a Taylor expansion up to third order, one obtains the formal expression

$$\left.\frac{\partial E(n')}{\partial n'}\right|_{n'=n} = \frac{E_{(n+1)} - E_{(n-1)}}{2} + \frac{1}{6}\left.\frac{\partial^3 E(n')}{\partial n'^3}\right|_{n'=n} \tag{1.37}$$

where the second order term is depreciated in the basis that, for large enough E, the continuum energy can be approximated to the energies of the particle in a box:

$$E_n = \frac{n^2\pi^2}{2r_{max}^2}. \tag{1.38}$$

This, together with the weak curvature of the function $E(n)$, allows us to accurately approximate the density of states by the simple relation [54]:

$$\rho\left(E_n\right) \approx \frac{2}{E_{(n+1)} - E_{(n-1)}}. \tag{1.39}$$

Although the method outlined here to get the correct asymptotic behaviour for discretized continuum states is effective for single-channel situations, a simple multiplicative factor will not yield the correct incoming boundary conditions for the multichannel case. Our multichannel approach starts first with the computation of single-channel uncoupled continuum wave functions for each channel μ, the so called uncoupled continuum states (UCSs). For this reason we will first start outlining some general properties of single-channel uncoupled continuum wave functions and then proceed to explain the multichannel case.

The single-channel continuum wave function

In atomic systems, unlike for molecules, the calculation of electronic continuum wave functions lying just above the first ionization threshold is a single-channel scattering problem where each channel can be associated with a given partial wave uncoupled from the rest. Nevertheless, the asymptotic behavior of these states linked

to the effect of the Coulomb potential at $r \to \infty$, as well as the effect of the remaining electrons in the ionic core, is easily extended to the multichannel situation.

One of the reasons the asymptotic behavior of an ionized electron is not well represented by the solutions of the Hamiltonian of a free particle, like a plane wave, is the slow decay of the Coulomb interaction with distance. This potential falls as r^{-1} making its influence to be felt even for $r \to \infty$. The partial wave of a photoelectron moving in a Coulomb potential in the asymptotic region can be expressed as a linear combination of regular and irregular Coulomb functions as [55]:

$$\psi_{\ell E}(r) \sim \frac{1}{r}\left[F_{\ell E}(r) - \pi K_\ell(E) G_{\ell E}(r)\right]. \tag{1.40}$$

where $K_\ell(E)$ is the reaction amplitude, the single-channel analogous of the **K**-matrix, which, in turn, is related to the usual scattering amplitude $\mathcal{S}_\ell$, analogous to the **S**-matrix, by:

$$\mathcal{S}_\ell = \frac{1 - i\pi K_\ell}{1 + i\pi K_\ell}. \tag{1.41}$$

The reaction amplitude represents the ratio of G_ℓ with respect to F_ℓ and is associated with the short-range central potential caused by the remaining electrons of the ion-core[5].

By making use of the analytic properties of the Coulomb regular and irregular functions to express the partial waves from equation 1.40 and changing to a representation in terms of the scattering amplitude instead of the reaction amplitude we obtain [56]:

$$\lim_{r\to\infty} \psi_{\ell E}(r) = \sqrt{\frac{1}{2\pi k}}\frac{1}{ir}\left(e^{i\theta_\ell} - \mathcal{S}_\ell^{\Omega\dagger} e^{-i\theta_\ell}\right) \tag{1.42}$$

with

$$\theta_\ell = kr - \frac{1}{2}\ell\pi + \frac{Z}{k}\log(2kr) + \sigma_\ell(k) \tag{1.43a}$$

$$\sigma_\ell(k) = \arg\Gamma(\ell + 1 - iZ/k) \tag{1.43b}$$

$$\mathcal{S}_\ell^{\Omega\dagger} = e^{-2i\delta_\ell}. \tag{1.43c}$$

The quantities δ_ℓ and σ_ℓ are the short-range and Coulomb phase shifts, respectively. They represent the deviation of the radial part of a partial wave in the asymptotic region associated with the short-range and Coulomb potentials with respect to the case of a free electron.

The multichannel continuum wave function

For molecules, the short-range potential is not central anymore. That means that the potential can transfer angular momentum to the ionized electron effectively coupling different partial waves. Unlike for the case of atoms, in which the problem of calculating the scattering wave function of the electronic continuum lying just above the first ionization threshold can be treated as a single-channel problem, for molecules, it is always a multichannel problem [49].

For H_2^+ the corresponding asymptotic partial waves can be expressed, following a similar procedure as the one for single-channel problems, in terms of regular and

[5]For hydrogenic ions the exact solution is the regular Coulomb function F_ℓ. When more electrons are present the solution with condition of regularity at the origin must be evaluated numerically, asymptotically the presence in equation 1.40 of the irregular function G_ℓ is a signature of the multi-electronic character of the atom and in particular of the screening effects in the core region [55].

irregular Coulomb spherical waves as [55]:

$$\psi_{\ell E}(\boldsymbol{r}) \sim \frac{1}{r}\left[f_{\ell E}(r)\mathcal{Y}_{\ell}^{m}(\Omega) - \sum_{\ell'}\pi K_{\ell\ell'}(E)g_{\ell' E}(r)\mathcal{Y}_{\ell'}^{m}(\Omega)\right] \tag{1.44}$$

where $K_{\ell\ell'}$ are the elements of the reaction matrix $\boldsymbol{K}$, which can be related to the usual scattering matrix $\boldsymbol{\mathcal{S}}$ in an analogous way as in 1.41, by the following expression:

$$\boldsymbol{\mathcal{S}} = \frac{\mathbb{1} - i\pi\boldsymbol{K}}{\mathbb{1} + i\pi\boldsymbol{K}}. \tag{1.45}$$

Equation 1.44 illustrates the coupling between different partial waves at a given energy that occurs in molecules.

Fixed boundary conditions at the edges of the box, which force $U_{nl}(0) = U_{nl}(r_{max}) = 0$, when solving the eigenvalue equation for the one-electron orbitals 1.15, remove the ℓ-degeneracy of the different partial waves at a given energy. This loss of degeneracy of the energy spectrum is caused by the need to solve a different problem for each ℓ when calculating in a box due to the centrifugal barrier. As a result, inter-channel coupling is not described correctly when employing discretization techniques like ours. This may not be critical for single-channel problems where this fact may be easily fixable or not even be an issue at all. But, when the non-central ionic potential couples different values of ℓ, calculating a continuum wave function at a given energy with the correct asymptotic behaviour from a direct diagonalization becomes impossible. Instead we get functions that satisfy arbitrary boundary conditions of the form:

$$\psi_{\ell E}(\boldsymbol{r}) \sim \frac{1}{r}\left[a_{\ell\ell' n}f_{\ell' E_n}(r)\mathcal{Y}_{\ell'}^{m}(\hat{\mathbf{r}}) + b_{\ell\ell' n}g_{\ell' E_n}(r)\mathcal{Y}_{\ell'}^{m}(\hat{\mathbf{r}})\right]. \tag{1.46}$$

The coefficients $a_{\ell\ell' n}$ and $b_{\ell\ell' n}$ can be calculated by fitting the obtained solutions to to linear combinations of the asymptotic form of the regular and irregular Coulomb functions at an energy $E = E_n$ using a least-square approach. The reader is referred to [57,58] for successful applications of this method in photoionization of molecules.

If we want to study inelastic processes, like photoionization, additional ionic thresholds have to be included in the definition of the different ionization channels. In addition to the coupling between different partial waves, the coupling between different ionization thresholds must also be taken into account. Again, it is not possible to obtain a wave function satisfying this condition from a direct diagonalization as a result of the poor description of inter-channel coupling. To include these threshold in the molecular two-electron scattering wave function we make use of a close-coupling expansion. This expansion consists on expressing the scattering wave function as an antisymmetrized product of ionic sates α, and a function representing the ionized electron in a well defined channel $\mu = (\alpha, \ell_\alpha)$. Our scattering two-electron wave function for a given channel μ and total electronic energy E is then written in terms of a multichannel close-coupling expansion as:

$$\mathcal{P}\Psi_{\mu E}^{\Omega^-}(\boldsymbol{r}_1, \boldsymbol{r}_2, R) = \Theta\sum_{\mu'}^{N_c}\left[\varphi_{\mu'}^{\Omega}(\boldsymbol{r}_1, \hat{\boldsymbol{r}}_2)\, F_{\mu\mu'}^{\Omega^-}(r_2)\right] \tag{1.47}$$

where the spin part has been factored out for simplicity. In the previous expression, Θ is the symmetrization (antisymmetrization) operator for the singlet (triplet)

state, N_c is the number of channels included, $\varphi^{\Omega}_{\mu'}$ represents the states of the H_2^+ molecular ion coupled with the angular functions of the scattered electron so that the whole ion-electron system is an eigenfunction of the set of operators Ω, and $F^{\Omega-}_{\mu\mu'}$ is the coupled partial wave of the ionized electron. multichannel incoming boundary conditions mandate that, asymptotically, there can only be one outgoing spherical Coulomb wave in the μ channel, whereas there are incoming spherical Coulomb waves in all channels labeled $\mu' = 1, \ldots, N_c$:

$$\lim_{r\to\infty} F^{\Omega-}_{\mu\mu'} = \sqrt{\frac{1}{2\pi k_\mu}}\frac{1}{ir}\left(\delta_{\mu\mu'}e^{i\theta_\mu} - \mathcal{S}^{\Omega\dagger}_{\mu\mu'}e^{-i\theta_{\mu'}}\right) \tag{1.48}$$

with analogous definition as those of the single-channel case

$$\theta_\mu = k_\mu r - \frac{1}{2}\ell_\mu\pi + \frac{Z}{k_\mu}\log\left(2k_\mu r\right) + \sigma_{\ell_\mu}\left(k_\mu\right) \tag{1.49a}$$

$$\sigma_{\ell_\mu}\left(k_\mu\right) = \arg\Gamma\left(\ell_\mu + 1 - iZ/k_\mu\right) \tag{1.49b}$$

$$\mathcal{S}^{\Omega\dagger}_{\mu\mu'} = e^{-2i\delta_\mu}. \tag{1.49c}$$

In principle, all possible ionization channels should be included in the close-coupling expansion to retrieve the true continuum wave function for a given channel but, in practice, only a handful of channels exhibit a significant coupling so that they need to be taken into consideration. For the number of ionic thresholds to be incorporated in the expansion the criterion used is whether they constitute energetically open or closed channels. These criteria are dictated by the total electronic energy E, for open channels $\varepsilon_\alpha = E - E_\alpha(R) \geq 0$ and for closed channels $\varepsilon_\alpha \leq 0$. In reality, even if only the first ionization threshold is included in the expansion, the number of open channels is still infinite considering that the ionized electron can be represented by an infinite number of partial waves. For continuum states of symmetry $^1\Sigma_u^+$ in the region below the second ionization threshold $2p\sigma_u$ the set of open channels would be $\{\mu_1\} = [\alpha_1 = H_2^+(1s\sigma_g), \ell_{\alpha_1} = 1, 3, 5, \ldots, \infty]$. Fortunately, the partial wave expansion converges rather quickly with ℓ and only a small number of partial waves needs to be taken into account.

Our $\mathcal{L}^2$ multichannel close-coupling method first requires us to calculate the single-channel electronic uncoupled continuum states for each separate channel μ' in equation 1.47, the already mentioned uncoupled continuum states (UCSs). These states correspond to a continuum state evaluated at a given ionic threshold α and angular momentum ℓ_α and are analogous to the static exchange wave function:

$$\zeta^0_{\mu E} = \Theta\left(\varphi^{\Omega}_{\mu}\left(\mathbf{r}_1, \hat{\mathbf{r}}_2\right) F^{\Omega-}_{\mu E}\left(r_2\right)\right). \tag{1.50}$$

Although these states correspond to asymptotically observable situations of the ion-electron system [50], they are not eigenstates of the electronic Hamiltonian because of the lack of inter-channel coupling, hence they are not true scattering states. To obtain the true multichannel continuum wave function $\mathcal{P}\Psi^{\Omega-}_{\mu E}$ with the appropiate boundary conditions from 1.48, we introduce the inter-channel coupling between UCSs by means of the Lippmann-Schwinger formalism. We obtain the UCSs by diagonalization of the μ projected electronic Hamiltonian $P_\mu\mathcal{H}_{el}P_\mu$, where P_μ is an angular momentum channel projector operator with the following properties:

$$P_\mu\zeta^0_{\mu E} = \zeta^0_{\mu E} \quad P_\mu P_{\mu'} = \delta_{\mu\mu'}P_\mu. \tag{1.51}$$

As mentioned before, we obtain the scattering wave function at a given energy E with the correct incoming boundary conditions by means of the Lippmann-Schwinger equations as

$$\mathcal{P}\Psi^{\Omega-}_{\mu E} = \zeta^0_{\mu E} + G^-_P(E)V\zeta^0_{\mu E} \tag{1.52}$$

where V is the inter-channel coupling, corresponding to the non-block diagonal terms of $\mathcal{H}_{el}$ connecting different channels $\mu \neq \mu'$, defined as

$$V = \sum_{\substack{\mu\mu' \\ \mu\neq\mu'}} P_\mu \mathcal{H}_{el} P_{\mu'} \tag{1.53}$$

and $G^-_p(E)$ is the coupled Green operator defined as

$$G^-_p(E) = \lim_{\eta\to 0} \frac{1}{E - \mathcal{H}_{el} + i\eta}. \tag{1.54}$$

The matrix elements of the coupled Green operator can be easily obtained following the procedures described in [47,59–61]. Formally, this operator is defined through a Dyson series of the uncoupled Green operator and the inter-channel coupling as

$$G^-_P(E) = G^-_0(E) + G^-_0(E)VG^-_P(E) \tag{1.55}$$

where

$$G^-_0(E) = \lim_{\eta\to 0} \frac{1}{E - \sum_\mu P_\mu \mathcal{H}_{el} P_\mu + i\eta}. \tag{1.56}$$

Some final remark need to be made before we are able to calculate $\mathcal{P}\Psi^{\Omega-}_{\mu E}$ with the $\mathcal{L}^2$ multichannel close-coupling approach developed so far. For the calculation of the coupled Green operator matrix elements all UCSs must have the same energy spectrum $E_{\mu n}$. This is particularly crucial if one wants to study nuclear motion where this requirement extends to all internuclear distances. As mentioned before, this is not possible due to the loss of ℓ-degeneracy of the discretized spectrum obtained from diagonalization. To overcome this issue we opt to introduce a step potential potential in the one-electron Hamiltonian h_{el} that fulfills $V(r) = 0$ for $r < r_0$ and $V(r) = \infty$ for $r > r_0$. By shifting the parameter r_0 we can match the energies of the UCSs to a previously defined energy grid. It is important that this energy grid is built to reproduce the density of states of a particle in a box in order to avoid big displacements of r_0 that would result in a loss of orthogonality. The final continuum wave function for channel μ with total electronic energy E obtained from a set of discretized UCSs $\{\zeta^0_{\mu n}\}$ can be written as:

$$\mathcal{P}\Psi^{\Omega-}_{\mu E_{\mu n}} = \rho^{1/2}_\mu(E_{\mu n}) \left(\zeta^0_{\mu n} + \sum_{\mu' n'} \sum_{\mu'' n''} \left\langle \zeta^0_{\mu' n'} \middle| G^-_P(E_{\mu n}) \middle| \zeta_{\mu'' n''} \right\rangle \times \left\langle \zeta^0_{\mu'' n''} | V | \zeta^0_{\mu n} \right\rangle \zeta^0_{\mu' n'} \right). \tag{1.57}$$

1.4.2 Resonances in the continuum

To obtain the states belonging to the $\mathcal{Q}$ subspace, the resonant $\psi_r \equiv \mathcal{Q}\psi_r$ states, one needs to diagonalize the Feshbach $\mathcal{Q}$-projected electronic Hamiltonian.

$$[\mathcal{Q}\mathcal{H}_{el}\mathcal{Q} - E_r]\,\psi_r\,(\boldsymbol{r}; R) = 0 \tag{1.58}$$

The actual calculation though, is performed by diagonalizing the total electronic Hamiltonian using a CI expansion, similarly to the case of bound states, in which selected configurations have been removed. Unlike for the case of the non-resonant continuum, resonant states can be accurately described using an $\mathcal{L}^2$ basis set since they represent localized states, as their asymptotic behaviour suggests in 1.28.

We make use of the orthogonality between the $\mathcal{P}$ and $\mathcal{Q}$ projectors to effectuate the truncation of the configuration space. The two-electron Feshbach projector $\mathcal{P}$ for a given threshold α can be written in terms of one-electron operators as

$$\mathcal{P}_\alpha(1,2) = \mathcal{P}_\alpha(1) + \mathcal{P}_\alpha(2) - \mathcal{P}_\alpha(1)\mathcal{P}_\alpha(2), \tag{1.59}$$

with

$$\mathcal{P}_\alpha(i) = |\psi_\alpha(i)\rangle\langle\psi_\alpha(i)| \tag{1.60}$$

where ψ_α corresponds to an ionic threshold of the molecule, namely, a state of H_2^+. The $\mathcal{Q}_\alpha$ projector operator is then easily found taking into account that $\mathcal{Q}_{\alpha=n} = 1 - \sum_{i=1}^{n}\mathcal{P}_{\alpha=i}$. With this projector we obtain the resonant states laying between the αth and $\alpha th + 1$ ionization thresholds with energy between $E_\alpha(R)$ and $E_{\alpha+1}(R)$. This way to build the $\mathcal{Q}$ subspace by separately calculating the different series of Rydberg states associated to each ionization threshold is more convenient than to build a single $\mathcal{Q}$ subspace. In practice, this means that to calculate the $\mathcal{Q}_1$ series we have to remove from the diagonalization process configurations containing the $1s\sigma_g$ orbital, for the $\mathcal{Q}_2$ series we should remove configurations containing the $1s\sigma_g$ and the $2p\sigma_u$ orbitals and so on.

As mentioned before, this states are metastable and have a finite lifetime. This lifetime is defined as the inverse of the autoionization width, $\tau = 1/\Gamma_r$, which, in turn, is defined as:

$$\Gamma_r(E,R) = \sum_\mu \Gamma_{r\mu} = 2\pi \sum_\mu \langle\psi_r|\mathcal{Q}\mathcal{H}\mathcal{P}|\psi_{\mu E}^{\Omega-}\rangle. \tag{1.61}$$

In Chapter 3 a more detailed description of autoionization will be given when discussing the propagation schemes used for our study of photoionization in time.

1.5 Nuclear motion

As discussed in section 1.1, the calculation of the vibrational states of H_2 in the framework of the BO approximation is performed by solving the eigenvalue equation:

$$\left\{-\frac{1}{2\mu}\frac{d^2}{dR^2} + \frac{J(J+1)}{2\mu R^2} + E_n(R)\right\}\chi_{n\nu}(R) = W_{n\nu}\chi_{n\nu}(R), \tag{1.62}$$

where μ is the reduced mass of the molecule, $W_{n\nu}$ is the total energy of the molecule and $E_n(R)$ is the nth electronic potential energy curve. In orther to solve the above equation we expand our vibrational wave function in a basis set of B-splines in a

similar fashion as what we did for the one-electron orbitals in section 1.2

$$\chi_{n\nu}(R) = \rho_{n\nu}^{1/2} \sum_{i}^{N_R} d_i^{n\nu} B_i^k(R), \tag{1.63}$$

where $\rho_{n\nu}$ corresponds to the density of nuclear states. When the nuclear wave function corresponds to a bound vibrational state this quantity equal to one to ensure the correct normalization of bound states to a Kronecker delta. Analogously to the case of continuum electronic states, when the nuclear wave function corresponds to a dissociative state, we need to impose the correct normalization to the wave function coming from a diagonalization using an $\mathcal{L}^2$ basis. The density of states associated with the nuclear continuum can be calculated in a similar fashion as we did for the electronic density of states.

$$\rho_{n\nu} = \frac{2}{W_{n(\nu+1)} - W_{n(\nu-1)}} \tag{1.64}$$

Photodissociation must be understood as a half collision without entrance channels [49]. Consequently, the nuclear wave functions belonging to the continuum must satisfy the corresponding asymptotic boundary conditions of a single-channel scattering problem

$$\lim_{R\to\infty} \chi_{n\nu}(R) = \frac{1}{R}\sqrt{\frac{m_\mu}{2\pi k_{n\nu}}} \left(e^{i\theta_{n\nu}} - \mathcal{S}_{n\nu}^{\dagger} e^{-i\theta_{n\nu}} \right) \tag{1.65}$$

with

$$\theta_{n\nu} = k_{n\nu} R - J\pi/2 \qquad \mathcal{S}_{n\nu} = e^{-2i\Delta_{n\nu}(k_{n\nu})} \tag{1.66}$$

where $k_{n\nu}$ is the nuclear momentum and $\Delta_{n\nu}(k_{n\nu})$ is the short-range nuclear phase shift, that can be extracted by fitting the real nuclear wave function obtained from the diagonalization procedure to the known asymptotic analytic form

$$\lim_{R\to\infty} \chi_{n\nu}(R) = \frac{1}{R}\sqrt{\frac{2m_\mu}{\pi k_{n\nu}}} \sin\left(\theta_{n\nu}\left(k_{n\nu}\right) + \delta_{n\nu}\left(k_{n\nu}\right)\right) \tag{1.67}$$

at the end of the nuclear box. The inclusion of this phase shift in the nuclear wave function, by multiplication of the factor $e^{-i\Delta_{n\nu}(k_{n\nu})}$, is an unavoidable requirement if one is interested in studying interference of nuclear wave-packets dissociating through different potential energy curves.

Chapter 2

Matter-Radiation Interaction

2.1 Classical description of electromagnetic radiation

In order to study phenomena related to the interaction of electromagnetic radiation with matter in the quantum domain, one needs to assess how to represent said electromagnetic radiation. Two approaches can be made, either to consider a classical description of radiation based on Maxwell's theory of the electromagnetic field or to adopt a quantum description of the field as dictated by quantum electrodynamics. Mathematically, the two theories have very different treatments. In the classical theory of radiation, the electromagnetic field is represented by a classical vector field defined at each space-time point whereas, in quantum electrodynamics, it is represented by a field operator (or quantized field) acting on state vectors in occupation number space (photons) [62,63]. Although quantum electrodynamics gives the most fundamental description of electromagnetic radiation in nature, in the classical limit, both classical and quantum theories are equivalent. When the number of photons becomes so large that the occupation number can be regarded as a continuous variable, a quantum description of radiation becomes unnecessary and computationally prohibitive. This is not true for processes such as spontaneous emission where occupation numbers can be as low as one and quantization of radiation is mandatory to correctly describe these kinds of processes. Considering the typical intensities attainable with HHG and FEL laser sources being in the range of $10^9 - 10^{17}$ W cm^{-2} which, for XUV and soft X-ray photons, correspond to $10^6 - 10^{14}$ photons per shot [64,65] it is safe to assume that a quantum description of radiation is not needed. We thus follow a *semi-classical* approach in the study of photoionization where the electromagnetic field is treated classically and the molecular target, as discussed in the previous chapter, is described fully quantum-mechanically.

2.1.1 Maxwell equations

The classical description of electromagnetic radiation is expressed by means of the Maxwell equations which, for radiation in a vacuum (no external charges or currents), take the following form:

$$\boldsymbol{\nabla} \cdot \boldsymbol{E} = 0 \tag{2.1}$$

$$\boldsymbol{\nabla} \cdot \boldsymbol{B} = 0 \tag{2.2}$$

$$\boldsymbol{\nabla} \times \boldsymbol{E} = -\partial_t \boldsymbol{B} \tag{2.3}$$

$$\boldsymbol{\nabla} \times \boldsymbol{B} = \frac{1}{c^2} \partial_t \boldsymbol{E} \tag{2.4}$$

where $\boldsymbol{E}(\boldsymbol{r},t)$ and $\boldsymbol{B}(\boldsymbol{r},t)$ are the electric and magnetic fields respectively. These four field equations can be rewritten with the introduction of the scalar and vector potentials.

Analogous to the definition of the scalar potential, which is a scalar field whose gradient is a vector field, we can define a vector potential $\boldsymbol{A}$ whose curl is a vector field $\boldsymbol{v} = \boldsymbol{\nabla} \times \boldsymbol{A}$. We can associate this new vector field to the magnetic field by taking into account that the divergence of the curl of a vector is always zero, $\boldsymbol{\nabla} \cdot (\boldsymbol{\nabla} \times \boldsymbol{A}) = 0$, which makes v a solenoid vector field like $\boldsymbol{B}$. The magnetic field can then be expressed in terms of the curl of the vector potential as:

$$\boldsymbol{B} = \boldsymbol{\nabla} \times \boldsymbol{A} \tag{2.5}$$

From equation 2.3 we have

$$\boldsymbol{\nabla} \times \boldsymbol{E} = -\partial_t \boldsymbol{B} = -\partial_t (\boldsymbol{\nabla} \times \boldsymbol{A}) \tag{2.6}$$

which can be rewritten as

$$\boldsymbol{\nabla} \times (\boldsymbol{E} + \partial_t \boldsymbol{A}) = 0. \tag{2.7}$$

Since the curl of the gradient of a scalar field is always zero ($\boldsymbol{\nabla} \times (\boldsymbol{\nabla}\phi) = 0$) we can define the expression inside the parenthesis as:

$$\boldsymbol{E} + \partial_t \boldsymbol{A} = -\boldsymbol{\nabla}\phi \tag{2.8}$$

or, equivalently:

$$\boldsymbol{E} = -\boldsymbol{\nabla}\phi - \partial_t \boldsymbol{A}. \tag{2.9}$$

With these new expressions equations 2.1 and 2.4 turn into:

$$-\nabla^2 \phi = \partial_t \boldsymbol{\nabla} \cdot \boldsymbol{A} \tag{2.10}$$

and

$$\nabla^2 \boldsymbol{A} - \boldsymbol{\nabla} \cdot (\boldsymbol{\nabla} \cdot \boldsymbol{A}) = \frac{1}{c^2} \partial_t (\boldsymbol{\nabla}\phi) + \frac{1}{c^2} \frac{\partial^2 \boldsymbol{A}}{\partial t^2}. \tag{2.11}$$

Together, equations 2.5, 2.9, 2.10 and 2.11 form the Maxwell equations written in terms of the electromagnetic potentials $\boldsymbol{A}$ and ϕ. At first glance, this reformulation of Maxwell equations may seem unnecessary, especially if one takes into account that the quantities that are usually measured in experiments are the electric and magnetic fields $\boldsymbol{E}$ and $\boldsymbol{B}$. But, from the beginning of quantum mechanics in 1926, the usefulness of these potentials was clear as they were better suited to be introduced in the Schrödinger equation compared to the electric and magnetic fields $\boldsymbol{E}$ and $\boldsymbol{B}$ [66]. These quantities, especially the vector potential, were believed to be just mathematical artifacts with no relation to any physical quantity until the discovery of the Aharonov–Bohm effect, with no classical counterpart, evidenced the relation between the vector potential and the phase shift of the wave function [67]. Another feature that made physicists reluctant to use this formulation is the fact that the electromagnetic potentials are not uniquely defined. If a gauge transformation is applied on these potentials the corresponding fields remain unchanged.

2.1.2 Gauge Transformations

What equations 2.5 and 2.9 tell us is that the electric and magnetic fields can be defined through the derivatives of some potentials, this means that there is an *infinite* family of potentials which all lead to the same fields. This family of potentials are all connected through what is called a *gauge transformation*, whose most general form involves a scalar function $\Lambda(\boldsymbol{r}, t)$ applied in the following way:

$$\begin{aligned} \boldsymbol{A} &\to \boldsymbol{A}' = \boldsymbol{A} + \boldsymbol{\nabla}\Lambda \\ \phi &\to \phi' = \phi - \tfrac{\partial \Lambda}{\partial t}. \end{aligned} \tag{2.12}$$

The invariance of the electric and magnetic fields with respect to a gauge transformation of the corresponding electromagnetic potentials can be easily proved.

$$\begin{aligned} \boldsymbol{B}' &= \boldsymbol{\nabla} \times \boldsymbol{A}' = \boldsymbol{\nabla} \times (\boldsymbol{A} + \boldsymbol{\nabla}\Lambda) = \boldsymbol{\nabla} \times \boldsymbol{A} + \boldsymbol{\nabla} \times (\boldsymbol{\nabla}\Lambda) = \boldsymbol{\nabla} \times \boldsymbol{A} = \boldsymbol{B} \\ \boldsymbol{E}' &= -\boldsymbol{\nabla}\phi' - \partial_t \boldsymbol{A}' = -\boldsymbol{\nabla}\left(\phi - \partial_t \Lambda\right) - \partial_t(\boldsymbol{A} + \boldsymbol{\nabla}\Lambda) = -\nabla\phi - \partial_t \boldsymbol{A} = \boldsymbol{E} \end{aligned} \tag{2.13}$$

Although gauge symmetry was first noticed when dealing with classical electrodynamics it is now considered one of the fundamental symmetries of nature and has become a very powerful tool in many fields such as quantum mechanics, quantum field theory, and particle physics. In quantum mechanics, particularly, it can be easily proved the invariance of the Hamiltonian of a charged particle in an electromagnetic field under a gauge transformation, which only adds a global phase to the wavefunction thus conserving probability density and probability current.

Coulomb gauge

Because of the gauge freedom of the electromagnetic potentials, we can force them to fulfill certain conditions that help simplify calculations. When dealing with charged particles interacting with electromagnetic fields in a semi-classical fashion (like in our case), one particularly useful condition is the Coulomb gauge, also called transverse or radiation gauge. This condition reads as follows:

$$\boldsymbol{\nabla} \cdot \boldsymbol{A} = 0. \tag{2.14}$$

It is worth noting that the Coulomb gauge merely narrows down the *infinite* number of potentials compatible with a given electromagnetic field, it only selects a class of gauges. This means, as we will see later, that the Coulomb gauge admits further gauge fixing [68].

This gauge is particularly useful because it separates the instantaneous Coulomb interaction, which is responsible for the binding of close charges, from the interaction with the transverse radiation field [69]. When choosing the Coulomb gauge for radiation in the vacuum, in virtue of 2.10, we find that:

$$\nabla^2 \phi = 0 \tag{2.15}$$

which is the well known Laplace equation whose only regular solution is of the form:

$$\phi = 0. \tag{2.16}$$

This, in turn, implies that $\boldsymbol{E} = -\partial_t \boldsymbol{A}$. On the other hand, equation 2.11 turns into a homogeneous wave equation for the vector potential:

$$\nabla^2 \boldsymbol{A} - \frac{1}{c^2}\frac{\partial^2 \boldsymbol{A}}{\partial t^2} = 0. \tag{2.17}$$

The previous equation admits traveling waves of the form $\boldsymbol{A}(\omega t - \boldsymbol{k}\cdot\boldsymbol{r})$ as solutions, where ω is the angular frequency, $\boldsymbol{k}$ is the wave vector pointing in the propagation direction and $\boldsymbol{r}$ is the position vector. These solutions can then be expressed in terms of monochromatic plane waves like[1]:

$$\boldsymbol{A}(\boldsymbol{r}, t) = A_0\, e^{\pm i(\omega t - \boldsymbol{k}\cdot\boldsymbol{r} + \delta)}\boldsymbol{\epsilon}. \tag{2.18}$$

The alternative name of *transverse gauge* becomes now evident, the application of the Coulomb gauge implies that the interacting field must be expressed as a transverse wave where the propagation vector $\boldsymbol{k}$ and the polarization vector of the field $\boldsymbol{\epsilon}$ are orthogonal to each other, meaning $\boldsymbol{k}\cdot\boldsymbol{\epsilon} = 0$.

Velocity and length gauges

In atomic and molecular physics two other gauges that are widely used are the length and velocity gauges. These two gauges are compatible with the Coulomb gauge, meaning they pertain to the class of gauges that fulfill 2.14. The corresponding particle-radiation interaction Hamiltonians can be easily derived from classical electrodynamics and they are related to the interaction terms $\boldsymbol{p}\cdot\boldsymbol{A}$ (velocity) and $\boldsymbol{r}\cdot\boldsymbol{E}$ (length)[2]. The velocity gauge interaction term is obtained from the minimal coupling Hamiltonian, derived from Lagrangian mechanics, by replacing the canonical momentum with $\boldsymbol{p} \to \boldsymbol{p} - q\boldsymbol{A}$ and the energy by $E \to E + q\phi$. The length gauge, on the other hand, is related to the multipole expansion of the electromagnetic potential and can be interpreted through the simple picture of a dipole interacting with an external field [70].

As we have previously commented, quantum mechanics is formally gauge invariant. Otherwise, the evaluation of observables would lead to different results depending on the selected gauge. However, this invariance is only guaranteed for exact calculations. In practical calculations, non-physical parameters of the calculation might be gauge-dependent and convergence of the results in different gauges might not be possible. This fact is particularly important when considering one-center expansions, like the one used to calculate our field-free eigenstates, in the length or velocity gauge.

One thing to take into account when selecting a given gauge is that, during the calculation, widely varying variables should be avoided. In the length gauge, the canonical momentum corresponds exactly to the mechanical momentum of the bound electron driven by the electromagnetic field. On the other hand, in the velocity gauge, the canonical momentum can be interpreted as the mean mechanical momentum averaged over one cycle [71]. This fact results in the electron acquiring a larger value of momentum when using the length gauge. In virtue of $\boldsymbol{L} = \boldsymbol{r}\times\boldsymbol{p}$, higher

[1] From this point on we will adopt as convention that, when no coordinate dependence of the vector potential is explicitly shown, the full dependence on space and time coordinates will be assumed, $\boldsymbol{A} \equiv \boldsymbol{A}(\boldsymbol{r}, t)$.

[2] These expressions are derived in the context of a non-relativistic Hamiltonian in dipole approximation with classical fields.

values angular momentum are also achieved and a larger angular momentum expansion is needed in order to correctly represent the motion of the electron. For this reason, our choice of gauge to express the electromagnetic field in the study of photoionization in molecules is the velocity gauge. Nonetheless, we will derive expressions for the interaction Hamiltonian in both gauges for convergence testing purposes.

2.1.3 Spatial dependence of $\mathbf{A}(\mathbf{r}, t)$

The simultaneous dependence on space and time coordinates of the vector potential often poses a challenge when dealing with theoretical calculations in atoms and molecules. The usual approach is to expand the vector potential in a power series of $\boldsymbol{k} \cdot \boldsymbol{r}$:

$$\boldsymbol{A}(\omega t - \boldsymbol{k} \cdot \boldsymbol{r}) = \boldsymbol{A}(t) - \frac{1}{\omega}\frac{d\boldsymbol{A}(t)}{dt}\boldsymbol{k} \cdot \boldsymbol{r} + \frac{1}{2\omega^2}\frac{d^2\boldsymbol{A}(t)}{dt^2}(\boldsymbol{k} \cdot \boldsymbol{r})^2 + \mathcal{O}\left((\boldsymbol{k} \cdot \boldsymbol{r})^3\right) \tag{2.19}$$

For most calculations dealing with electromagnetic radiation up to the region of optical frequencies, taking only the zeroth-order term is widely regarded as a reasonable approximation. Mathematically, this holds as long as $|\boldsymbol{k} \cdot \boldsymbol{r}| \ll 1$ and, since $|\boldsymbol{k}| = 2\pi/\lambda$ with λ being the wavelength's radiation, when $\lambda \gg |\boldsymbol{r}|$ the series effectively converges to the lowest-order term. This approximation is called *long wave* or *dipole approximation* and it reflects the fact that, when the size of the atom or molecule is much smaller when compared to the wavelength of the radiation, the field can be viewed as spatially constant and homogeneous and only varying in time $\boldsymbol{A}(\boldsymbol{r}, t) \approx \boldsymbol{A}(t)$.

The implications of the dipole approximation are many. If we look at equation 2.5 it becomes clear that, within the dipole approximation, the magnetic field is always zero since $\boldsymbol{B} = \boldsymbol{\nabla} \times \boldsymbol{A}(t) = 0$. Another consequence of this approximation is the fact that the molecule does not *feel* any retardation effects arising from the finite speed of light. Since the field is only time-dependent, all points in space experience the same variations of the electromagnetic field at the same time effectively violating causality. Nevertheless, this approximation has proven to yield accurate results in a wide range of experimental conditions.

Inherent to all approximations is the existence of limits to its applicability, and the dipole approximation is no exception to this rule. For frequencies larger than those of UV, the breakdown of dipole approximation becomes evident as the size of the atom or molecule becomes comparable to the wavelength of radiation. But the rapid development of laser sources with increasing capabilities in delivering high-intensity beams has also shown limits to the applicability of the dipole approximation in the long-wave regime. Figure 2.1 depicts the regions were different approximations may be adopted as a function of intensity and field frequency.

The breakdown of dipole approximation in the long-wave region is associated with the use of high-intensity laser sources, which are able to ionize the electron by tunneling. For high enough intensities the laser can accelerate the electron to speeds that make it more susceptible to the magnetic field component of the Lorentz force, which scales as v/c. As a result of the combined effect of electric and magnetic fields, momentum is transferred in the direction of propagation of the field towards the electrons. The breakdown of the dipole approximation in the long-wave regime comes then from the impossibility to disregard magnetic effects [73]. This leads to the occurrence of non-dipole behavior such as magnetic displacement or radiation pressure [72]. The breakdown of the dipole approximation in the long-wave regime

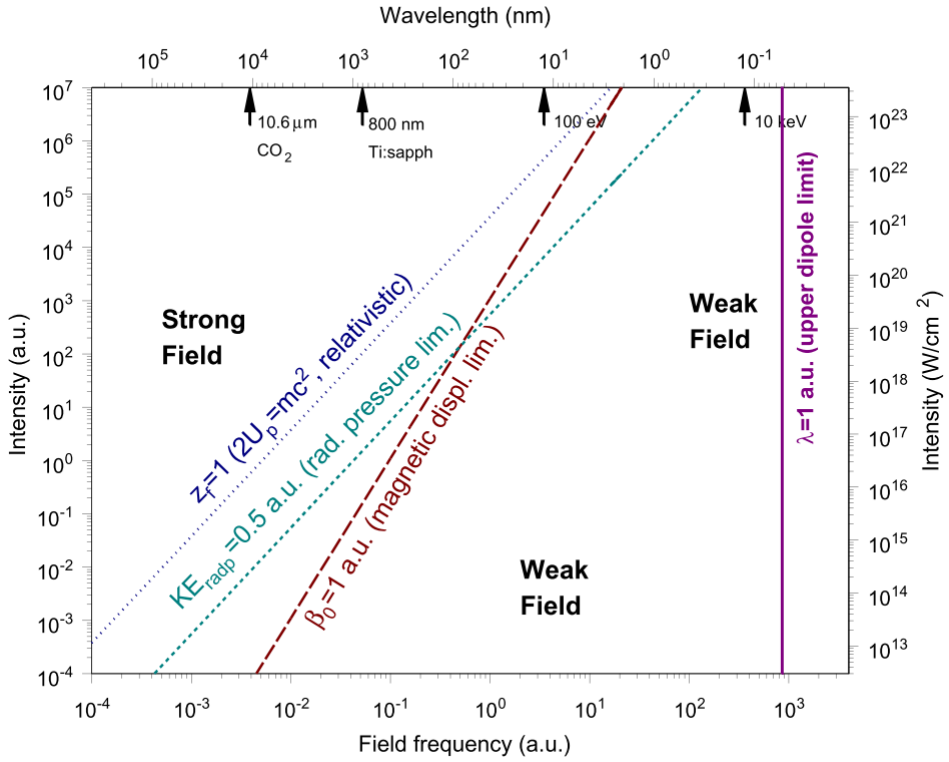

FIGURE 2.1 – Figure from Ref. [72] illustrating the different regions that appear in the wavelength-intensity parameter space. The *Weak Field* region corresponds to the situations in which the dipole approximation remains valid. In the short wavelength region, when the wavelength of radiation starts to be comparable to the size of the atom, we find the upper limit of the dipole approximation. In the long-wavelength region, we find the magnetic displacement limit, where the displacement in the field propagation direction caused by the magnetic field is comparable to the size of the atom, and the radiation pressure limit, with a non-negligible contribution to energy and momentum, as the first lower-limits for the applicability of the dipole approximation. The onset of relativistic effects begins outside the region of validity of the dipole approximation when $2U_p = mc^2$ where U_p is the ponderomotive energy of the electron.

can also be related to the size of the system with respect to the wavelength as in the short-wave case. The motion of the electron in a strong field can be approximated by that of a classical charged particle in an oscillating field with speed $v \equiv E/\omega$ and motion amplitude $r \equiv E/\omega^2$. For field intensities such that $\lambda \approx E/\omega^2$, the size of the system becomes comparable to the wavelength of the radiation and the dipole approximation is no longer valid.

Relativistic effects and non-dipole effects are also closely related. As can be seen in figure 2.1, the breakdown of the dipole approximation for long wavelengths marks the preamble to the inclusion of relativistic effects. As we have hinted before, by taking only the lowest-order term of the power expansion we are neglecting any relativistic effect caused by the finite speed of light. Higher-order terms of the vector potential expansion from 2.19 are intimately related to relativistic corrections. This is better illustrated if we adopt an alternative expression for the power series of the vector potential,

$$\boldsymbol{A}(\omega t - \boldsymbol{k}\cdot\boldsymbol{r}) = \boldsymbol{A}(t) - \frac{1}{c}\frac{d\boldsymbol{A}(t)}{dt}\boldsymbol{n}\cdot\boldsymbol{r} + \frac{1}{2}\frac{1}{c^2}\frac{d^2\boldsymbol{A}(t)}{dt^2}(\boldsymbol{n}\cdot\boldsymbol{r})^2 + \mathcal{O}\left(1/c^3\right). \tag{2.20}$$

The zeroth-order term, once again, results in the time-dependent vector potential characteristic of the dipole approximation. The rest of the terms are relativistic corrections that take into account to some extent the effects of the finite speed of light. In the description of the field-free molecule of Chapter 1, we did not consider any effect associated with the relativistic nature of particles, like Lorentz invariance light speed or spin effects, which are of the order $\mathcal{O}(1/c^2)$ in the Hamiltonian. To be consistent, in the study of non-dipole effects in photoionization of molecules in a non-relativistic regime, we will only keep terms of order $\mathcal{O}(1/c)$, which introduce retardation effects, and neglect all terms of order $\mathcal{O}(1/c^2)$, which are considered true relativistic effects in the field-free Hamiltonian [27].

2.2 The interaction Hamiltonian

In this section, we will derive the complete non-relativistic interaction Hamiltonian with the electromagnetic potentials expressed in the Coulomb and velocity (or length) gauges. We start from the minimal coupling Hamiltonian, derived from Lagrangian mechanics, which accounts for the interactions of charged particles with electromagnetic radiation [74,75]. The corresponding quantum interaction Hamiltonian for a particle with mass m and charge q is obtained by means of the usual canonical quantization procedure which takes the following form:

$$\begin{aligned}\mathcal{H} &= \frac{1}{2m}(p - q\boldsymbol{A})^2 + q\phi \\ &= \frac{1}{2m}(-\nabla^2 + iq\boldsymbol{\nabla}\cdot\boldsymbol{A} + iq\boldsymbol{A}\cdot\boldsymbol{\nabla} + (q\boldsymbol{A})^2) + q\phi.\end{aligned} \tag{2.21}$$

Coulomb gauge

The second step is to introduce the Coulomb gauge in our interaction Hamiltonian. Here we take advantage of the fact that $\boldsymbol{p}$ and $\boldsymbol{A}$ commute when the electromagnetic potentials are expressed in this gauge. This can be easily seen when considering the

action of $\boldsymbol{\nabla} \cdot \boldsymbol{A}$ on a wave function Φ and apply the chain rule to the action of the differential operator.

$$\boldsymbol{\nabla} \cdot \boldsymbol{A}\Phi \equiv \boldsymbol{\nabla}(\boldsymbol{A}\Phi) = (\boldsymbol{\nabla} \cdot \boldsymbol{A})\Phi + \boldsymbol{A}(\boldsymbol{\nabla}\Phi) = \boldsymbol{A}(\boldsymbol{\nabla}\Phi) \equiv \boldsymbol{A} \cdot \boldsymbol{\nabla}\Phi \tag{2.22}$$

We have taken advantage of the Coulomb gauge condition that mandates $\boldsymbol{\nabla} \cdot \boldsymbol{A} = 0$ to remove the first term of the sum[3]. We have also seen that, within the Coulomb gauge, $\phi = 0$. The interaction Hamiltonian in the Coulomb gauge is then expressed as:

$$\mathcal{H} = -\frac{1}{2m}\nabla^2 + \frac{iq}{m}\boldsymbol{A} \cdot \boldsymbol{\nabla} + \frac{q^2}{2m}\boldsymbol{A}^2. \tag{2.23}$$

This form of the total Hamiltonian tells us that there are two terms responsible for the interaction with the electromagnetic field. The term $\boldsymbol{A} \cdot \boldsymbol{P}$ is usually related to one-photon processes, whereas the $\boldsymbol{A}^2$ term is related to two-photon processes and plays no role in dipole approximation since it appears as a global phase of the wave function.

Multipolar expansion of $\mathbf{A}(\mathbf{r}, t)$

Since we are studying photoionization in a non-relativistic fashion we can take the multipolar expansion rejecting terms of order $\mathcal{O}(1/c^2)$ and higher. Introducing the truncated expansion of the vector potential in the Hamiltonian we have:

$$\begin{aligned}\mathcal{H} &= -\frac{1}{2m}\nabla^2 + \frac{iq}{m}\left(\boldsymbol{A}(t) + \boldsymbol{E}(t)\frac{\boldsymbol{n}\cdot\boldsymbol{r}}{c}\right)\cdot\boldsymbol{\nabla} + \frac{q^2}{2m}\left(\boldsymbol{A}(t) + \boldsymbol{E}(t)\frac{\boldsymbol{n}\cdot\boldsymbol{r}}{c}\right)^2 \\ &= -\frac{1}{2m}\nabla^2 + \frac{iq}{m}\boldsymbol{A}(t)\cdot\boldsymbol{\nabla} + \frac{q^2}{2m}\boldsymbol{A}^2(t) \\ &\qquad + \frac{iq}{mc}(\boldsymbol{n}\cdot\boldsymbol{r})\boldsymbol{E}(t)\cdot\boldsymbol{\nabla} + \frac{q^2}{mc}(\boldsymbol{n}\cdot\boldsymbol{r})\boldsymbol{A}(t)\cdot\boldsymbol{E}(t) + \mathcal{O}(1/c^2),\end{aligned} \tag{2.24}$$

where we have made use of of the fact that $\phi = 0$ in the Coulomb gauge, and that the electric field can be related to the vector potential by $\boldsymbol{E}(t) = -\partial_t \boldsymbol{A}(t)$ as shown in equation 2.9. The first three terms are equivalent to the interaction Hamiltonian in the dipole approximation, that is when $\boldsymbol{A}(\boldsymbol{r}, t) \approx \boldsymbol{A}(t)$. The next two are due to non-dipole effects, corresponding to corrections of order $\mathcal{O}(1/c)$, and are responsible for the introduction of retardation effects in the interaction Hamiltonian.

Velocity and length gauges

As we mentioned before, the velocity gauge is directly obtained from the minimal coupling Hamiltonian. To obtain the usual interaction Hamiltonian in the velocity gauge we perform the following unitary transformation like the one in equation 2.12:

$$\Lambda(\boldsymbol{r}, t) = \int_{-\infty}^{t'} -\frac{1}{2}\boldsymbol{A}^2(0, t)dt \tag{2.25}$$

[3]Note the difference between the two terms $\boldsymbol{\nabla} \cdot \boldsymbol{A}\Phi$ and $(\boldsymbol{\nabla} \cdot \boldsymbol{A})\Phi$. The first term implies that the operator $\boldsymbol{A}$ first acts on the state vector and then $\boldsymbol{\nabla}$ acts on the result. On the other hand, the second term corresponds to the operator $\boldsymbol{\nabla} \cdot \boldsymbol{A}$ acting on the state vector.

which results in the following expressions for the electromagnetic potentials

$$\begin{aligned} \boldsymbol{A} \to \boldsymbol{A}' &= \boldsymbol{A} + \boldsymbol{\nabla}\Lambda = \boldsymbol{A} + \boldsymbol{\nabla}\int_{-\infty}^{t'} -\frac{1}{2}\boldsymbol{A}^2(0,t)dt = \boldsymbol{A} \\ \phi \to \phi' &= \phi - \frac{\partial\Lambda}{\partial t} = 0 - \frac{\partial}{\partial t}\left(\int_{-\infty}^{t'} -\frac{1}{2}\boldsymbol{A}^2(0,t)dt\right) = \frac{1}{2}\boldsymbol{A}^2(t). \end{aligned} \tag{2.26}$$

It is easy to see that, by performing this gauge transformation, we eliminate the time-only dependent term of equation 2.24 in a way that does not alter the vector potential, thus remaining in the Coulomb gauge. This term does not allow transition between different states and the effect of the unitary transformation 2.25 on the final wave function is just the addition of a global phase. The final interaction Hamiltonian has the following form:

$$\mathcal{H} = -\frac{1}{2m}\nabla^2 + \frac{iq}{m}\boldsymbol{A}(t)\cdot\boldsymbol{\nabla} + \frac{iq}{mc}(\boldsymbol{n}\cdot\boldsymbol{r})\boldsymbol{E}(t)\cdot\boldsymbol{\nabla} + \frac{q^2}{mc}(\boldsymbol{n}\cdot\boldsymbol{r})\boldsymbol{A}(t)\cdot\boldsymbol{E}(t) \tag{2.27}$$

A useful partition of this Hamiltonian, whose convenience will become evident when we introduce the interaction picture in the next chapter, is the following:

$$\begin{aligned} \mathcal{H} &= \mathcal{H}_0 + \mathcal{V}_{DA}^{(1)} + \mathcal{V}_{RET}^{(1)} + \mathcal{V}_{RET}^{(2)} \\ \mathcal{H}_0 &= -\frac{1}{2m}\nabla^2 \\ \mathcal{V}_{DA}^{(1)} &= \frac{iq}{m}\boldsymbol{A}(t)\cdot\boldsymbol{\nabla} \\ \mathcal{V}_{RET}^{(1)} &= \frac{iq}{mc}(\boldsymbol{n}\cdot\boldsymbol{r})\boldsymbol{E}(t)\cdot\boldsymbol{\nabla} \\ \mathcal{V}_{RET}^{(2)} &= \frac{q^2}{mc}(\boldsymbol{n}\cdot\boldsymbol{r})\boldsymbol{A}(t)\cdot\boldsymbol{E}(t) \end{aligned} \tag{2.28}$$

The $\mathcal{H}_0$ term corresponds to the time-independent field-free Hamiltonian of the particle and the last three terms are time-dependent and represent the interaction with the electromagnetic field. The first one of these time-dependent terms, $\mathcal{V}_{DA}^{(1)}$, corresponds to the usual dipole approximation interaction term in the velocity gauge and is associated with $\boldsymbol{A}\cdot\boldsymbol{\nabla}$ from 2.23. The second term, $\mathcal{V}_{RET}^{(1)}$, is also derived from $\boldsymbol{A}\cdot\boldsymbol{\nabla}$ and constitutes its first non-dipole correction. The final term, $\mathcal{V}_{RET}^{(2)}$, is the first non-dipole correction to $\boldsymbol{A}^2$, which is neglected in dipole approximation, and plays a key role in the study of Stimulated Compton and Raman Scattering [76].

As mentioned before, because of the faster convergence of the angular momentum expansion while using the velocity gauge with respect to the length gauge, we will use the Hamiltonian shown in 2.28 for our calculations. However, it is worth obtaining also the final expression for the interaction Hamiltonian in the length gauge in dipole approximation. For this, we apply the the Goeppert-Mayer transformation to the Hamiltonian from 2.23. This gauge transformation is characterized by the function:

$$\Lambda(\boldsymbol{r},t) = -\boldsymbol{r}\cdot\boldsymbol{A}(t) \tag{2.29}$$

which results in the following electromagnetic potentials:

$$\begin{aligned} \boldsymbol{A} \to \boldsymbol{A}' &= \boldsymbol{A} + \boldsymbol{\nabla}\Lambda = \boldsymbol{A} - \boldsymbol{\nabla}\left(\boldsymbol{r}\cdot\boldsymbol{A}(t)\right) = 0 \\ \phi \to \phi' &= \phi - \frac{\partial\Lambda}{\partial t} = 0 + \frac{\partial}{\partial t}\left(\boldsymbol{r}\cdot\boldsymbol{A}(t)\right) = \boldsymbol{r}\cdot\boldsymbol{E}(t) \end{aligned} \tag{2.30}$$

For the expression of the vector potential we have made use of the formula for the gradient of the scalar product of two vectors:

$$\boldsymbol{\nabla}(\boldsymbol{r}\cdot\boldsymbol{A}(t)) = (\boldsymbol{A}(t)\cdot\boldsymbol{\nabla})\boldsymbol{r} + (\boldsymbol{r}\cdot\boldsymbol{\nabla})\boldsymbol{A}(t) + \boldsymbol{A}(t)\times(\boldsymbol{\nabla}\times\boldsymbol{r}) + \boldsymbol{r}\times(\boldsymbol{\nabla}\times\boldsymbol{A}(t))$$

where only the first survives given that all spatial derivatives of $\boldsymbol{A}(t)$ and $\boldsymbol{\nabla}\times\boldsymbol{r}$ are zero. Introducing the new gauge fixed potentials into the velocity gauge Hamiltonian, and neglecting all non-dipole terms, we have:

$$\mathcal{H} = -\frac{1}{2m}\nabla^2 + \boldsymbol{r}\cdot\boldsymbol{E}(t) \tag{2.31}$$

were we obtain the famous dipole term for the interaction $\boldsymbol{r}\cdot\boldsymbol{E}(t)$. The similarities between the dipole term in length gauge and the non-dipole term $\mathcal{V}^{(2)}_{RET}$ in velocity gauge, suggest a relation between the selection rules associated with both terms in velocity gauge. This issue will be further commented in the next chapter and when commenting on the results of our study on non-dipole effects.

2.2.1 The molecular Hamiltonian with radiation

In the previous section, we have developed the interaction Hamiltonian of a particle of mass m and charge q with electromagnetic radiation. The full Hamiltonian of interaction between electromagnetic radiation and the H_2 molecule may then be written by combining the field-free Hamiltonian, which incorporates all the interaction terms responsible for the internal motion of the molecule and is time-independent, and the interaction Hamiltonian defined in equation 2.28 acting on all the particles of the system. This Hamiltonian reads as follows.

$$\mathcal{H} = \mathcal{H}_{el} + T_N + V_e(\boldsymbol{r_1},\boldsymbol{r_2},t) + V_N(\boldsymbol{R}_A,\boldsymbol{R}_B,t) \tag{2.32}$$

where $\mathcal{H}_{el}$ and T_N where already defined in equation 1.4, and V_e and V_N are the interaction terms between radiation and the electrons and nuclei of the molecule respectively. These last terms, in turn, can be divided into several contributions associated with the different dipole and non-dipole terms developed in this chapter. The electronic and nuclear interaction potentials then read as:

$$\begin{aligned} V_e(\boldsymbol{r_1},\boldsymbol{r_2},t) &= \mathcal{V}^{(1)}_{DA} + \mathcal{V}^{(1)}_{RET} + \mathcal{V}^{(2)}_{RET} \\ V_N(\boldsymbol{R}_A,\boldsymbol{R}_B,t) &= \mathfrak{V}^{(1)}_{DA} + \mathfrak{V}^{(1)}_{RET} + \mathfrak{V}^{(2)}_{RET} \end{aligned} \tag{2.33}$$

where

$$\mathcal{V}^{(1)}_{DA} = -i\sum_i \boldsymbol{A}(t)\cdot\boldsymbol{\nabla}_{\boldsymbol{r}_i} \tag{2.34a}$$

$$\mathcal{V}^{(1)}_{RET} = -\frac{i}{c}\sum_i (\boldsymbol{n}\cdot\boldsymbol{r}_i)\,(\boldsymbol{E}(t)\cdot\boldsymbol{\nabla}_{\boldsymbol{r}_i}) \tag{2.34b}$$

$$\mathcal{V}^{(2)}_{RET} = \frac{1}{c}\sum_i (\boldsymbol{A}(t)\cdot\boldsymbol{E}(t))\,(\boldsymbol{n}\cdot\boldsymbol{r}_i). \tag{2.34c}$$

As we will detail in the next chapter, the term $V_N(\boldsymbol{R}_A,\boldsymbol{R}_B,t)$ can be neglected altogether in the basis of the photon energies considered in our study. The term $\mathcal{V}^{(1)}_{RET}$ can also be neglected since our study of non-dipole effects in photoionization focuses on

the phenomena of Stimulated Compton and Raman Scattering, in which this term plays a negligible role [77].

Chapter 3

Dynamical study of photoionization in H_2

3.1 Time dependent Schrödinger equation

In the study of photoionization of molecules by laser pulses, the evolution in time of a given quantum system, provided by its state, is described by the TDSE that is written:

$$i\frac{\partial}{\partial t}\left|\Psi(t)\right\rangle = \mathcal{H}(t)\left|\Psi(t)\right\rangle. \tag{3.1}$$

To solve the above equation, the total time-dependent Hamiltonian can be partitioned into a stationary field-free Hamiltonian and a time-dependent interaction potential as follows:

$$\mathcal{H}(t) = \mathcal{H}_0 + \mathcal{V}_{int}(t). \tag{3.2}$$

In this partition $\mathcal{H}_0$ represents the unperturbed Hamiltonian including all kinetic and potential terms of the field-free molecule which is, of course, time-independent. This Hamiltonian, and its corresponding eigenstates, were treated in detail in Chapter 1. The second term, $\mathcal{V}_{int}(t)$, represents the interaction of the system with the electromagnetic field. This interaction term was reviewed in detail in Chapter 2 where we showed that it can be further partitioned depending on the nature of the approximations we use to describe radiation-matter interaction.

In the first section of this chapter, we unveil the final form of the TDSE that we solve in our study of photoionization of H_2 with ultrashort laser pulses. This section synthesizes our knowledge on the field-free molecular eigenstates and interaction between matter and radiation together with the above partitioning of the total Hamiltonian.

3.1.1 Interaction picture

The insertion of the partitioned Hamiltonian shown in 3.2 into the TDSE allows us to introduce an alternative formulation of the dynamical evolution of our quantum system known as the interaction or Dirac picture. This formulation is fundamentally equivalent to the usual Schrödinger and Heisenberg pictures and is particularly convenient in the study of collisions and in the context of TDPT. This is because it removes the "trivial" time evolution of the quantum states once the interaction potential $\mathcal{V}_{int}(t)$ is off. When there is no interaction with the laser ($\mathcal{V}_{int}(t) = 0$) the problem reduces to finding the set of eigenstates that diagonalize $\mathcal{H}_0$ by solving:

$$\mathcal{H}_0\left|\psi_n\right\rangle = E_n\left|\psi_n\right\rangle, \tag{3.3}$$

and propagate them using the field-free time evolution operator $U_0(t) = e^{-i\mathcal{H}_0 t}$ as:

$$|\phi_n(t)\rangle = U(t)\,|\psi_n\rangle = |\psi_n\rangle\, e^{-iE_n t}. \tag{3.4}$$

Without any loss of generality, we can use this set of eigenstates as complete basis that is used to expand any solution of 3.1 as:

$$|\Psi(t)\rangle = \sum_n c_n(t)\,|\phi_n(t)\rangle = \sum_n c_n(t)\,|\psi_n\rangle\, e^{-iE_n t}. \tag{3.5}$$

Solving a differential equation by expanding its solutions in a basis set is the foundation of spectral method techniques. By using the eigenstates of the molecule as basis set we can encapsulate the time-dependence associated to the field-free evolution of the system in the exponential $e^{-iE_n t}$. This way, the time evolution resulting from the interaction with the laser must come exclusively from the time-dependent coefficients of the expansion. We thus define the time-dependent state vectors and the interaction potential operator in the interaction picture, from their corresponding forms in the Schrödinger picture, as:

$$\begin{aligned} |\Psi_I(t)\rangle &= e^{i\mathcal{H}_0 t}\,|\Psi(t)\rangle = \sum_n c_n(t)\,|\psi_n\rangle \\ V_I(t) &= e^{i\mathcal{H}_0 t}\mathcal{V}_{int}(t)e^{-i\mathcal{H}_0 t}. \end{aligned} \tag{3.6}$$

From these definitions the resulting TDSE in the interaction picture becomes:

$$i\frac{\partial}{\partial t}\,|\Psi_I(t)\rangle = V_I(t)\,|\Psi_I(t)\rangle\,. \tag{3.7}$$

This formulation lies in-between the Schrödinger and Heisenberg pictures since, as reflected by equations 3.6, both states and operators evolve in time. The advantage of the interaction picture is that it separates the time evolution resulting from the interaction potential so that it only affects the state vectors. On the other hand, the time evolution of the operators originates from purely kinematic effects associated with the unperturbed Hamiltonian.

Taking equation 3.7 and projecting it onto $\langle\psi_m|$ we obtain the following first order coupled differential equation:

$$i\frac{\mathrm{d}c_m(t)}{\mathrm{d}t} = \sum_n c_n(t)\,\langle\psi_m|\,V_I(t)\,|\psi_n\rangle = \sum_n c_n(t)\,\langle\psi_m|\,\mathcal{V}_{int}(t)\,|\psi_n\rangle\, e^{i(E_m-E_n)t} \tag{3.8}$$

where we have made use of the expansion of the state vector from 3.6. This equation can also be expressed in matrix form as:

$$i\frac{d}{dt}\begin{pmatrix} c_1(t) \\ c_2(t) \\ \vdots \\ c_n(t) \end{pmatrix} = \begin{pmatrix} V_{11}(t) & V_{12}(t) & \cdots & V_{1n}(t) \\ V_{21}(t) & V_{22}(t) & \cdots & V_{2n}(t) \\ \vdots & \vdots & \ddots & \vdots \\ V_{n1}(t) & V_{n2}(t) & \cdots & V_{nn}(t) \end{pmatrix} \cdot \begin{pmatrix} c_1(t) \\ c_2(t) \\ \vdots \\ c_n(t) \end{pmatrix}, \tag{3.9}$$

with the interaction matrix elements

$$V_{nm}(t) = \langle\psi_n\,|V_I(t)|\,\psi_m\rangle = \langle\psi_n|\,\mathcal{V}_{int}(t)\,|\psi_m\rangle\, e^{i(E_n-E_m)t}. \tag{3.10}$$

3.1.2 Time-dependent Feshbach close-coupling method

Up until now, we have alluded, in a very general way, to a complete basis of eigenstates in which to expand the total time-dependent wave function. The final form of the TDSE shown in 3.9 will depend to a large degree on the specific characteristics of this basis set. In this section, we will introduce in our spectral approach to solve the TDSE all the tools developed in Chapter 1 regarding the eigenstates of H_2, which conform to our particular basis set.

First, we recall the partition of the total wave function into resonant and non-resonant parts by means of the Feshbach projectors, seen in equation 1.27, and apply it to the time-dependent case:

$$|\Psi(t)\rangle = \mathcal{Q}\,|\Psi(t)\rangle + \mathcal{P}\,|\Psi(t)\rangle\,. \tag{3.11}$$

This modification of the original stationary Feshbach formalism is needed if one wants to study molecular autoionization and photionization as a function of time. By inserting this *ansatz* into the TDSE and projecting onto each subspace we obtain the following pair of coupled differential equations:

$$i\frac{\partial}{\partial t}\begin{pmatrix} \mathcal{Q}\,|\Psi(t)\rangle \\ \mathcal{P}\,|\Psi(t)\rangle \end{pmatrix} = \begin{pmatrix} \mathcal{Q}\mathcal{H}\mathcal{Q} & \mathcal{Q}\mathcal{H}\mathcal{P} \\ \mathcal{P}\mathcal{H}\mathcal{Q} & \mathcal{P}\mathcal{H}\mathcal{P} \end{pmatrix}\begin{pmatrix} \mathcal{Q}\,|\Psi(t)\rangle \\ \mathcal{P}\,|\Psi(t)\rangle \end{pmatrix}. \tag{3.12}$$

At the beginning of section 1.4, the validity of the BO approximation within the resonant and non-resonant subspaces was stated. This was supported under the assumption that non-adiabatic effects are negligible across each subspace. The question now is if non-adiabatic effects can be neglected when there is population transfer between the $\mathcal{Q}$ and $\mathcal{P}$ subspaces, *i.e.* autoionization, caused by the crossed terms $\mathcal{Q}\mathcal{H}\mathcal{P}$ and $\mathcal{P}\mathcal{H}\mathcal{Q}$. For that, we make use of the fact that autoionization lifetimes of doubly excites states are almost entirely due to electron correlation. We then can assume that $\mathcal{Q}T_N(R)\mathcal{P} = \mathcal{P}T_N(R)\mathcal{Q} = 0$, which implies that both projector operators commute with the nuclear kinetic energy operator $[T_N(R), \mathcal{Q}] = [T_N(R), \mathcal{P}] = 0$. This means that we can use a basis set of BO vibronic states written as products of electronic and nuclear wave functions $\{\psi_n(\boldsymbol{r}; R)\cdot\chi_{v_n}(R)\}$ to approximate our total time-dependent wave function.

Another consequence of the commutation between both $\mathcal{P}$ and $\mathcal{Q}$ with the nuclear kinetic energy operator $T_N(R)$ is the need to redefine the stationary Hamiltonian from 3.2. The reason being the occurrence of the autoionization term $\mathcal{Q}\mathcal{H}_{el}\mathcal{P}$ (and its hermitian conjugate $\mathcal{P}\mathcal{H}_{el}\mathcal{Q}$) which represents a time-independent non-stationary operator. We can define the total molecular Hamiltonian as the sum of a new Feshbach unperturbed block-diagonal Hamiltonian plus a new interaction potential as:

$$\begin{aligned} \mathcal{H}_0 \to \mathcal{H}_0^{Fesh} &= \mathcal{Q}\mathcal{H}_0\mathcal{Q} \oplus \mathcal{P}\mathcal{H}_0\mathcal{P} \\ \mathcal{V}_{int}(t) \to \mathcal{V}_{int}^{Fesh}(t) &= \mathcal{V}_{int}(t) + \mathcal{Q}\mathcal{H}_{el}\mathcal{P} + \mathcal{P}\mathcal{H}_{el}\mathcal{Q}. \end{aligned} \tag{3.13}$$

The new form of the unperturbed Hamiltonian allows us to expand the total time-dependent wave function in a basis set of vibronic states belonging to the $\mathcal{P}$ and $\mathcal{Q}$

subspaces. Its final form in the Schrödinger picture is:

$$\begin{aligned}\langle \mathbf{r}, R|\Psi(t)\rangle \equiv \Psi(\mathbf{r},R,t) = &\sum_b \sum\!\!\!\!\!\!\int_{v_b} C_{bv_b}(t)\psi_b(\mathbf{r};R)\chi_{v_b}(R)e^{-iW_{bv_b}t} \\ &+ \sum_r \sum\!\!\!\!\!\!\int_{v_r} C_{rv_r}(t)\psi_r(\mathbf{r};R)\chi_{v_r}(R)e^{-iW_{rv_r}t} \\ &+ \sum_{\alpha\ell_\alpha}\int d\varepsilon_\alpha \sum\!\!\!\!\!\!\int_{v_\alpha} C^{\ell_\alpha\varepsilon_\alpha}_{\alpha v_\alpha}(t)\psi^{\varepsilon_\alpha}_{\alpha\ell_\alpha}(\mathbf{r};R)\chi_{v_\alpha}(R)e^{-iW_{\alpha v_\alpha}t},\end{aligned} \tag{3.14}$$

where $\sum\!\!\!\!\!\!\int_v$ means a summation over discrete vibrational bound states and an integration over dissociative states of the nuclear continuum. The three different terms of the expansion correspond to the different types of eigenstates of the molecular field-free Hamiltonian which can be summarized as follows:

1. Vibronic **bound states** $\{\psi_b(\mathbf{r};R)\cdot\chi_{v_b}(R)\}$. These states represent the molecule being in the bth electronic bound state and in the vibrational state v_b associated to the bth bound potential energy curve with total vibronic energy W_{bv_b}. Although $\psi_b(\mathbf{r};R)$ formally belongs to the $\mathcal{P}$ subspace, in practice they are obtained from a direct diagonalization of 1.22 using a CI scheme as described in section 1.3.

2. Vibronic **autoionizing or doubly excited states** (resonances in the continuum) $\{\psi_r(\mathbf{r};R)\cdot\chi_{v_r}(R)\}$. These states represent the molecule being in the rth resonant state and in the vibrational state v_r associated to the rth resonant potential energy curve with total vibronic energy W_{rv_r}. They belong to the $\mathcal{Q}$ subspace and are obtained by diagonalization of $\mathcal{Q}\mathcal{H}_{el}\mathcal{Q}$ as shown in section 1.4.2.

3. Vibronic **non-resonant continuum states** $\{\psi^{\varepsilon_\alpha}_{\alpha l_\alpha}(\mathbf{r};R)\cdot\chi_{v_\alpha}(R)\}$. These states represent scattering states characterized by an electron with kinetic energy ε_α and angular momentum ℓ_α, and an ion in its αth electronic state (the αth ionization threshold of the molecule) and in the vibrational state v_α associated to the αth ionic potential energy curve. The total vibronic energy of the molecule is $W_{\alpha v_\alpha} = \varepsilon_\alpha + E_{v_\alpha}$ where E_{v_α} is the vibronic energy of the remaining ion. These states are approximate solutions of the $\mathcal{P}\mathcal{H}_{el}\mathcal{P}$ eigensystem and are calculated within the framework of multichannel scattering theory using a close-coupling expansion as detailed in section 1.4.1.

Introducing the previous *ansatz* into the TDSE in the interaction picture, together with the Feshbach interaction potential from equation 3.13, we obtain the set of coupled differential equations which, in compact matrix form, read as:

$$i\frac{d}{dt}\begin{pmatrix} C_b \\ C_r \\ C_c \end{pmatrix} = \begin{pmatrix} V_{bb'}(t) & V_{br}(t) & V_{bc}(t) \\ V_{rb}(t) & V_{rr'}(t) & [V(t)+\mathcal{Q}\mathcal{H}_{el}\mathcal{P}]_{rc} \\ V_{cb}(t) & [V(t)+\mathcal{P}\mathcal{H}_{el}\mathcal{Q}]_{cr} & V_{cc'}(t) \end{pmatrix}\cdot\begin{pmatrix} C_b \\ C_r \\ C_c \end{pmatrix} \tag{3.15}$$

where we have used the compact notation $b=\{bv_b\}, r=\{rv_r\}$ and $c=\{\alpha v_\alpha \ell_\alpha \varepsilon_\alpha\}$. Analogously to the matrix elements of 3.10, we define the new matrix elements in a

basis of vibronic states as[1]:

$$\begin{aligned} V_{nm}(t) &= \int_0^{R_{max}} \chi_{v_n}(R) \left\langle \psi_n(\boldsymbol{r};R) \left| V_I(\boldsymbol{r},R,t) \right| \psi_m(\boldsymbol{r};R) \right\rangle \chi_{v_m}(R) dR \\ \mathcal{Q}\mathcal{H}_{el}\mathcal{P}_{nm} &= \int_0^{R_{max}} \chi_{v_n}(R) \left\langle \psi_n(\boldsymbol{r};R) \left| \mathcal{Q}\mathcal{H}_{el}\mathcal{P}_I \right| \psi_m(\boldsymbol{r};R) \right\rangle \chi_{v_m}(R) dR \end{aligned} \tag{3.16}$$

For the sake of conciseness we have adopted the compact notation $\boldsymbol{r} \equiv (\boldsymbol{r}_1, \boldsymbol{r}_2)$. This matrix equation represents the final result of our implementation for the solution of TDSE in the context of molecular photoionization, the *time-dependent Feshbach close coupling* (TDFCC) method.

One of the advantages of our method is the straightforward interpretation of autoionization in time that it allows. While the interaction potential $V(t)$ populates both $\mathcal{P}$ and $\mathcal{Q}$ subspaces in time, the crossed terms $\mathcal{Q}\mathcal{H}_{el}\mathcal{P}$ and $\mathcal{P}\mathcal{H}_{el}\mathcal{Q}$ are responsible for the population transfer between the two subspaces. In practice, the role of these crossed terms is to induce doubly excited states to decay into the non-resonant continuum depleting the $\mathcal{Q}$ subspace. As mentioned before, this term is non-stationary but time-independent, meaning that it is active before and after the interaction when the laser is on. For atoms, the action of this term when $t \to \infty$ completely empties the $\mathcal{Q}$ subspace.

$$\lim_{t\to\infty} \mathcal{P} \left|\Psi(t)\right\rangle = \left|\Psi(t)\right\rangle \qquad \lim_{t\to\infty} \mathcal{Q} \left|\Psi(t)\right\rangle = 0 \tag{3.17}$$

In molecules, especially ones with light nuclei like H_2, this is no longer true. Since dissociation competes in time with autoionization, resonant states can dissociate before they have had time to autoionize. Some of the norm of the total wave function may remain then in the $\mathcal{Q}$ subspace, so the asymptotic limit needs to be redefined as:

$$\lim_{t\to\infty} \mathcal{P} \left|\Psi(t)\right\rangle = \Phi_{\text{ion}} \qquad \lim_{t\to\infty} \mathcal{Q} \left|\Psi(t)\right\rangle = \Phi_{\text{diss}} \tag{3.18}$$

where Φ_{ion} is the asymptotic representation of the ionization channels and Φ_{diss} is the asymptotic representation of the dissociative channels that form neutral fragments. If a doubly excited state dissociates before being able to autoionize population transfer mediated by $\mathcal{Q}\mathcal{H}_{el}\mathcal{P}$ is no longer possible so, effectively, this term asymptotically tends to zero. The limit of the unperturbed Hamiltonian becomes

$$\lim_{t\to\infty} \mathcal{H}_0 = \mathcal{Q}\mathcal{H}_0\mathcal{Q} + \mathcal{P}\mathcal{H}_0\mathcal{P}, \tag{3.19}$$

so that, when $t \to \infty$, the eigenstates of the $\mathcal{P}$ and $\mathcal{Q}$ subspaces are also eigenstates of the total unperturbed Hamiltonian. This is another powerful consequence of the TDFCC method, the coefficients $C_{\alpha v_\alpha}^{\ell_\alpha \varepsilon_\alpha}$ of our expansion truly represent physical ionization amplitudes in the asymptotic limit. Calculation of photoelectron spectra (PES) and molecular angular distributions becomes straightforward by just taking the expansion coefficients at $t = \infty$.

3.2 Time dependent perturbation theory

Alternatively to the resolution of the TDSE, the use of perturbation theory, especially its time dependent version, is also very extended in the study of photoionization in molecules as it does not require solving a system of coupled differential equations.

[1] Equivalently for $\mathcal{P}\mathcal{H}_{el}\mathcal{Q}$.

It also presents many advantages from the interpretation point of view, especially when dealing with multiphoton processes.

Mathematically, the study of the dynamic evolution of a quantum system reduces to the determination of the time evolution operator $U(t, t_0)$. This unitary operator, completely determined by the Hamiltonian of a system, creates a correspondence between the state vector of a system at a time t_0 and its state at a later time t as

$$U(t, t_0)|\Psi(t_0)\rangle = |\Psi(t)\rangle. \tag{3.20}$$

The probability to find a system, initially prepared as $\Psi(t_0) \equiv \psi_i$, in a given state ψ_f at a later time t can then be calculated as:

$$P_{i\to f}(t) = \left|\langle\psi_f|\Psi(t)\rangle\right|^2 = \left|\langle\psi_f\left|U\left(t, t_0\right)\right|\psi_i\rangle\right|^2. \tag{3.21}$$

If the initial and final states are eigenstates of the Hamiltonian of the system, calculation of transition probabilities reduces to the problem of finding the matrix elements of the time evolution operator.

The problem of finding the time evolution operator associated to a time dependent Hamiltonian is by no means trivial and, in general, one needs to solve the time-dependent Schrödinger equation to obtain it. When considering a system whose Hamiltonian can be partitioned, as shown in equation 3.2, into a stationary part with well known solutions and a time-dependent perturbation, approximate solutions can be obtained with the use of time-dependent perturbation theory (TDPT). From the representation of the TDSE in the interaction picture shown in equation 3.7 it is easy to see that, integrating, we get:

$$|\Psi_I(t)\rangle = |\Psi_I(t_0)\rangle - i\int_{t_0}^{t} dt_1 V_I(t_1)|\Psi_I(t_1)\rangle. \tag{3.22}$$

Substituting $\Psi_I(t)$ into 3.20 and projecting on both sides with $\Psi_I(t_0)$ we obtain the following integral equation for the evolution operator in the interaction picture:

$$U_{\mathrm{I}}\left(t, t_0\right) = 1 - i\int_{t_0}^{t} V_{\mathrm{I}}\left(t_1\right) U_{\mathrm{I}}\left(t_1, t_0\right) \mathrm{d}t_1. \tag{3.23}$$

Through an iterative process the previous equation transforms into the well known Dyson series:

$$U_I(t, t_0) = 1 + \sum_{N=1}^{\infty} U_I^{(N)}(t, t_0) \tag{3.24}$$

where the different terms of the series are defined as

$$\begin{aligned}
U_I^{(1)}\left(t, t_0\right) &= -i\int_{t_0}^{t} dt_1 V_I\left(t_1\right) \\
U_I^{(2)}\left(t, t_0\right) &= (-i)^2\int_{t_0}^{t} dt_1 V_I\left(t_1\right)\int_{t_0}^{t_1} dt_2 V_I\left(t_2\right) \\
U_I^{(N)}\left(t, t_0\right) &= (-i)^N\int_{t_0}^{t} dt_1 V_I\left(t_1\right)\int_{t_0}^{t_1} dt_2 V_I\left(t_2\right)\cdots\int_{t_0}^{t_{N-1}} dt_N V_I\left(t_N\right).
\end{aligned} \tag{3.25}$$

If the interaction term V_I represents a weak disturbance to the system, the series can be truncated to a finite order assuming that it converges. Each term of the Dyson series can be related to a Feynman diagram and the order of each term can be understood as the number of times the system interacts with the potential V_I.

Introducing the Dyson series into the expression for the transition matrix element shown in equation 3.22 we obtain

$$\langle \psi_f | U(t,t_0) | \psi_i \rangle = \delta_{fi} + \sum_{N=1}^{\infty} \langle \psi_f | U_I^{(N)}(t,t_0) | \psi_i \rangle. \tag{3.26}$$

The first and second order corrections of this series then read as

$$\langle \psi_f | U_I^{(1)}(t,t_0) | \psi_i \rangle = -i \int_{t_0}^{t} dt_1 \langle \psi_f | V_I(t_1) | \psi_i \rangle \tag{3.27a}$$

$$\langle \psi_f | U_I^{(2)}(t,t_0) | \psi_i \rangle = (-i)^2 \sum\!\!\!\!\!\!\int_m \int_{t_0}^{t} dt_1 \langle \psi_f | V_I(t_1) | \psi_m \rangle \times \int_{t_0}^{t_1} dt_2 \langle \psi_m | V_I(t_2) | \psi_i \rangle \tag{3.27b}$$

where, for the expression of the second-order matrix element, we have made used of the closure relation:

$$\mathbf{1} = \sum\!\!\!\!\!\!\int_m |\psi_m\rangle \langle \psi_m| . \tag{3.28}$$

For a given transition, the order of the truncated Dyson series and the power of the field involved in the interaction are directly related to the number of photons participating in the process. For direct transitions between states, *i.e.* first order transition, the interaction terms $\boldsymbol{A}\cdot\boldsymbol{P}$ and $\boldsymbol{A}^2$ are linked to processes involving one and two photons, respectively, as we advanced in Chapter 2. For $\boldsymbol{A}^2$, since the transition is not mediated by any intermediate state, the interaction with the two photons is simultaneous. This has important consequences on the study of non-dipole effects as we will see in Part III. In higher order transitions, a sequence of coherent time-ordered events is established for the interaction with multiple photons. If we consider, for example, a second-order matrix element where the interaction term is $\boldsymbol{A}\cdot\boldsymbol{P}$, it can be shown that it corresponds to a sequential two-photon process. Looking at equation 3.27b we see that the system interacts two times with the interaction potential at t_1 and t_2 such that $t_0 \leq t_2 \leq t_1 \leq t$. At t_2 a photon associated to $\boldsymbol{A}\cdot\boldsymbol{P}$ induces a transition from the initial state ψ_i to an intermediate virtual state ψ_m. Then, at t_1 the system interacts again with the potential and a second photon mediates the transition from ψ_m to the final state ψ_f. It is worth mentioning that, although we call this kind of process sequential, both interactions in a second-order transition are coherent in time.

It is easy to generalize this case to conclude that a given matrix element of order N with interaction term $\boldsymbol{A}\cdot\boldsymbol{P}$ can be linked to a sequential N-photon process through $N-1$ intermediate virtual states. This result, extended for long enough interaction times, is the basis for the derivation of the well-known Fermi's golden rule. Similar reasoning for the interaction term $\boldsymbol{A}^2$ links matrix elements of order N with N sequential processes where each event implies the simultaneous interaction with two photons. Globally, $2N$ photons participate in an N-order process involving $\boldsymbol{A}^2$. It must be stressed that this multiphoton interpretation holds as long as one remains in a perturbative regime. An example of this is strong filed ionization where perturbation theory fails and an interpretation in terms of quantum tunneling is better suited.

Unlike with probabilities obtained from the resolution of 3.15, which account for all N-order processes, specific expressions must be derived for each process that one wants to study in the context of TDPT. This will be done in Chapter 5 related

to the study of Stimulated Raman Scattering and Stimulated Compton Scattering processes. Nonetheless, the multiphoton interpretation of TDPT is already a very powerful tool by itself which can be used in the analysis of results obtained from non-perturbative calculations. From the selection rules associated with the interaction operator and symmetry considerations, one can obtain the order of a given transition.

3.3 Matrix elements

One key element in our study of photoinization of molecules with ultashort laser pulses is the calculation of matrix elements of the form:

$$V_{nm}(t) = \langle \psi_m | V_I(t) | \psi_n \rangle \tag{3.29}$$

This terms represent the coupling between states through the interaction potential and, as can be seen in equations 3.15 and 3.27, they are needed for both perturbative and non-perturbative calculations. In this section we will address some properties concerning these matrix elements, as well as those associated with the operator $\mathcal{Q}\mathcal{H}_{el}\mathcal{P}$.

From the computational point of view, calculation of couplings between electronic states is usually the most expensive task, primarily due to the necessity to use large angular and radial basis sets supported in boxes of considerable size. This is needed in order to correctly describe the high oscillatory behavior of continuum states and to avoid unphysical reflections of the ionized electron at the edges of the box. If we consider matrix elements on a basis of vibronic states, which is mandatory in the study of coupled electron-nuclear dynamics, the calculation of the aforementioned couplings has to be repeated at each internuclear distance of our nuclear coordinate space. Even in the context of FNA, if one is interested in above-threshold ionization processes, computation time scales rapidly with the electronic grid dimension.

One of the main advantages of our method is that these heavy calculations need to be performed just once, instead of at every time step of propagation. This is not surprising for the case of $\mathcal{Q}\mathcal{H}_{el}\mathcal{P}$ since it is a time-independent operator. For the case of the time-dependent interaction potential it can be shown that, for interaction potentials like the ones discussed in Chapter 2, the time-dependent part containing the information on the laser parameters can be factored out. This allows us to use the same matrix elements having only to invest computer effort in propagating the dynamics for each specific laser field configuration.

The calculation of the vibronic couplings shown 2.32 can be further simplified if we neglect the effect of the interaction potential with nuclear coordinates. This is justified in the basis of the validity of the BO approximation. Separating the interaction potential into one part acting on the electrons and another acting on the nuclei,

as shown in 2.32, the matrix elements are written:

$$\begin{aligned} V_{nm}(t) &= \int_0^{R_{\max}} \mathrm{d}R \chi_{\nu_n}(R) \cdot \langle \psi_n(\mathbf{r};R) \left| V(\boldsymbol{r},R;t) \right| \psi_m(\mathbf{r};R) \rangle \cdot \chi_{\nu_m}(R) \\ &= \int_0^{R_{\max}} \mathrm{d}R \chi_{\nu_n}(R) \cdot \langle \psi_n(\mathbf{r};R) \left| V_e(\boldsymbol{r};t) + V_N(R;t) \right| \psi_m(\mathbf{r};R) \rangle \cdot \chi_{\nu_m}(R) \\ &= \int_0^{R_{\max}} \mathrm{d}R \chi_{\nu_n}(R) \cdot \langle \psi_n(\mathbf{r};R) \left| V_e(\boldsymbol{r};t) \right| \psi_m(\mathbf{r};R) \rangle \cdot \chi_{\nu_m}(R) \\ &\quad + \int_0^{R_{\max}} \mathrm{d}R \chi_{\nu_n}(R) \cdot V_N(R;t) \cdot \chi_{\nu_m}(R) \cdot \langle \psi_n(\mathbf{r};R) | \psi_m(\mathbf{r};R) \rangle \end{aligned}$$

The second term of this expression is zero unless for transitions which do not change the electronic state. The part of the interaction potential affecting the nuclear coordinates is then solely responsible for vibrational transitions in the same electronic potential energy curve. This kind of transitions involve photon energies in the IR region of the spectrum, which can be neglected in our case given our interest in phenomena associated with the interaction with UV and X-ray photons. The calculation of vibronic couplings then reduces to the integration over nuclear coordinates of the initial and final nuclear wave functions with the matrix elements between electronic states of the form:

$$\left\langle \psi_n(\mathbf{r};R) \middle| V_e(\boldsymbol{r};t) \middle| \psi_m(\mathbf{r};R) \right\rangle. \tag{3.30}$$

An analogous result is found for the expression of the vibronic matrix elements of $\mathcal{Q}\mathcal{H}_{el}\mathcal{P}$ derived from the commutation between the nuclear kinetic energy operator and the Feshbach projectors $\mathcal{P}$ and $\mathcal{Q}$.

3.3.1 Selection rules

As shown in 2.33, $V_e(\boldsymbol{r};t)$ can be separated into a dipole and a non-dipole contribution associated to the operators $\boldsymbol{A}\cdot\boldsymbol{P}$ and $\boldsymbol{A}^2$ respectively. These contributions, represented by the interaction operators $\mathcal{V}_{DA}^{(1)}$ and $\mathcal{V}_{RET}^{(2)}$, are shown in equation 2.34. The corresponding matrix elements representing the coupling between electronic states through these operators are expressed as follows:

$$V_{nm}^{(A\cdot P)}(t) = -iA(t) \langle \psi_n(\mathbf{r};R) \left| \epsilon \cdot \boldsymbol{\nabla} \right| \psi_m(\mathbf{r};R) \rangle \, e^{i(E_n - E_m)t} \tag{3.31a}$$

$$V_{nm}^{(A^2)}(t) = \boldsymbol{A}(t)\cdot\boldsymbol{E}(t)\alpha \langle \psi_n(\mathbf{r};R) \left| \boldsymbol{n}\cdot\boldsymbol{r} \right| \psi_m(\mathbf{r};R) \rangle \, e^{i(E_n - E_m)t}, \tag{3.31b}$$

where we have made use of the fact that the time-only dependent functions $\boldsymbol{A}(t)$ and $\boldsymbol{E}(t)$, recalling that $\boldsymbol{E}(t) = -\partial_t \boldsymbol{A}(t)$, can be factored out. We thus remain with the calculation of the time-independent matrix elements involving the position and momentum operators. Calculation of these operators in a cartesian basis is an arduous task, specially considering that our electronic wave functions are expressed in a basis of spherical harmonics. For this reason, we switch to a representation of these operators in spherical components which relate to the original cartesian operators as:

$$\begin{aligned} r_1^{(1)} &= -\frac{1}{\sqrt{2}}(x+iy) & \nabla_1^{(1)} &= -\frac{1}{\sqrt{2}}(\nabla_x + i\nabla_y) \\ r_{-1}^{(1)} &= \frac{1}{\sqrt{2}}(x-iy) & \nabla_{-1}^{(1)} &= \frac{1}{\sqrt{2}}(\nabla_x - i\nabla_y) \\ r_0^{(1)} &= z & \nabla_0^{(1)} &= \nabla_z \end{aligned} \tag{3.32}$$

With this transformation the cartesian operators turn into spherical tensors operators of rank one, which have rotational properties closely related to those of angular momentum eigenstates and enable us to use the Wigner-Eckart theorem. This theorem makes it easier to calculate the matrix elements of spherical tensor operators in the basis of angular momentum eigenstates by expressing them as the product between two factors. One of the factors corresponds to a $3j$-symbol containing all the information on the angular momentum orientation of each state and of the spherical tensor operator, and the other independent of it. For the matrix elements of the position and momentum operator in spherical components this theorem reads results in the following expression.

$$\left\langle U_{n\ell}\mathcal{Y}_{\ell}^{m}\middle|\nabla_{\mu}^{(1)}\middle|U_{n'\ell'}\mathcal{Y}_{\ell'}^{m'}\right\rangle = (-1)^{-\ell'+1-m}\sqrt{3}\begin{pmatrix}\ell' & 1 & \ell\\ m' & \mu & -m\end{pmatrix}\langle\ell||\nabla||\ell'\rangle \tag{3.33a}$$

$$\left\langle U_{n\ell}\mathcal{Y}_{\ell}^{m}\middle|r_{\mu}^{(1)}\middle|U_{n'\ell'}\mathcal{Y}_{\ell'}^{m'}\right\rangle = (-1)^{-\ell'+1-m}\sqrt{3}\begin{pmatrix}\ell' & 1 & \ell\\ m' & \mu & -m\end{pmatrix}\langle\ell||r||\ell'\rangle \tag{3.33b}$$

where $\langle\ell||\nabla||\ell'\rangle$ and $\langle\ell||r||\ell'\rangle$ are the reduced matrix elements independent of the orientation of the angular momentum [78]. The first advantage of using this theorem in the calculation of matrix elements applies to their actual computation. The reduced matrix elements involve radial integrals between B-splines and the operators, which are much more expensive part from a computational point of view compared to the $3j$-symbols. With this theorem we avoid calculation of these reduced matrix elements for all possible values of m and μ considerably reducing computation time. But the biggest advantage of the Wigner-Eckart theorem stems from the symmetry properties of the $3j$-symbols which makes them to be zero unless $m' + \mu - m = 0$ and $|\ell - 1| \leq \ell \leq \ell + 1$. Again, this translates into savings in computational resources, but, more importantly, establishes which transitions between states are allowed depending on the operator orientation. These allowed transitions can be summarized in the following selection rules:

$$\begin{array}{lll} x;\nabla_x \longrightarrow \Delta m = \pm 1 & \Delta\ell = \pm 1\\ y;\nabla_y \longrightarrow \Delta m = \pm 1 & \Delta\ell = \pm 1\\ z;\nabla_z \longrightarrow \Delta m = 0 & \Delta\ell = \pm 1 \end{array} \tag{3.34}$$

Although these selection rules have been derived from the calculation of one-electron matrix elements, they are still valid for the coupling between two-electron states. Given that the eigenstates of H_2 are also eigenstates of L_z with $M = m_1 + m_2$ eigenvalue, and that they have defined parity associated to the spherical harmonics included in the one-center expansion, the symmetry of the final state can be easily deduced from the selection rules. By using the selection rules and the multiphoton interpretation derived from perturbation theory we can even know the symmetry of the final state for transitions involving several photons. For transitions of order one, the selection rules tells us that these transitions connect states with different parity ($g \to u$ or $u \to g$). It also tells us that, when the operator is perpendicular to the molecular axis, there is a difference of one in the quantum number M between the initial and final states. For the case of an operator parallel to the nuclear axis, there is no change in M. For transitions of order two the selection rules become:

$$\begin{array}{lll} x;\nabla_x^{(N=2)} \longrightarrow \Delta m = 0, \pm 2 & \Delta\ell = 0, \pm 2\\ y;\nabla_y^{(N=2)} \longrightarrow \Delta m = 0, \pm 2 & \Delta\ell = 0, \pm 2\\ z;\nabla_z^{(N=2)} \longrightarrow \Delta m = 0 & \Delta\ell = 0, \pm 2 \end{array} \tag{3.35}$$

It is worth noting that, although the position and momentum operators in a given direction have the same selection rules, they produce different outcomes in our Hamiltonian. In our approximation of the interaction with radiation in the velocity gauge the position matrix elements associated, with non-dipole effects, are related to the propagation direction of the pulse. Whereas, the momentum matrix elements, associated with the dipole approximation, do so with the polarization direction. Since both propagation and polarization vectors are perpendicular to each other, dipole and non-dipole transitions have different selection rules for a given configuration of the laser pulse.

3.4 Observables

Experimental observations have long been able to retrieve information relative to the energy of the different fragments produced in photoionization, with spectra resolved either in photoelectron energy, in nuclear kinetic energy, or both. Recent advances in experimental detection have also allowed the detection of fully differential quantities in all angles and energies of photofragments, which have helped unveil detailed information otherwise hidden in the angle integrated spectra. From an experimental point of view, it implies that all fragments must be detected in coincidence to retrieve their individual momenta. Microscopes making use of velocity map imaging (VMI), velocity correlation (VC) methods, or cold target recoil ion momentum spectroscopy (COLTRIMS) techniques are able to provide the velocity vectors for all the fragments produced from a single target molecule. Moreover, COLTRIMS experiments in H_2 are even able to know in which atomic center the residual electron is localized after dissociative photoionization, see Ref. [49] an references therein.

Our implementation of the Feshbach partitioning scheme together with the description of continuum state by means of a multichannel scattering approach allows us to directly relate the coefficients of the expansion of the total wave function to true ionization amplitudes. As stated before, for long enough propagation times, the eigenstates of the $\mathcal{P}$ and $\mathcal{Q}$ subspaces are also eigenstates of the total Hamiltonian of the system. This propagation time has to be longer than the pulse duration and long enough so that all resonant states have either dissociated or decayed into the continuum. In practice, this usually means propagation times equal to the duration of the pulse plus four femtoseconds. Since our total wave function is expanded on a basis of states belonging to the $\mathcal{P}$ and $\mathcal{Q}$ subspaces, when the previous condition is fulfilled, we can use the coefficients of the total wave function to calculate differential probabilities. These differential probabilities can be directly related to resolved spectra obtained from experiments since our description of continuum states incorporates asymptotic boundary conditions.

The doubly differential probability in both electronic (ε_α) and vibrational (E_{ν_α}) energies for each partial wave (ℓ_α) of each ionization threshold (α) can be written as:

$$\frac{d^2 P_{\ell_\alpha}}{dE_{\nu_\alpha} d\varepsilon_\alpha} = \left| C^{\varepsilon_\alpha}_{\alpha \ell_\alpha \nu_\alpha}\left(t_f\right) \right|^2 \tag{3.36}$$

where t_f is the propagation time fulfilling the conditions mentioned above. In order to obtain PES or nuclear kinetic energy release (KER) spectra, one simply has to integrate the above expression in either electronic or nuclear energy and sum over

the different ionization and dissociation channels included in the calculation.

$$\frac{dP}{dE_\nu} = \sum_{\alpha\ell_\alpha} \int \mathrm{d}\varepsilon_\alpha \left| C^{\varepsilon_\alpha}_{\alpha\ell_\alpha v_\alpha}(t_f) \right|^2 \tag{3.37}$$

$$\frac{dP}{d\varepsilon} = \sum_{\alpha\ell_\alpha} \sum\!\!\!\!\!\!\int_{v_\alpha} \mathrm{d}E_{v_\alpha} \left| C^{\varepsilon_\alpha}_{\alpha\ell_\alpha v_\alpha}(t_f) \right|^2 \tag{3.38}$$

Integrating over electronic and nuclear energies we obtain the total ionization yield.

When analysing results differential in only photoelectron energy or nuclear kinetic energy, one has to take into account that, unlike with atoms for which the excess energy from photoabsorption is always transferred to the electrons, the excess energy in molecules is shared between both electrons and nuclei in different ways. While these expressions produce results that can be directly compared to experimental observations, we also make use of truncated spectra in which we select specific ionization channels to gain a deeper understanding on their role in the photoionization dynamics.

Molecular frame photoelectron angular distributions (MFPADs) can also be obtained from the coefficients of the total wave function. In order to obtain triply differential ionization probabilities, differential in the ejection solid angle $d\Omega_e$ and electronic and nuclear energies, first we need to project the total wave function with

$$\Psi^-_\alpha(\mathbf{r}, R, t) = \sum_{\ell_\alpha} i^{\ell_a} e^{-i\sigma_{\ell_a}(\varepsilon_\alpha)} \mathcal{Y}^{m_\alpha *}_{\ell_\alpha}(\mathbf{k}_e)\, \psi^{\varepsilon_\alpha}_{\alpha\ell_\alpha m_\alpha}(\mathbf{r}, R) \chi_{v_\alpha}(R) e^{-iW_{\alpha v_\alpha} t}. \tag{3.39}$$

This is the asymptotic wave function satisfying incoming boundary conditions, similar to that of equation 1.33, that describes an electron ejected through the αth ionization threshold, in the direction $\boldsymbol{k}_e \equiv d\Omega_e$, written as a partial wave decomposition in spherical harmonics [52]. The resulting triply differential probability reads as:

$$\frac{d^3P}{dE_{v_\alpha} d\varepsilon_\alpha d\Omega_e} = \left| \sum_{\ell_\alpha} i^{-\ell_\alpha} e^{i\sigma_{\ell_\alpha}(\varepsilon_\alpha)} \mathcal{Y}^{m_\alpha}_{\ell_\alpha}(\mathbf{k}_e)\, C^{\varepsilon_\alpha}_{\alpha\ell_\alpha v_\alpha}(t_f) \right|^2 \tag{3.40}$$

3.4.1 Cross-section

Measurement of cross-sections is also very useful and commonly used in the analysis of scattering results. This quantity measures the probability that a specific event takes place and is defined as the ratio of the number of events of a certain type per unit time and per unit scatterer, to the flux of the incident particles with respect to the target [79]. In the case of photoionization cross-sections the incident beam is the laser and the event considered is ionization and it is defined as

$$\sigma^{(N)} = \frac{\Gamma^{(N)}}{F^N}, \tag{3.41}$$

where $\Gamma^{(N)}$ is transition rate, F is the flux and N is the order of the event in perturbation theory. This particular definition of the cross-section is also known as the generalized cross-section and is often used in multiphoton ionization where it is measured in units of $cm^{2N} s^{(N-1)}$. Unlike PES and MFPADs, cross-sections are independent of the laser parameters and are directly related to the structure of the molecule and its dipole transition moments.

The measurement of photoionization cross-sections usually requires long pulse durations and not too high intensities, for this reason, they are often obtained in experiments performed with synchrotron radiation. These kinds of conditions make perturbation theory the ideal tool to calculate cross-sections. The photoionization rate can be calculated from transition amplitudes obtained from TDPT as shown below

$$\Gamma_{i\to f}^{(N)} = \lim_{t\to\infty} \int \frac{d}{dt} \left| \langle \psi_f | U^{(N)}(t, t_0) | \psi_i \rangle \right|^2 \rho_f(E) dE \tag{3.42}$$

where $\rho_f(E)$ is the density of final states. The previous expressions apply for the cases where the final state belongs to the continuum part of the spectrum. That can represent either an ionization situation, where the electron is ejected into the continuum or the scattering of light, where the photon energy is also a continuum variable.

Part II

Electron-nuclear dynamics with UV pulses

Chapter 4

Harmonic filtering effects in attosecond pulse trains

Observation in real-time of microscopic motion requires the ability to obtain observables as a function of the delay between the event that triggers the dynamics and the subsequent probing of the evolution of the system. Well-characterized laser pulses from high-harmonic generation (HHG) provide nowadays the necessary attosecond resolution to explore atomic and molecular dynamics, enabling the manipulation of electron motion at its natural timescale. In this endeavor, the combination of a single attosecond pulse (SAP) or an attosecond pulse train (APT) in the UV/XUV region with an IR field in a pump-probe scheme has proven to be a very successful technique to investigate the laser-induced coupled electron-nuclear dynamics in small molecules. Particularly, pump-probe schemes have been used to control the ionization yield in atoms by means of electron wave packet interference [80] and have opened the door for the study of nuclear wave packet dynamics in molecules [15,81].

In contrast with the broad bandwidth of SAPs, which have little state selectivity, the narrow bandwidth of each harmonic in an APT allows to precisely exciting multiple states enabling accurate control of photoionization [82]. This ability to specifically excite several states can be used to control nuclear and electronic dynamics through interference between quantum pathways that end up in the same final state [83,84]. Specifically, recent experiments in H_2 employed a phase-locked comb of attosecond VUV harmonics with an IR femtosecond laser pulse in a VUV pump-IR probe scheme demonstrating that the IR probe can be used to control excitation and ionization yields on attosecond timescales by means of electron wave packet interference [32]. From a theoretical perspective, the possibility for coherently and simultaneously controlling both electronic and nuclear dynamics, specifically populating different vibronic states, demands theoretical approaches which go beyond the BO approximation to be understood.

In the generation of APTs with HHG, spectral filters such as monochromators, thin metal filters, glass windows, or multilayer-coated mirrors are commonly used to suppress certain harmonics. The capacity to select specific photon energies is essential for understanding the molecular dynamics derived from particular electronic transitions [85]. Otherwise, other processes can obscure the contribution from those specific transitions increasing the complexity of the dynamics. Moreover, the ability to manipulate the spectral content of the harmonics is crucial for controlling the coupled electron-nuclear dynamics triggered by coherent ultrashort pulses. In this chapter, we present *ab initio* calculations performed on H_2 in a XUV pump-UV probe scheme using an ATP to investigate the possibility of control excitation, dissociation, and ionization yields by filtering different harmonics of the ATP.

4.1 Theoretical modelling

Our theoretical treatment of the pump-probe scheme is based on the TDFCC methodology described in detail in the first part of this thesis. The following Hamiltonian characterizes the interaction between the molecule and the electromagnetic field:

$$\mathcal{H} = \mathcal{H}_0 + \mathcal{V}_{DA}^{(1)}, \tag{4.1}$$

where $\mathcal{H}_0$ is the full-dimensional field-free Hamiltonian from equation 1.3, and $\mathcal{V}_{DA}^{(1)}$, representing the interaction with radiation, is the dipole operator defined in equation 2.34a. For the laser parameters considered in this chapter, the wavelength of the electromagnetic field is long enough compared with the size of the system and the intensity is low enough so that we can neglect the non-dipole terms $\mathcal{V}_{RET}^{(1)}$ and $\mathcal{V}_{RET}^{(2)}$ from equations 2.34b and 2.34c. For our study, we addressed the case of polarization parallel to the internuclear axis for both pump and probe. This results in the following expression for the Hamiltonian:

$$\mathcal{H} = \mathcal{H}_{el} + T_N + A(t) \sum_i P_{z_i} \tag{4.2}$$

where $\mathcal{H}_{el}$ and T_N are the electronic Hamiltonian and the nuclear kinetic energy operator of the field-free molecule, defined in equation 1.4, and the last term is the dipole operator in the velocity gauge for our particular laser configuration. The previous dipole interaction term only allows for transitions between states with the same z-component of the angular momentum and different parities. For a molecule initially in the ground state $X^1\Sigma_g^+$, this means that only ${}^1\Sigma_g^+ \leftrightarrow {}^1\Sigma_u^+$ transitions are allowed. The absorption of an odd number of photons, usually dominated by the one-photon absorption, will populate states of symmetry ${}^1\Sigma_u^+$ and the absorption of an even number of photons will reach states of ${}^1\Sigma_g^+$ symmetry.

The XUV pump consists of an APT with a total duration of $T = 6$ fs generated from an 800 nm IR field with the 9$^{\text{th}}$ harmonic as the central frequency of the train ($\omega = 13.95$ eV) and an intensity of $1.4 \cdot 10^9$ W/cm^2. Two different trains were considered to investigate the effects of harmonic filtering. A first one, corresponding to the unfiltered train, containing harmonics up to the 17$^{\text{th}}$, and a second one, emulating the effects of filtering the higher harmonics of the train, containing only up to the 9$^{\text{th}}$ harmonic. The probe pulse employed consists of the 3$^{\text{rd}}$ harmonic of the same 800 nm IR field ($\omega = 4.65$ eV) used to generate the APTs with a total duration of $T = 6$ fs and an intensity of $3.0 \cdot 10^{11}$ W/cm^2.

Bearing in mind the duration and photon energy of the pulses, our theoretical description of the field-free states needs to include resonant states to account for autoionization. We included in our calculations the first six bound sates, the first two series, $\mathcal{Q}_1$ and $\mathcal{Q}_2$, of resonant states, and the first two ionization thresholds $1s\sigma_g$ and $2p\sigma_u$ with partial waves up to $\ell = 7$ for both ${}^1\Sigma_g^+$ and ${}^1\Sigma_u^+$ symmetries. The expansion of the mono-electronic orbitals contains angular momenta up to $\ell_{max} = 16$ and 410 B-splines supported in an electronic box with $r_{max} = 60$ a.u.. The vibrational wave functions were calculated with 240 B-splines in a box of $R_{max} = 12$ a.u.. This particular set of parameters has been used in the past for similar calculations of the group yielding excellent results when comparing with experimental measurements.

Throughout this chapter we use ${}^1\Sigma_g^+$ and ${}^1\Sigma_u^+$ to refer to the symmetry of the total two-electron wave function of bound, resonant or continuum states. To refer to the one-electron ionic states we use the terms $1s\sigma_g$ and $2p\sigma_u$.

4.2 Quantum pathways

In figure 4.1 we show the schematics of our pump-probe simulation with the main quantum pathways, which indicate that ionization is mostly due to one-photon absorption from the higher harmonics of the train or two-photon absorption from a combination of the central or lower harmonics of the train and the probe. For the laser parameters considered here, the probe pulse has enough intensity and photon energy to ionize a molecule already in an electronic excited state but not enough to directly ionize it from the ground state, a process that would require the much less probable absorption of four photons. Similarly, the intensity of the pump makes the absorption of more than one XUV photon very unlikely. We also neglect any distortion of the field-free states and any contribution from tunnel ionization based on the fact that the Keldysh parameter is much greater than one.

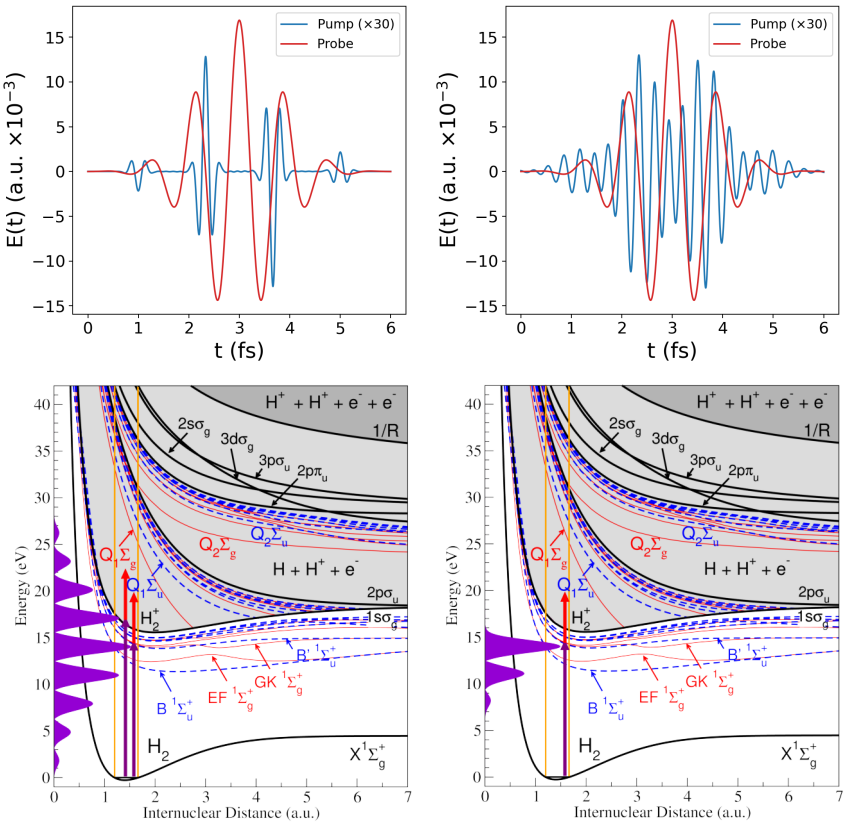

FIGURE 4.1 – Schematics of the pump-probe simulation for the unfiltered (left panels) and filtered (right panels) cases. Top panels represent the vector potential of the pump (intensity multiplied by a factor of 30 for clarity) and probe. Bottom panels represent the Fourier Transform of the pump on top of the potential energy curves of H_2 with purple and red arrows representing the possible quantum pathways of the XUV harmonics and probe photons, respectively. The two vertical lines of the potential energy curve diagram represent the Franck–Condon region determined by the vibrational ground state $v_g = 0$ of H_2.

In figure 4.2, we see the total photoelectron yields for dissociative and non-dissociative ionization as a function of the delay between the pump and probe for

both unfiltered and filtered APTs. For both cases, the dominant process is non-dissociative ionization, representing more than 95% of total ionization yield for the unfiltered case and around 80% for the filtered case. The dependence of the non-dissociative yields with the delay between the pump and the probe are in accordance with our initial hypothesis on the main ionization pathways shown in figure 4.1. The constant ionization yield at all delays for the unfiltered case suggests that the probe does not play a significant role in non-dissociative ionization. The main contribution seems to be the absorption of a XUV photon from the higher harmonics of the train. For the filtered train, this process is no longer energetically allowed, so we observe a modulation of the non-dissociative ionization yield with the delay indicating absorption of photons from both the pump and the probe. As a result of the one-photon absorption route being suppressed, we also observe a significant decrease in the total ionization yield. On the other hand, the dissociative yield shows a dependence on the delay for both filtered and unfiltered trains. The different dependence on the delay for both cases, however, suggests different dissociative routes.

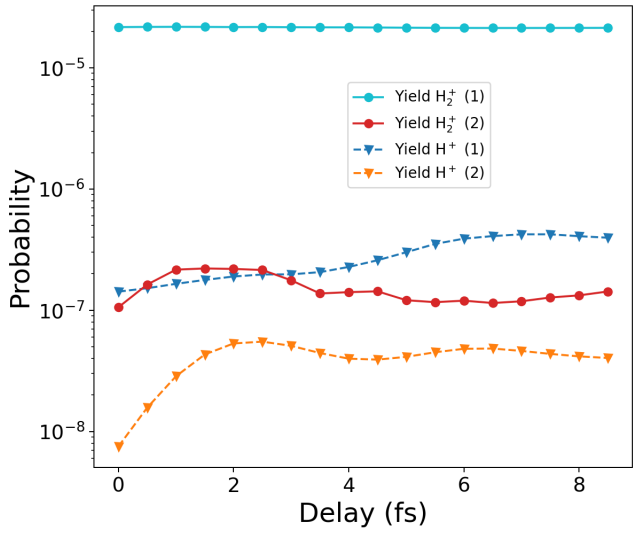

FIGURE 4.2 – Calculated H_2^+ and H^+ yields as a function of the delay between the unfiltered (1) and filtered (2) APT and the probe.

For a better understanding of the different dissociative routes, figure 4.3 shows the contribution from each ionization threshold included in the calculation. The main difference between the two cases is the suppression of the $2p\sigma_u$ dissociative channel for the filtered case, which is the main dissociative route for the unfiltered case at longer delays. Looking at dissociation through the first ionization threshold, we observe a similar modulation with the delay for both cases. The constant difference between the two yields can be attributed to the effect of one-photon ionization to a dissociative state of $1s\sigma_g$, which is not possible for the filtered case. This similar modulation indicates a common underlying dynamics for both cases. For the filtered case, this dynamics is the main contribution, but for the unfiltered case, it is obscured by more dominant processes.

As mentioned in Chapter 3, with our theoretical implementation, we are able to retrieve fully differential probabilities both in energy and angle of the emitted photoelectron, that experimentally require to perform coincidence measurements, which are significantly more challenging from the experimental point of view. However,

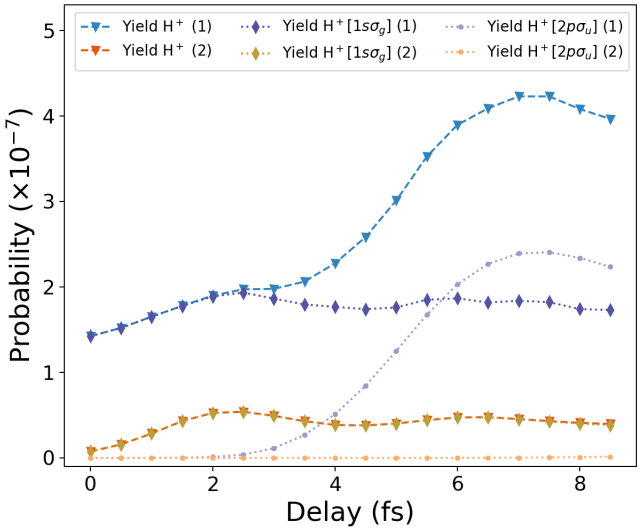

FIGURE 4.3 – Calculated H^+ yields as a function of the delay between the unfiltered (1) and filtered (2) APT, and the probe with their corresponding contributions from the ionic states $1s\sigma_g$ and $2p\sigma_u$.

energy-differential observable are commonly retrieved in photoionization experimental set ups. In between the fully differential probabilities and the fully integrated yields, kinetic energy release distributions integrated in electronic or nuclear energy give a more detailed description of the dynamics of photoionization while keeping a more readable picture of the evolution of the system as a function of the delay. In the following sections, we present an analysis of the dynamics of H_2 induced by our pump-probe scheme by investigating the different ionization probabilities as a function of the nuclear kinetic energy (NKE) or the electron kinetic energy (EKE) and the delay.

4.3 Dissociative ionization

We begin with the analysis of the different quantum pathways leading to dissociative ionization and the effects of the delay on both unfiltered and filtered cases. Figure 4.4 shows the total NKE spectrum for the unfiltered case with the truncated spectra corresponding to its three main contributions. These contributions consist of i) one-photon ionization to the ground state of H_2^+, ii) two-photon ionization to the ground state of H_2^+, and iii) two-photon ionization to the $2p\sigma_u$ excited state of H_2^+.

Energetically, the only possibility for direct dissociative ionization from the ground state is by absorption of the 13^{th} harmonic of the unfiltered train. As shown in the truncated NKE distribution for the ${}^1\Sigma_u^+(1s\sigma_g)$ continua, this process produces a constant signal with the delay at low NKE. The rapid decrease of the probability with NKE is consistent with results from previous works on direct ionization [86, 87].

The second contribution, two-photon ionization into the ground state of H_2^+, produces a periodic signal in the ${}^1\Sigma_g^+(1s\sigma_g)$ truncated NKE distribution, with maximums for delays of 2 and 6 fs, and a minimum at 4 fs. The delay-dependent signal maps the dynamics of the excited states of the neutral molecule, populated by the absorption of the 9^{th} harmonic of the train and then ionized by the delayed absorption of a photon from the probe.

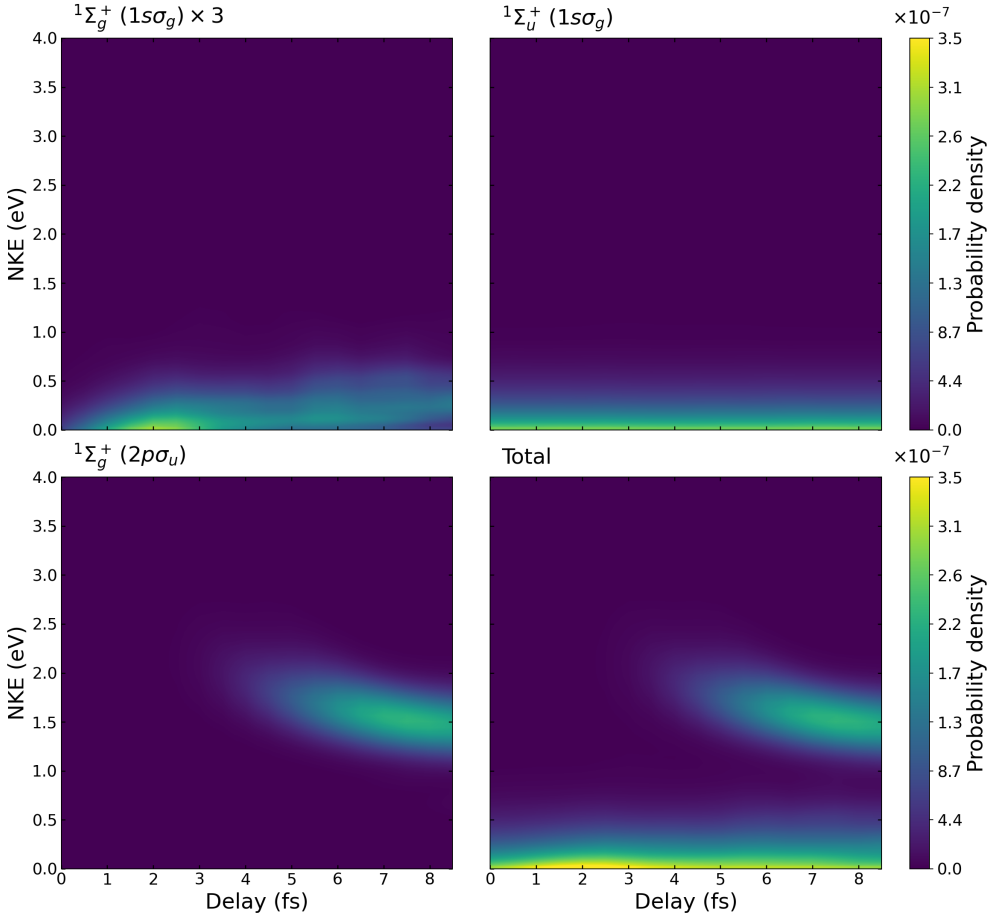

FIGURE 4.4 – Probability of dissociative ionization as a function of the NKE and the delay between the unfiltered APT and the probe. The three major contributions from each final total symmetry of the two-electron system ($^1\Sigma_g^+$ and $^1\Sigma_u^+$) and ionic states (1sσ_g and 2pσ_u) are represented in the top (left and right) and bottom left panels. The total probability is plotted in the bottom right panel.

The last contribution appears for delays longer than 4 fs in the $^1\Sigma_g^+(2p\sigma_u)$ truncated spectrum and progressively moves to lower NKE with the delay. This process starts with the creation of a nuclear wave packet that evolves in time towards larger internuclear distances where the energy needed to access 2pσ_u decreases, which explains the appearance of the signal at longer delays. At this point, the probe can promote the wave packet to the potential energy curve of 2pσ_u with the absorption of a photon from the probe. To elucidate the nature of the nuclear wave packet created by the pump, we performed a truncated calculation with no couplings between continuum states; the resulting total NKE spectrum is shown in figure 4.5. The absence of the signal corresponding to two-photon absorption to 2pσ_u implies that, in the full calculation, this process requires above-threshold ionization (ATI) of a nuclear wave packet in the ground state of the ion. Thus, this process implies the absorption of a photon from the 11$^{\text{th}}$ harmonic of the train and the subsequent absorption of a photon from the probe.

Unlike with the unfiltered case, which has one-photon absorption and ATI as the dominant processes in dissociative ionization, with the filtered train, the only major contribution to the total NKE spectrum comes from two-photon absorption to the ground states of the ion as seen in figure 4.6. Although this contribution

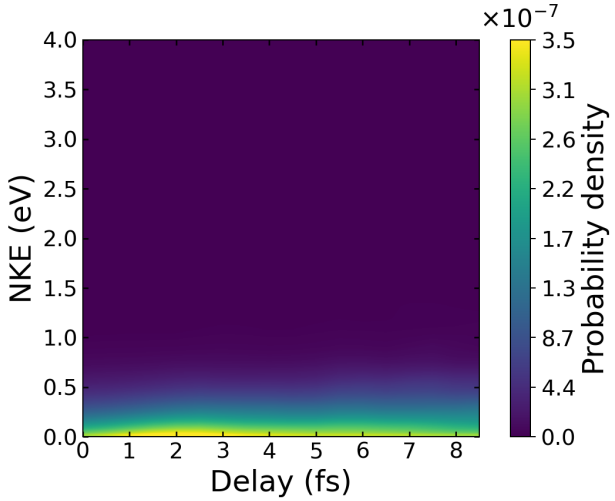

FIGURE 4.5 – Total probability of dissociative ionization as a function of the NKE and the delay between the unfiltered APT and the probe for a truncated calculation in which contribution from ATI terms has been removed.

is present in the unfiltered case, it is three times less intense compared to the two main processes. However, the resemblance of the total NKE spectrum for the filtered case with the ${}^1\Sigma_g^+(1s\sigma_g)$ truncated spectrum for the unfiltered case, shown in the upper left panel of figure 4.4, indicates that harmonic filtering does not alter the temporal evolution of the excited molecule. By filtering the higher harmonics in the train, one can thus extract the ionization signal solely associated with the two-photon absorption through the excited neutral molecule and, in this way, recover its dynamics as a direct map.

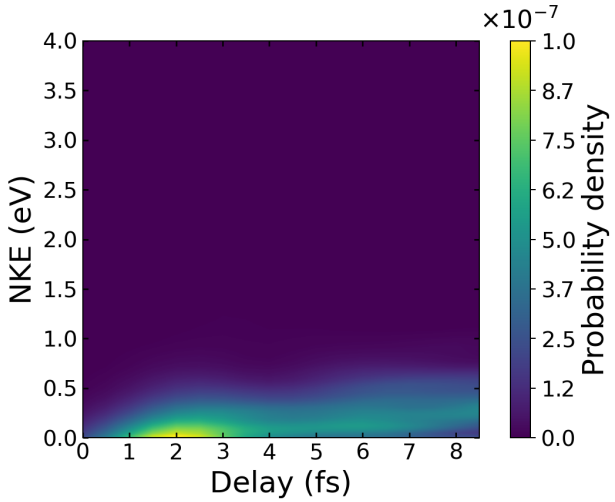

FIGURE 4.6 – Probability of dissociative ionization as a function of the NKE and the delay between the filtered APT and the probe. The major contribution to the total probability comes from the final symmetry ${}^1\Sigma_g^+$ and the ionic state $1s\sigma_g$.

A similar analysis as the one presented above for the different contributions to

the NKE spectrum can be made for the probabilities of dissociative ionization differential in EKE (integrated in NKE) shown in figure 4.7. For the unfiltered train, again, contributions from three different channels compete: one-photon ionization to $1s\sigma_g$, two-photon absorption to $1s\sigma_g$, and two-photon absorption to $2p\sigma_u$. One-photon absorption to $1s\sigma_g$ shows a similar delay-independent probability appearing for EKE between 1.5-2.0 eV. This value for the kinetic energy of the electrons comes from the excess energy resulting from the absorption of the 13^{th} harmonic of the train taking into account that the nuclei barely gain any kinetic energy. Two-photon absorption to $1s\sigma_g$ shows a similar periodic dependence with the delay as its differential in NKE counterpart. Finally, the same increase in the probability for longer delays appears for two-photon ionization to $2p\sigma_u$. In this case, however, the spectrum moves towards higher energies with the delay in accordance with a constant value for the excess energy shared between the electrons and the nuclei. The results from the calculations without ATI terms also show a disappearance of this signal in agreement with our previous results. Similarly to what we noticed in the NKE spectra, by filtering the higher harmonics of the train, we erase the contribution from one-photon ionization and ATI retrieving the same EKE spectrum as the one shown in the upper left panel of figure 4.7 corresponding to the ${}^1\Sigma_g^+(1s\sigma_g)$ contribution.

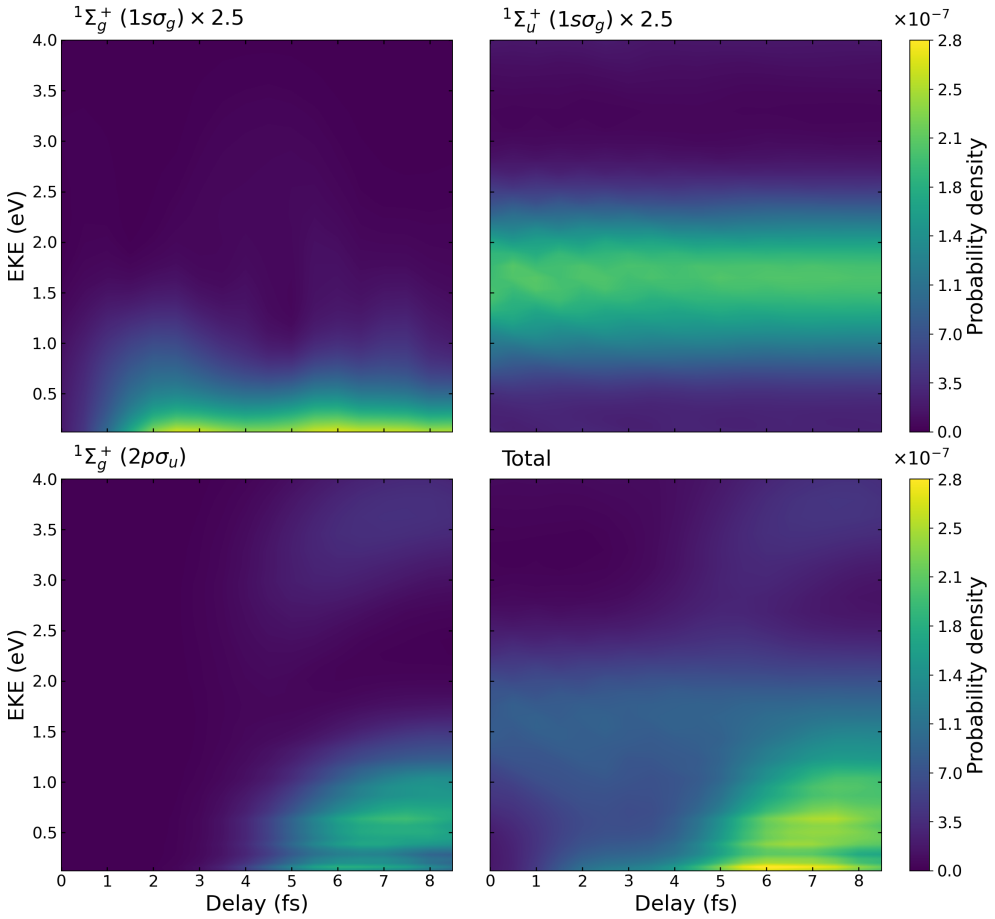

FIGURE 4.7 – Probability of dissociative ionization as a function of the EKE and the delay between the unfiltered APT and the probe. The three major contributions from each final total symmetry of the two-electron system (${}^1\Sigma_g^+$ and ${}^1\Sigma_u^+$) and ionic states ($1s\sigma_g$ and $2p\sigma_u$) are represented in the top (left and right) and bottom left panels. The total probability is plotted in the bottom right panel

4.4 Non-dissociative ionization

Unlike for the case of dissociative ionization, our analysis of the probability of non-dissociative ionization as a function of the delay, shown in figure 4.8, reveals only one major contribution for both unfiltered and filtered cases. These contributions come from one-photon and two-photon absorption, respectively. The spectra of the unfiltered case show the usual delay-independent signal consistent with one-photon absorption. The main mechanism is the absorption of the 11^{th} harmonic of the train, which mainly populates the first vibrational states of the ion and produces electrons with kinetic energy between 0.5-1.0 eV. A slightly visible interference pattern appears in the EKE spectrum of the unfiltered case, which was found to be caused by higher-order processes involving the resonant states of the molecule.

The two-photon ionization pathway of the filtered case presents a more complex dependence on the delay as it involves the evolution of the excited neutral molecule. From the experimental point of view, this implies that one can use a filter to uncover the two-photon signal from the dominant one-photon signal of the higher harmonics of the train. The ionization probability as a function of the vibronic energy of the ion, shown in the lower-left panel of figure 4.8, shows that, for delays around 2 fs, two maxima appear, one for vibrational states with a low quantum number ($\nu = 1-5$) and another for states with a higher quantum number ($\nu = 10-15$). At those same delays, the EKE spectrum shows only one signal appearing at 0.5 eV. This particular sharing of the excess energy between electrons and the nuclei is explained by the simultaneous action of two interfering mechanisms involving the 7^{th} and 9^{th} harmonics of the train. For longer delays, the population of vibrational states of H_2^+ moves towards intermediate quantum numbers ($\nu = 5-10$), and the corresponding EKE spectrum shows a weaker signal than before for EKE around 2.5 eV. In this case, however, the process only involves the absorption of the 9^{th} harmonic of the train and a photon from the probe as the combination of the 7^{th} harmonic and the probe does not provide enough energy to produce these signals.

After inspection of the truncated spectra for the unfiltered case, we found the same contribution from two-photon ionization to $1s\sigma_g$ as the one obtained for the filtered case. However, in this case, a difference of two orders of magnitude between the signals completely overshadows its contribution to the total non-dissociative photoionization process.

So far we have shown that two-photon ionization to $1s\sigma_g$ involves absorption of the 7^{th} and 9^{th} harmonics of the train for non-dissociative ionization and the 9^{th} harmonic for dissociative ionization. These two harmonics directly populate the $B\,^1\Sigma_u^+$ and $B'\,^1\Sigma_u^+$ excited states of the molecule, which indicates that the observed modulation of ionization with the delay is a direct consequence of the dynamics of these excited states. Figure 4.9 shows the excitation probability for the different vibrational states of both $B\,^1\Sigma_u^+$ and $B'\,^1\Sigma_u^+$ for a calculation including the pump. The perfect agreement between the filtered and unfiltered cases reinforces the idea that harmonic filtering does not alter the dynamics of the excited molecule. The absorption of the two aforementioned harmonics translates into the appearance of two distinguishable groups of vibrational states whose coherent superposition creates a molecular wave packet that evolves in time. The first group appears in the lower vibrational states of $B\,^1\Sigma_u^+$ and is originated by the absorption of the 7^{th} harmonic of the train. The second group consists of both the higher vibrational states of $B\,^1\Sigma_u^+$ and the lower vibrational states of $B'\,^1\Sigma_u^+$. The modulation of the two-photon absorption probability with the delay can then be related to interferences between the different vibronic components of a molecular wave packet.

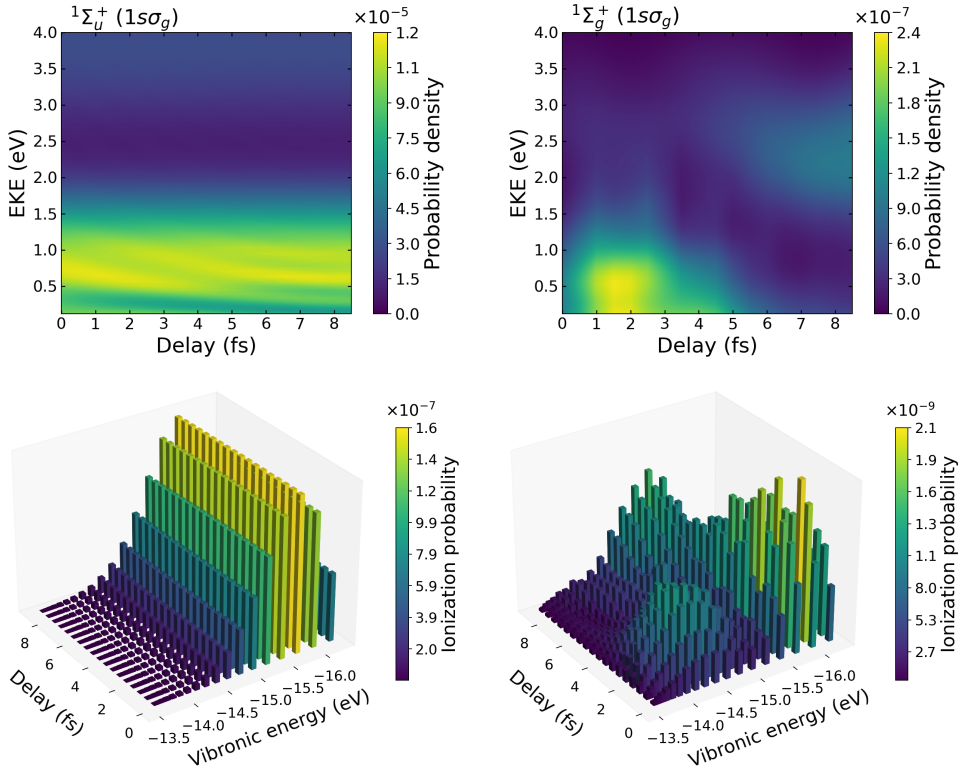

FIGURE 4.8 – Probability of non-dissociative ionization as a function of the EKE (upper panels) and the vibrational energy of the ion (lower panels) and the delay between the unfiltered (left panels) and filtered (right panels) APT and the probe. The only major contribution for the unfiltered case comes from one-photon ionization while two-photon ionization does so for the filtered case.

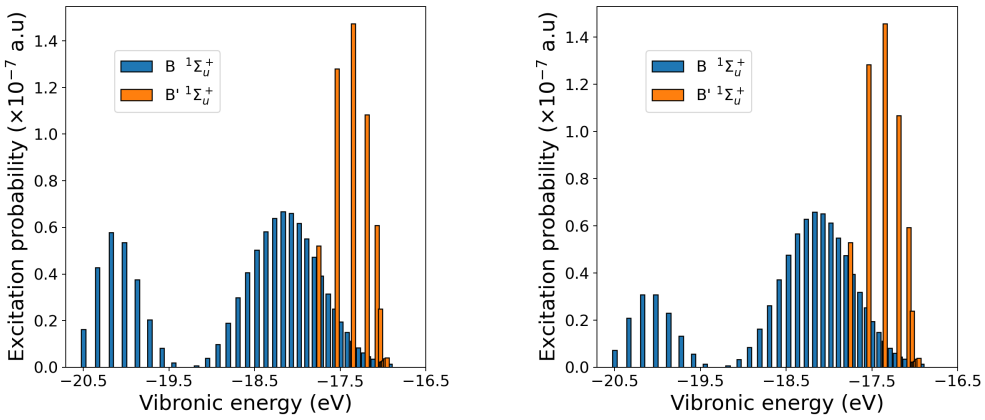

FIGURE 4.9 – Probability of excitation to vibronic molecular bound excited states of H_2 B and B′ with and unfiltered (left panel) and filtered (right panel) APT.

4.5 Asymmetry in the angular distributions

The suppression of one-photon ionization over two-photon ionization by filtering the higher harmonics of the APT also affects the molecular frame angular distributions (MFPADs) resulting from dissociative ionization. The interference between

one- and two-photon absorption paths, present only in the unfiltered case, produces asymmetries in the MFPADs due to states of different symmetry with respect to the inversion center of the molecule being populated. By filtering the higher harmonics of the APT, ionization is only due to two-photon absorption, which leads to a symmetric photoelectron ejection pattern. Experimentally, observation of these asymmetries requires to perform coincidence measures that detect the electrons and ions coming from the same event using a COLTRIMS reaction microscope. Theoretically, to satisfy the boundary conditions in which electron ejection angles are measured with respect to the ejection of the ion fragment, we need to project the total wave function onto a combination of *gerade* and *ungerade* ionization channels. This way, the wave function satisfies incoming boundary conditions that localize one of the protons in a given center. Since we have only included the first two ionization thresholds, these combination reads as

$$|\Psi^{-}_{u,d}\rangle = \frac{1}{\sqrt{2}}(|\Psi^{-}_{1s\sigma_g}\rangle \pm |\Psi^{-}_{2p\sigma_u}\rangle) \tag{4.3}$$

where u (Upward) and d (Downward) indicate the direction of the proton ejection, and $\Psi^{-}_{1s\sigma_g}$ and $\Psi^{-}_{2p\sigma_u}$ fulfill the same asymptotic conditions as 3.39. After projecting our total wave function with the previous combination, we obtain an expression for the fully differential probability in all angles and energies that is able to reproduce the asymmetries caused by the interference between the different dissociative channels associated with one-photon and two-photon ionization paths.

$$\frac{d^3P}{dE_v d\varepsilon d\Omega_e} = \frac{1}{2}\left|\sum_{\alpha=1s\sigma_g}^{2p\sigma_u}\sum_{\ell_\alpha} i^{-\ell_\alpha} e^{i\sigma_{\ell_\alpha}(\varepsilon_\alpha)} \mathcal{Y}^{m_\alpha}_{\ell_\alpha}(\mathbf{k}_e)\, C^{\varepsilon_\alpha}_{\alpha\ell_\alpha\nu_\alpha}(t_f)\right|^2 \tag{4.4}$$

The resulting MFPADs for dissociative ionization for several delays between the filtered and unfiltered APTs and the pump are shown in figure 4.10. As expected, for the filtered case the MFPADs are completely symmetric for all delays considered. The results for the unfiltered case show asymmetries indicating the coherent superposition of *gerade* and *ungerade* states. Moreover, by varying the delay we show the possibility of steering the direction of the ejection of the electron.

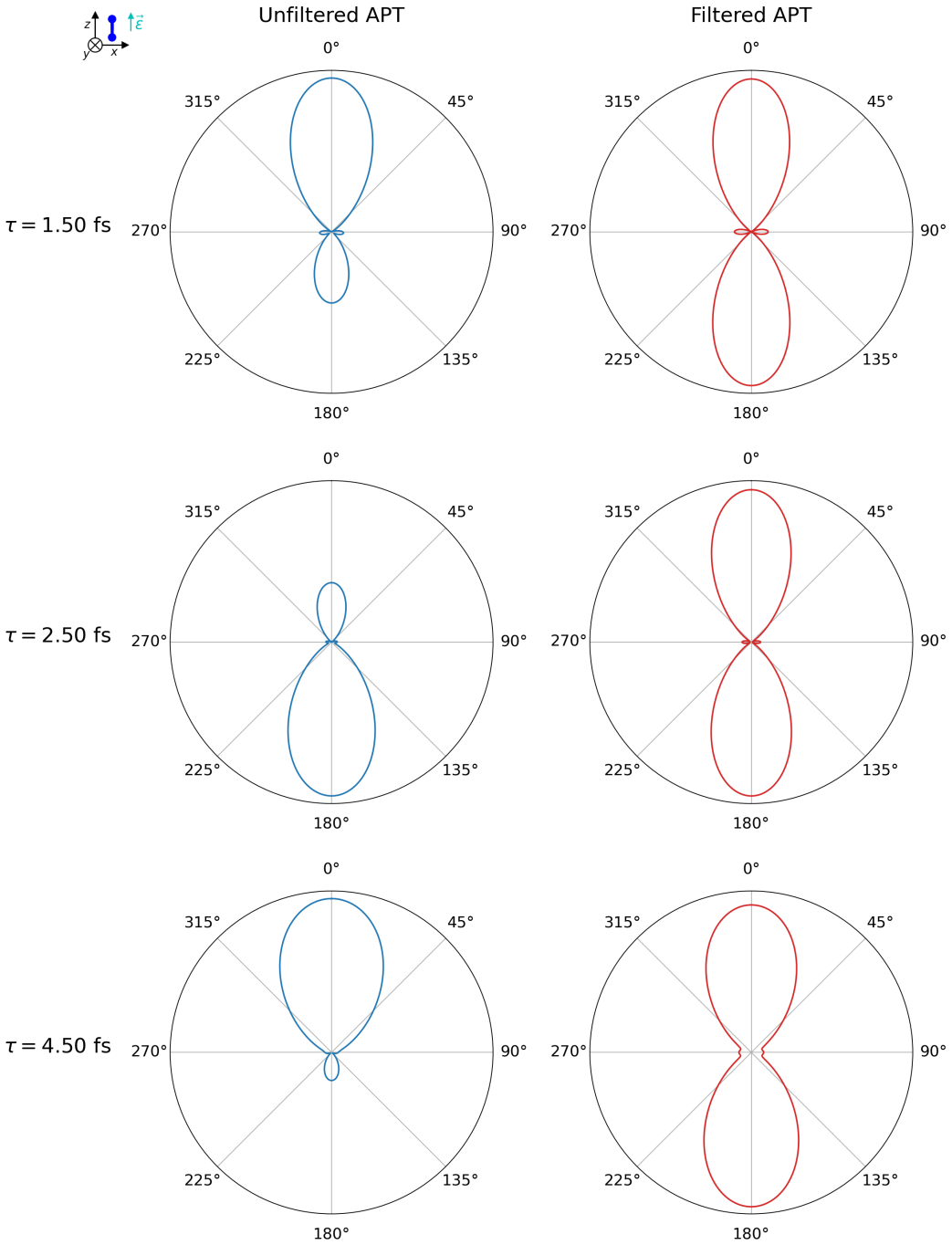

FIGURE 4.10 – 2D-projected MFPADs in the $z - o - x$ plane for dissociative ionization of H_2 with EKE=0.5 eV and NKE=0.2 eV for a pump-probe scheme with an unfiltered (left panels) and filtered (right panels) APT. Each row corresponds to different delays of the probe with respect to the APT.

Conclusions

In this part of the thesis, we have presented results for a XUV pump-UV probe scheme using an APT as pump and a single pulse as probe. We have studied the effect of harmonic filtering by analyzing the coupled electron-nuclear dynamics induced by two ATPs differing in the number of harmonics of their spectrum. We have shown that, by removing the higher harmonics of the spectrum of the APT, we are able to suppress one-photon ionization over two-photon ionization efficiently.

For the energies and laser intensities considered in the study, non-dissociative ionization is the most dominant ionization process for both the filtered and unfiltered cases studied. For this process, harmonic filtering significantly reduces the ionization yield and, by suppressing the one-photon ionization route, we are able to steer ionization by controlling the delay between pump and probe.

Through the analysis of differential probabilities in nuclear and electronic kinetic energy release, we have elucidated the main quantum pathways of both non-dissociative and dissociative ionization. For the unfiltered case, dissociative ionization happens mostly through one-photon absorption of the higher harmonics of the train and two-photon absorption through ATI. We have shown the possibility of control of dissociative channels for the unfiltered case as a function of the delay and have observed that ATI plays a key role. For the filtered case, the only contribution to dissociative ionization comes from two-photon absorption through the excited states of the molecule. This last contribution was also present for the unfiltered case, but it was obscured by the predominance of one-photon absorption and ATI. We observed no sign that harmonic filtering altered the temporal evolution of the excited molecule, so this technique can be used to recover the underlying dynamics of the excited states of H_2.

For non-dissociative ionization, we have shown that, by filtering the higher harmonics of the pump, we can control ionization by interference between vibronic wave packets formed in the $B\ ^1\Sigma_u^+$ and $B'\ ^1\Sigma_u^+$ excited states of H_2.

Finally, we have shown that asymmetries in the MFPADs are produced in the unfiltered case as a consequence of states of different symmetry with respect to the inversion center of the molecule being populated. We have also shown that control of the direction of ejection of the electron with the delay is possible. By eliminating the one-photon ionization route, the interference between states with different parity is no longer possible, so we have observed that harmonic filtering recovers symmetric MFPADs.

Part III

Stimulated Raman and Compton scattering

Chapter 5

Perturbative treatment of stimulated Raman scattering

Raman spectroscopy is a widely used technique based on the inelastic scattering of light by matter, with many applications in chemistry and material science for its inherent sensitivity to identify vibrational modes in molecular and solid-state systems. Spectroscopic techniques that make use of spontaneous Raman emission, however, have very low sensitivity due to the small cross-section of this process. Several techniques based on coherent Raman scattering have been proposed to enhance sensitivity over the years, one of them being Stimulated Raman Spectroscopy. This family of techniques is based on the non-linear phenomenon of Stimulated Raman Scattering (SRS), discovered shortly after the invention of the laser [88,89], which employs two incident fields with different photon energies ω_1 and ω_2 such that $\omega_1 > \omega_2$. In SRS, the system is excited by the absorption of ω_1 and then it relaxes by the stimulated emission of a photon with energy ω_2, the difference $\omega_1 - \omega_2$ is absorbed by the material. This increase in sensitivity has made SRS an attractive option for biological imaging [90,91].

With the advent of ultrashort laser pulses, time-resolved SRS techniques have enabled the direct observation of the coherent molecular motions at ultrafast time scales [92]. Additionally, the large bandwidth of ultrashort pulses opens the possibility for the study of electronic structure. Calculations with intense XUV and ultrashort X-ray pulses show that one can probe the dynamics of core-valence excitations in specific atoms of a molecule by using Stimulated X-ray Raman Spectroscopy (SXRS) [93]. Because of the photon energies involved in SXRS, intermediate states participating in the core-valence transition dynamics belong to the continuum, so ionization can occur. The low cross-section of Raman excitations in the XUV/X-ray region compared to direct photoionization makes the experimental observation of this phenomenon difficult. Nevertheless, recent calculations of stimulated Raman transitions at frequencies of 30–40 eV with pulse durations of a few femtoseconds have shown that Raman redistribution can overwhelm photoionization [94].

In the attosecond domain, HHG sources have dominated over the past two decades [1]. But the low conversion efficiency of HHG in the X-ray regime makes free-electron lasers the only viable source of high-intensity X-ray pulses to study the dynamics of core-valence excitations in the attosecond domain (the natural timescale for the electron motion). Regarding the theoretical treatment of these processes, studies and experiments in atoms and molecules have shown that the inclusion of effects beyond the dipole approximation becomes mandatory [25,26].

The second part of the results of this thesis centers on the study of non-dipole effects in the inelastic scattering of X-ray photons, with energies in the 0.6-1.6 keV range, by the H_2 molecule. In this chapter, we begin by studying non-dipole effects

in SRS and, in the next two chapters, we center on Stimulated Compton Scattering (SCS). This last process also involves the interaction with two incident fields of frequencies ω_1 and ω_2, as in SRS, but in this case, the energy difference $\omega_1 - \omega_2$ absorbed by the molecule leads to ionization. We neglect the effects of nuclear motion, assuming the validity of the FNA, and autoionization throughout this part partially justified by the fact that very-short pulses are used.

In the study of SCS and SRS with XUV/X-ray photons and the role of non-dipole effects, a key aspect is the relative contribution of the interaction terms $\boldsymbol{A} \cdot \boldsymbol{P}$ and $\boldsymbol{A}^2$. Whereas the contribution of the diamagnetic term $\boldsymbol{A}^2$ is zero in the domain where the dipole approximation is valid, it is the main responsible for the introduction of non-dipole effects in SCS and SRS. This term may even become dominant as the dipole contribution, coming from $\boldsymbol{A} \cdot \boldsymbol{P}$, diminishes because of partial cancellation of second-order contributions related to this term. This phenomenon can be intuitively understood in the framework of perturbation theory with the calculation of the Raman cross-section including retardation effects obtained from the Kramers-Heisenberg-Waller (KHW) formula [95, 96]. For the intensities and photon energies considered in our study, the theory of tunneling is not valid, and the use of TDPT is appropriate. The conclusions we extract from the study of the Raman cross-section regarding the relative contribution of dipole and non-dipole effects can be easily extended to the Compton case. However, due to the difficulties in the practical implementation of perturbative calculations in SCS we will restrict to Raman processes in this chapter.

In the calculation of the dipole contribution to the Raman cross-section, a correct description of the intermediate states lying in the high energy continuum is necessary. Even in the context of FNA an accurate description of these states is an arduous task given the high oscillatory behavior of the wave function at those energies and the number of open ionization channels. Previous to our analysis of the partial cancellation of the $\boldsymbol{A} \cdot \boldsymbol{P}$ term, we present a convergence study in the calculation of continuum states.

In the last section of this chapter, we reveal the first results on SRS with attosecond pulses in H_2. We employ a similar methodology as the one used in [97] for the hydrogen atom using several expressions derived from perturbation theory. At the end, we present a comparison with results obtained from non-perturbative calculations.

5.1 The Kramers-Heisenberg-Waller transition amplitudes

Our first step in the calculation of the Raman cross-section including retardation effects starts with the derivation of the KHW transition matrix elements. We begin with the determination of transition amplitudes in the context of TDPT with two overlapping in times monochromatic fields with potential vectors $\boldsymbol{A_1}(\boldsymbol{r}, t_1)$ and $\boldsymbol{A_2}(\boldsymbol{r}, t_2)$. The total amplitude can be divided into two contributions associated with the $\boldsymbol{A} \cdot \boldsymbol{P}$ and $\boldsymbol{A}^2$ operators.

$$U_{fi}^{KHW} = U_{fi}^{A \cdot P} + U_{fi}^{A^2} \tag{5.1}$$

As mentioned in Chapter 3, in first order perturbation theory, the $\boldsymbol{A} \cdot \boldsymbol{P}$ interaction operator is responsible for one-photon transitions, whereas $\boldsymbol{A}^2$ is responsible for two-photon transitions. This means that, to correctly describe a two-photon process

like SRS or SCS in lowest order perturbation theory (LOPT), the $\boldsymbol{A}\cdot\boldsymbol{P}$ term needs to be treated in second order. The resulting transition amplitudes read as:

$$\begin{aligned} U_{fi}^{A\cdot P} \equiv \langle\psi_f|U_{A\cdot\boldsymbol{P}}^{(2)}(t,t_0)\,|\psi_i\rangle &= (-i)^2\sum\!\!\!\!\!\!\int_m \int_{t_0}^{t} dt_1 \int_{t_0}^{t_1} dt_2 e^{iE_{fm}t_1}e^{iE_{mi}t_2} \\ &\times\left[\langle\boldsymbol{A_2}(r,t_1)\cdot\boldsymbol{P}\rangle_{fm}\langle\boldsymbol{A_1}(r,t_2)\cdot\boldsymbol{P}\rangle_{mi} + \langle\boldsymbol{A_1}(r,t_1)\cdot\boldsymbol{P}\rangle_{fm}\langle\boldsymbol{A_2}(r,t_2)\cdot\boldsymbol{P}\rangle_{mi}\right] \end{aligned} \tag{5.2a}$$

$$U_{fi}^{A^2} \equiv \langle\psi_f|U_{A^2}^{(1)}(t,t_0)\,|\psi_i\rangle = -i\int_{t_0}^{t} dt_1\; e^{iE_{fi}t_1}\langle\boldsymbol{A_1}(r,t_1)\cdot\boldsymbol{A_2}(r,t_1)\rangle_{fi} \tag{5.2b}$$

with the compact notation $E_{ba}\equiv E_b-E_a$, $\langle\boldsymbol{A}(r,t)\cdot\boldsymbol{P}\rangle_{ba}\equiv\langle\Psi_b\,|\boldsymbol{A}(r,t)\cdot\boldsymbol{P}|\,\Psi_a\rangle$, and $\langle\boldsymbol{A_1}(r,t_1)\cdot\boldsymbol{A_2}(r,t_1)\rangle_{ba}\equiv\langle\Psi_b\,|\boldsymbol{A_1}(r,t_1)\cdot\boldsymbol{A_2}(r,t_1)|\,\Psi_a\rangle$.

In the expression for the transition amplitudes associated with $\boldsymbol{A}^2$ we have neglected the contributions from $\boldsymbol{A_1}(r,t)\cdot\boldsymbol{A_1}(r,t)$ and $\boldsymbol{A_2}(r,t)\cdot\boldsymbol{A_2}(r,t)$ as, in the context of scattering of photons, these terms describe elastic processes. A similar reasoning was used for the transition amplitudes associated with $\boldsymbol{A}\cdot\boldsymbol{P}$. We use plane waves to represent the vector potential of an ideal monochromatic field:

$$\boldsymbol{A}(\boldsymbol{r},t) = A_0\,e^{-i(\omega t-\boldsymbol{k}\cdot\boldsymbol{r})}\boldsymbol{\epsilon}+c.c \tag{5.3}$$

where the first term corresponds to absorption of a photon with energy ω and the complex conjugate to the emission of a photon with the same energy. The wave vector $\boldsymbol{k}$ marks the propagation direction of the wave, $\boldsymbol{\epsilon}$ is the polarization vector, and A_0 is the amplitude of the field. The two terms that appear in the $\boldsymbol{A}\cdot\boldsymbol{P}$ transition amplitude represent the same processes of absorption of ω_1 and emission of ω_2, but with opposite time-ordering. We label the contribution that begins with the absorption of ω_1 followed by the emission of ω_2 as the direct path $(\boldsymbol{A}\cdot\boldsymbol{P}_D)$. On the other hand, the process that starts with the emission of ω_2 accompanied by the absorption of ω_1 is referred to as the inverse path $(\boldsymbol{A}\cdot\boldsymbol{P}_I)$. Unlike for the $\boldsymbol{A}\cdot\boldsymbol{P}$ contribution, where the process is sequential (but coherent in time), the absorption and emission processes in $\boldsymbol{A}^2$ are simultaneous, coming from the fact that it is described by a single matrix element.

Following a similar procedure as in [62], by setting $t_0=0$, neglecting the artificial sudden turning of the perturbation (*adiabatic swhitch-on*) and extending the integration over t_2 to infinity we obtain:

$$U_{fi}^{A\cdot P_D} = -iA_{0,1}A_{0,2}\left\langle e^{-i\boldsymbol{k}_2\cdot\boldsymbol{r}}P_{\boldsymbol{\epsilon}_2}G^{+}(E_i+\omega_1)e^{i\boldsymbol{k}_1\cdot\boldsymbol{r}}P_{\boldsymbol{\epsilon}_1}\right\rangle_{fi}\int_0^t dt_1 e^{i(E_{fi}-\omega_1+\omega_2)t_1} \tag{5.4a}$$

$$U_{fi}^{A\cdot P_I} = -iA_{0,1}A_{0,2}\left\langle e^{i\boldsymbol{k}_1\cdot\boldsymbol{r}}P_{\boldsymbol{\epsilon}_1}G(E_i-\omega_2)e^{-i\boldsymbol{k}_2\cdot\boldsymbol{r}}P_{\boldsymbol{\epsilon}_2}\right\rangle_{fi}\int_0^t dt_1 e^{i(E_{fi}-\omega_1+\omega_2)t_1} \tag{5.4b}$$

and

$$U_{fi}^{A^2} = -iA_{0,1}A_{0,2}\left\langle e^{i(\boldsymbol{k}_1-\boldsymbol{k}_2)\cdot\boldsymbol{r}}(\boldsymbol{\epsilon}_1\cdot\boldsymbol{\epsilon}_2)\right\rangle_{fi}\int_0^t dt_1 e^{i(E_{fi}-\omega_1+\omega_2)t_1} \tag{5.5}$$

where $A_{0,1}$ and $A_{0,2}$ are the amplitudes of the two fields. In the previous expressions we have made use the compact notation $P_{\boldsymbol{\epsilon}_n}\equiv\boldsymbol{\epsilon}_n\cdot\boldsymbol{P}$ and have introduced the Green

operators:

$$G^+(E+\omega) = \lim_{\varepsilon\to 0^+} G(E+\omega+i\varepsilon) = \lim_{\varepsilon\to 0^+} \sum\!\!\!\!\!\!\int_m \frac{|\Psi_m\rangle\langle\Psi_m|}{E+\omega-E_m+i\varepsilon} \tag{5.6a}$$

$$G(E-\omega) = \sum\!\!\!\!\!\!\int_m \frac{|\Psi_m\rangle\langle\Psi_m|}{E-\omega-E_m}. \tag{5.6b}$$

Following formal collision theory, in the transition amplitude corresponding to the direct path, we have introduced the advanced Green operator $G^+(E_i+\omega_1)$ to avoid the divergence associated with situations when a continuum state is resonant with the ground state by the absorption of ω_1. To calculate the limit, we make use of the Sokhatsky–Weierstrass theorem, which results in this expression for the advanced Green operator:

$$\begin{aligned} G^+(E+\omega) &= \lim_{\varepsilon\to 0^+} \sum\!\!\!\!\!\!\int_m \frac{|\Psi_m\rangle\langle\Psi_m|}{E+\omega-E_m+i\varepsilon} dm \\ &= \mathcal{P}\sum\!\!\!\!\!\!\int_m \frac{|\Psi_m\rangle\langle\Psi_m|}{E+\omega-E_m} dm - \pi i |\Psi_m\rangle\langle\Psi_m|\,\delta(E+\omega-E_m). \end{aligned} \tag{5.7}$$

For the case of bound resonant states the usual approach is to introduce the width Γ_m of the excited bound state Ψ_m due to its finite lifetime by making $E_i \to E_i + i\frac{\Gamma_r}{2}$ [98]. The transition amplitudes corresponding to the inverse path do not diverge for processes where the molecule is initially in the ground state. This is because the denominator of $G(E_i-\omega_2)$ will never be zero as that would mean that there is an intermediate state with lower energy than the ground state.

The evaluation of matrix elements containing $e^{i(\boldsymbol{k}-\boldsymbol{k}')\cdot\boldsymbol{r}}$ and $e^{i\boldsymbol{k}\cdot\boldsymbol{r}}P_e$ can be computationally expensive even for the simplest systems, and may become prohibitive for more complex systems such as molecules. Following an analogous procedure as in section 2.1.3, we expand $e^{i\boldsymbol{k}\cdot\boldsymbol{r}}$ in Taylor series and keep only the first two terms.

$$e^{i\boldsymbol{k}\cdot\boldsymbol{r}} \approx 1 + i\boldsymbol{k}\cdot\boldsymbol{r} - \frac{1}{2!}(\boldsymbol{k}\cdot\boldsymbol{r})^2 + \ldots \tag{5.8}$$

As it has already been mentioned, by taking only the first term of the expansion, we are adopting the usual dipole approximation, which is justified for low photon energies or long wavelengths. In this regime, it is easy to see that the matrix element associated with $\boldsymbol{A}^2$ vanishes[1] and the only contribution to SRS (or SCS) comes from $\boldsymbol{A}\cdot\boldsymbol{P}$ in second order. At higher energies, retardation effects need to be included by taking higher-order terms of the expansion, this results in a non-zero contribution of the diamagnetic term $\boldsymbol{A}^2$ for SRS processes. This last term was found to be the dominant contribution in SRS (and SCS) for photon energies in the keV regime [99]. In this thesis, we have adopted the same hybrid approach as Bachau *et. al.* [25] in which the $\boldsymbol{A}\cdot\boldsymbol{P}$ contribution is treated in the context of dipole approximation, by taking the zeroth-order term of the expansion, and retardation effects are included only in the $\boldsymbol{A}^2$ term with the inclusion of the first-order term $i\boldsymbol{k}\cdot\boldsymbol{r}$. Since $|\boldsymbol{k}| = \omega/c$, this is consistent with the fact that only terms up to $\mathcal{O}(1/c)$ are introduced. The final

[1] In dipole approximation the only contribution of this term comes from the elastic scattering of photons, whose treatment is not on the scope of this thesis.

expressions for the different terms of the KHW matrix elements are the following:

$$M_{fi}^{A\cdot P_D} = \lim_{\varepsilon\to 0^+} \sum\!\!\!\!\!\!\int_m \frac{\langle \Psi_f|\boldsymbol{\epsilon}_2\cdot\boldsymbol{P}|\Psi_m\rangle\langle\Psi_m|\boldsymbol{\epsilon}_1\cdot\boldsymbol{P}|\Psi_i\rangle}{E_m - E_i - \omega_1 + i\varepsilon} \tag{5.9a}$$

$$M_{fi}^{A\cdot P_I} = \sum\!\!\!\!\!\!\int_m \frac{\langle \Psi_f|\boldsymbol{\epsilon}_1\cdot\boldsymbol{P}|\Psi_m\rangle\langle\Psi_m|\boldsymbol{\epsilon}_2\cdot\boldsymbol{P}|\Psi_i\rangle}{E_m - E_i + \omega_2} \tag{5.9b}$$

$$M_{fi}^{A^2} = -i\alpha\langle\Psi_f|(\omega_1\boldsymbol{n_1} - \omega_2\boldsymbol{n_2})\cdot\boldsymbol{r}|\Psi_i\rangle(\boldsymbol{\epsilon_1}\cdot\boldsymbol{\epsilon_2}), \tag{5.9c}$$

where $\boldsymbol{n}_1$ and $\boldsymbol{n}_1$ are the propagation directions of the two fields related to the wave vector by $\boldsymbol{k} = \frac{\omega}{c}\boldsymbol{n}$. These matrix elements are in turn related to the final time-dependent transition amplitudes by

$$\begin{aligned} U_{fi}^{KHW} &= M_{fi}^{KHW} A_{0,1}A_{0,2} i \int_0^t dt_1 e^{i(E_f - E_i - \omega_1 + \omega_2)t_1} \\ &= \left[M_{fi}^{A\cdot P_D} + M_{fi}^{A\cdot P_I} + M_{fi}^{A^2}\right] A_{0,1}A_{0,2} i \int_0^t dt_1 e^{i(E_f - E_i - \omega_1 + \omega_2)t_1}. \end{aligned} \tag{5.10}$$

By squaring this transition amplitude, we obtain a time-dependent probability, which can be used to calculate the time-independent transition rate and the cross-section. This procedure was introduced in Chapter 3 and will be further detailed later. The previous expressions already give information on the different mechanisms that participate in SRS. The dipole terms imply a second-order process mediated by the polarization vectors of the fields $\boldsymbol{\epsilon_1}, \boldsymbol{\epsilon_2}$. On the other hand, the non-dipole term is a concurrent process dependent on the propagation directions of the fields $\boldsymbol{n}_1$ and $\boldsymbol{n}_2$.

5.2 Convergence of intermediate states

By introducing the Green operator in the $\boldsymbol{A}\cdot\boldsymbol{P}$ second-order matrix elements, we see the appearance of matrix elements representing dipole one-photon transitions between the initial or final states and the complete set of intermediate states ($\langle\Psi_f|\boldsymbol{\epsilon}_1\cdot\boldsymbol{P}|\Psi_m\rangle$ or $\langle\Psi_m|\boldsymbol{\epsilon}_2\cdot\boldsymbol{P}|\Psi_i\rangle$). The vast majority of the intermediate states that play a significant role in the Raman transitions we are interested in belong to the electronic continuum. This fact presents two main problems when performing actual SRS (or SCS) calculations using X-ray photons. The first issue comes from the difficulty to obtain a proper representation of continuum states, albeit the high oscillatory behavior of the wave function at the energies studied. The second issue is related to the number of intermediate states to include in the calculation. To achieve convergence of the matrix elements, one has to balance the need to incorporate all the relevant states associated with the process while keeping the calculation computationally feasible. At the energies achieved by the electron after absorption of ω_1, all ionization thresholds of H_2 are energetically opened. Moreover, higher partial waves that do not contribute for transitions at lower photon energies may start to do so significantly increasing the number of ionization channels. To obtain a proper set of intermediate states we performed several convergence tests based on calculating the one-photon photoionization cross-section. We assumed radiation with polarization parallel to the internuclear axis in our tests, so we focused on transitions from bound states of symmetry $^1\Sigma_g^+$ to continuum states of symmetry $^1\Sigma_u^+$, and compared

results obtained from length and velocity gauge calculations[2]. The corresponding one-photon cross-sections, expressed in atomic units, read as follows:

$$\frac{d\sigma_V^{(1)}}{d\Omega} = \frac{4\pi^2}{\omega c}\sum_{\alpha,\ell_\alpha}|\langle\psi^{\varepsilon_\alpha}_{\alpha,\ell_\alpha}|P_z|\psi_i\rangle|^2 \tag{5.11a}$$

$$\frac{d\sigma_L^{(1)}}{d\Omega} = \frac{4\pi^2\omega}{c}\sum_{\alpha,\ell_\alpha}|\langle\psi^{\varepsilon_\alpha}_{\alpha,\ell_\alpha}|z|\psi_i\rangle|^2 \tag{5.11b}$$

where ω is the photon energy equal to the energy difference between the continuum and the initial states ($\omega = \varepsilon_\alpha - E_i$). The determination of the bound and continuum wave functions, ψ_i and $\psi^{\varepsilon_\alpha}_{\alpha,\ell_\alpha}$ respectively, was detailed in Chapter 1, and the calculation of the corresponding position and momentum operator matrix elements was described in Chapter 3.

To obtain an accurate representation of continuum states, we tested several parameters involved in the calculation of the one-electron orbitals as well as the two-electron uncoupled continuum states (UCSs). We present the results of our convergence test for three different parameters, the number of B-splines (N_B) and angular momenta (ℓ_{max}) in the expansion of the mono-electronic orbitals, and the number of points (NPI) used in the numerical calculation of the bi-electronic integrals from equation 1.25. These parameters were chosen on the basis of their influence in the description of the high oscillatory behavior of the wave function at high energies. The different sets of B-splines tested were all of order 8 and built in a radial box of r_{max}=60 a.u.. For the two-electron wave functions, we used 700 configurations for the bound states and 280 configurations for the UCSs. The spectrum of our discretized UCSs consists of a grid with 244 energy values that reproduce the density of states of a particle in a box of size r_{max} which can be derivad from equation 1.38.

$$\rho(E) = \frac{1}{\pi\sqrt{2}}\frac{r_{max}}{\sqrt{E}} \tag{5.12}$$

With this energy grid, we are able to reproduce the continuum wave function of an electron with up to 80 a.u. of kinetic energy. This energy limit is more than enough to study SCS and SRS with X-ray pulses ranging between 20 and 60 a.u. of photon energy. For this first set of convergence tests, we included only the first ionization threshold (the H_2^+ ion is left in the $1s\sigma_g$ state) and partial waves up to $\ell = 7$ in our multichannel expansion. Convergence analysis of the multichannel character of the wave function was also performed, and the results will be shown later.

Figure 5.1 shows the one-photon cross-sections comparing results from calculations using 280 and 340 B-splines. In this first test we set ℓ_{max}=16 and NPI=1001. As we expected from a calculation with this number of angular momenta, convergence between length and velocity gauge results is not achieved, especially at high energies and for ionization from an excited state. Nonetheless, the sharp oscillations in the cross-section suggest room for improvement in the description of continuum states aside from the angular expansion. However, this improvement seems not to be related to the number of B-splines used as there are no significant variations for both

[2]To obtain the cross-section for a length gauge calculation we simply make use of the well-known relation between length and velocity gauge dipole matrix elements

$$\langle\Psi_f|\boldsymbol{r}|\Psi_i\rangle = \frac{-i}{E_f - E_i}\langle\Psi_f|\boldsymbol{P}|\Psi_i\rangle$$

calculations. Another test with N_B=280, NPI=1001 and ℓ_{max}=20 was performed, but no significant difference with the results shown in Figure 5.1 was found. The negligible change in the results supports the idea that convergence in the length gauge at high energies is very slow and may require enormous expansions with up to 100 angular momenta [68]. Further investigation on the description of excited states might also be needed given the large deviations between the velocity gauge and length gauge results for the 2nd and 3rd excited states.

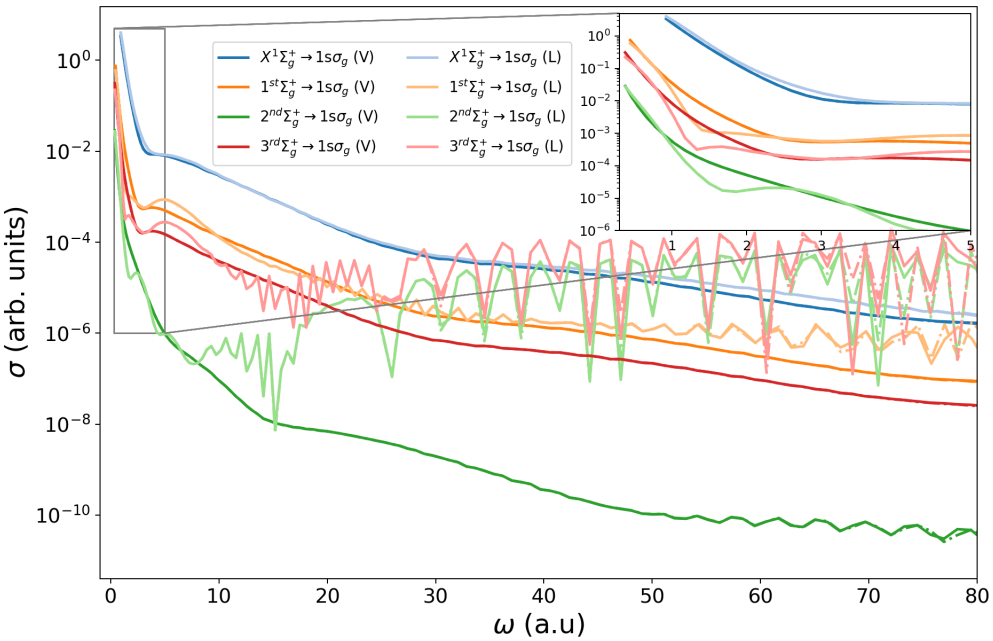

FIGURE 5.1 – Partial photoionization cross-section to the $^1\Sigma_u^+(1s\sigma_g)$ continuum from the ground state and the first three excited states of symmetry $^1\Sigma_g^+$ of H_2 as a function of photon energy. The dark colors represent results from calculations in velocity gauge (labeled with V), while the corresponding light colors do so for calculations in length gauge (labeled with L). Results from calculations using 280 (solid line), 340 (dashed-dotted line) B-splines are shown.

The rapid oscillations of the continuum wave function at high energies also affect the correct description of electron-electron repulsion. The Z^k method [41], used in the calculation of the matrix elements of the $1/r_{12}$ operator shown in equation 1.25, is very sensitive to the number of points used in the numerical calculation of the two-electron radial integrals at high energies. Figure 5.2 shows results for calculations with N_B=280, ℓ_{max}=16 and comparing several values of NPI. The results show that using 3003 points to solve the bi-electronic integrals erases the sharp oscillations in the length gauge cross-section. Although this does not fix the significant difference between the length and velocity gauge results, the disappearance of the sharp oscillations implies that the quality of the continuum wave functions has significantly improved. At this point, we decided to focus on the velocity gauge results, which we deemed to be converged with N_B=280, ℓ_{max}=16 and NPI=3003.

The multichannel description of the continuum wave function affects our two main concerns regarding the set of intermediate states needed in the calculation of the second-order transition amplitudes. For once, it is important to know which are the most relevant ionization channels, given that we cannot include them all. The second is related to the multichannel description of each ionization channel, *i.e.* the

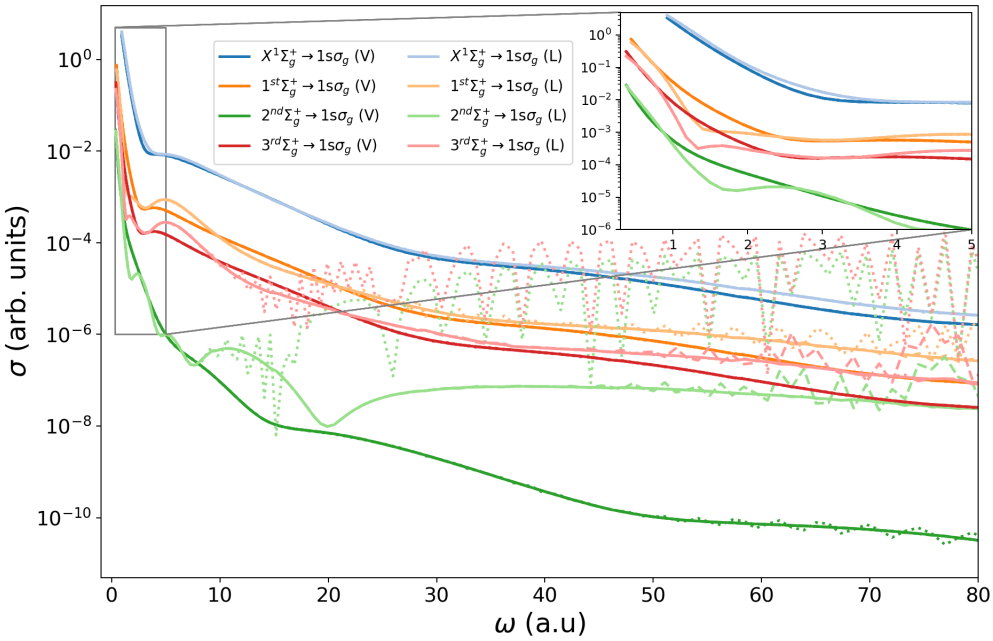

FIGURE 5.2 – Partial photoionization cross-section to the ${}^1\Sigma_u^+(1s\sigma_g)$ continuum from the ground state and the first three excited states of symmetry ${}^1\Sigma_g^+$ of H_2 as a function of photon energy. The dark colors represent results from calculations in velocity gauge (labeled with V), while the corresponding light colors do so for calculations in length gauge (labeled with L). Results from calculations using 1001 (dotted line), 2002 (dashed line), and 3003 (solid line) points to solve the bi-electronic integrals from equation 1.25 are shown.

number of channels μ' we include in the Lippmann-Schwinger equation, shown in equation 1.57, to obtain the wave function corresponding to a specific channel μ. In figure 5.3 we show the contribution from the first 6 partial waves to the one-photon cross-section from the ground state to the ${}^1\Sigma_u^+(1s\sigma_g)$ continuum. To study processes involving photon energies between 20 and 60 a.u., including only partial waves up to $\ell = 7$ is sufficient as these contribute the most in this energy region.

The inclusion of additional ionization thresholds needs to be addressed two-fold. First by looking at their relevance as intermediate states, and second by examining their role in the multichannel description of other channels. In Figure 5.4 we show the one-photon cross-section from the ground state and the first excited state to the ${}^1\Sigma_u^+(1s\sigma_g)$ and ${}^1\Sigma_u^+(2p\sigma_u)$ continua. We also plot the results from a calculation in which we included the effect of the $2p\sigma_u$ ionization channel in the multichannel description of the ${}^1\Sigma_u^+(1s\sigma_g)$ continuum. With a difference of two orders of magnitude between the ${}^1\Sigma_u^+(1s\sigma_g)$ and ${}^1\Sigma_u^+(2p\sigma_u)$ cross-sections, it is safe to assume that continuum states associated with the second ionization threshold do not play a significant role as intermediate states in Raman transitions. The effect of this threshold as a perturbation to the ${}^1\Sigma_u^+(1s\sigma_g)$ cross-section at high photon energies can also be neglected. We performed additional tests where H_2^+ could be left in the second and fourth excited ionic states $2p\pi_u$ and $2s\sigma_g$, which we have not included here for clarity, and arrived to the same conclusions. We thus decided to include as intermediate states in the calculation of the second-order dipole matrix elements continuum states associated only with the first ionization threshold $1s\sigma_g$ with partial waves up to $\ell = 7$.

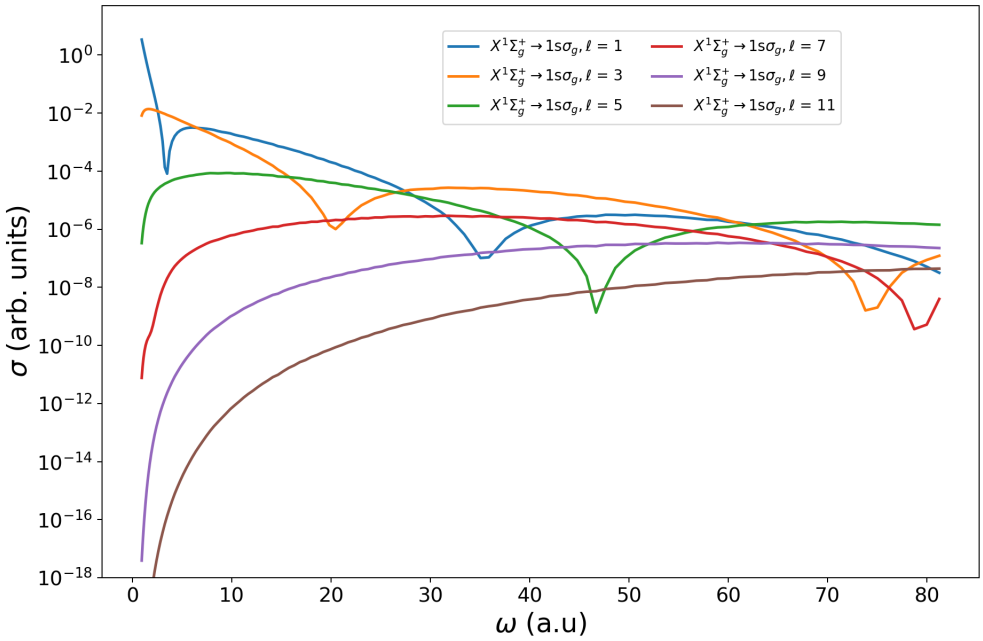

FIGURE 5.3 – Contribution from the first six partial waves to the partial photoionization cross-section to the ${}^1\Sigma_u^+(1s\sigma_g)$ continuum from the ground state of H_2 as a function of photon energy.

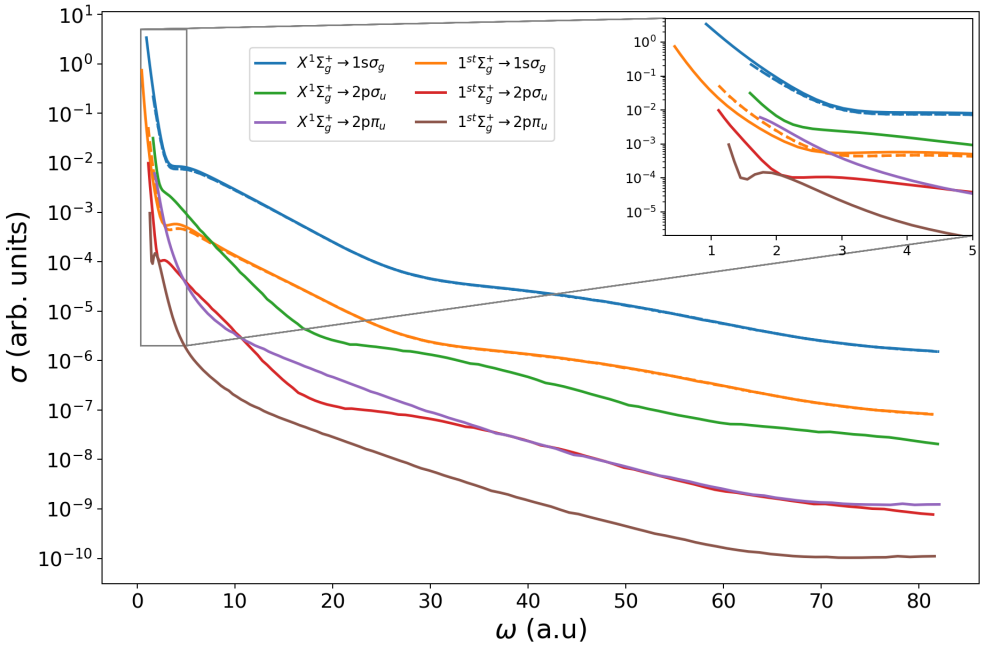

FIGURE 5.4 – Partial photoionization cross-sections to the ${}^1\Sigma_u^+(1s\sigma_g)$ and ${}^1\Sigma_u^+(2p\sigma_g)$ continua from the ground state and the first excited state of symmetry ${}^1\Sigma_g^+$ of H_2 as a function of photon energy. The dashed line represents results from calculations in which $2p\sigma_u$ has been included in the multichannel description of the ${}^1\Sigma_u^+(1s\sigma_g)$ continuum.

To our knowledge, nobody has attempted to calculate nor has measured the one-photon cross-section of H_2 at such high energies. Reference [100] shows the total

calculated cross-section up to 20 a.u. with a comparison with experimental results up to 4 a.u. from [101]. In their publication, Fojón *et al.* also calculated the contribution from the continuum with ${}^1\Sigma_u^+$ final symmetry, which agrees with our results.

Although we have established the convergence of the set of intermediate states from a perturbative perspective, the same conclusions apply for non-perturbative calculations. The relation between the interaction operator $\mathcal{V}_{DA}^{(1)}$, seen equation 2.34, and $\boldsymbol{A}\cdot\boldsymbol{P}$ makes it possible to use the same matrix elements for the calculation of the KHW Raman cross-section and for the study of SRS with ultrashort pulses as we will see later. In the case of Compton scattering, more thorough testing needs to be done regarding the number of thresholds to include for both dipole and non-dipole transitions. Because SCS leads to ionization, different thresholds might play a role not as intermediate states but as final states. With our current method to calculate electronic continuum states, the convergence of continuum-continuum couplings, necessary for the dipole contribution to SCS, cannot be achieved in perturbative calculations, and a direct resolution of the TDSE is needed instead. This issue will be dealt with in the next chapter.

5.3 The Raman cross-section

We define the differential cross-section as:

$$\frac{d\sigma}{d\Omega} = \frac{\Gamma_{d\Omega}}{F}. \tag{5.13}$$

where F is the incident photon flux and $\Gamma_{d\Omega}$ is the transition rate differential in solid angle. As we mentioned in Chapter 3, when the final state of a given transition has a continuous spectrum, the corresponding probabilities have to be integrated over a certain domain and the density of final states needs to be included. Although, in Raman scattering the final state of the molecule is a discrete bound state, the states of the scattered photon form a continuous spectrum. By calculating the limit for an infinite pulse duration we can obtain transition rates, which are time-independent, from transition probabilities obtained from TDPT as:

$$\begin{aligned}\Gamma_{d\Omega}^{(KHW)} &= \lim_{t\to\infty}\int \frac{dP_{i\to f}^{(KHW)}}{dt}\rho_{d\Omega}(\omega_2)d\omega_2 \\ &= \int d\omega_2\rho_{d\Omega}(\omega_2)\left|M_{fi}^{KHW}\right|^2 \lim_{t\to\infty}\frac{d}{dt}\left|A_{0,1}A_{0,2}\int_0^t dt_1 e^{i(E_f-E_i-\omega_1+\omega_2)t_1}\right|^2,\end{aligned} \tag{5.14}$$

where $\rho_{d\Omega}(\omega_2)$ is the density of scattered photons per unit solid angle. Finally, by substituting the density of states and the photon flux of a monochromatic a plane wave[3] and using the following property

$$\left|\int_0^t dt_1 e^{-\omega t_1}\right|^2 \underset{t\to\infty}{\sim} 2\pi t\delta(\omega) \tag{5.15}$$

we obtain the final expression for the Raman cross-section including retardation effects.

$$\frac{d\sigma^{KHW}}{d\Omega} = \alpha^4\frac{\omega_2}{\omega_1}\left|M_{fi}^{A\cdot P_D} + M_{fi}^{A\cdot P_I} + M_{fi}^{A^2}\right|^2 \tag{5.16}$$

[3]Defined as $\rho_{d\Omega}(\omega) = \frac{\omega}{(2\pi A_0)^2 c^3}d\Omega$ and $F = \frac{\omega c A_0^2}{2\pi}$ respectively.

Because of the appearance of $\delta(E_f - E_i - \omega_1 + \omega_2)$, which enforces energy conservation, the energy of the scattered photon is fixed to $\omega_2 = \omega_1 - (E_f - E_i)$. Nonetheless we leave it as ω_2 for convenience.

To discuss the relative importance of the dipole and non-dipole contributions to Raman scattering, we calculated the cross-section associated with $\boldsymbol{A} \cdot \boldsymbol{P}$ for the case where the incident and scattered fields have the same polarization parallel to the internuclear axis. In our calculation, we neglected the width of the resonant intermediate bound states since their contribution appears for lower photon energies. We show the results in Figure 5.5 for the total $\boldsymbol{A} \cdot \boldsymbol{P}$ contribution and from its direct and inverse path components. The origin of the partial cancellation of the dipole contribution to Raman scattering becomes now evident. The cross-sections for the direct and inverse paths tend to become equal for larger photon energies. However, their corresponding matrix elements have opposite signs and end up canceling each other. On the other hand, the contribution from $\boldsymbol{A}^2$ to the Raman cross-section is almost constant as it is associated with a single matrix element and $\omega_2/\omega_1 \approx 1$ for larger incident photon energies. A comparison between the dipole and non-dipole contribution to the Raman cross-section is difficult as, in the context of our approximation, both mechanisms populate bound states of different symmetries. This comparison will be shown at the end of the next section.

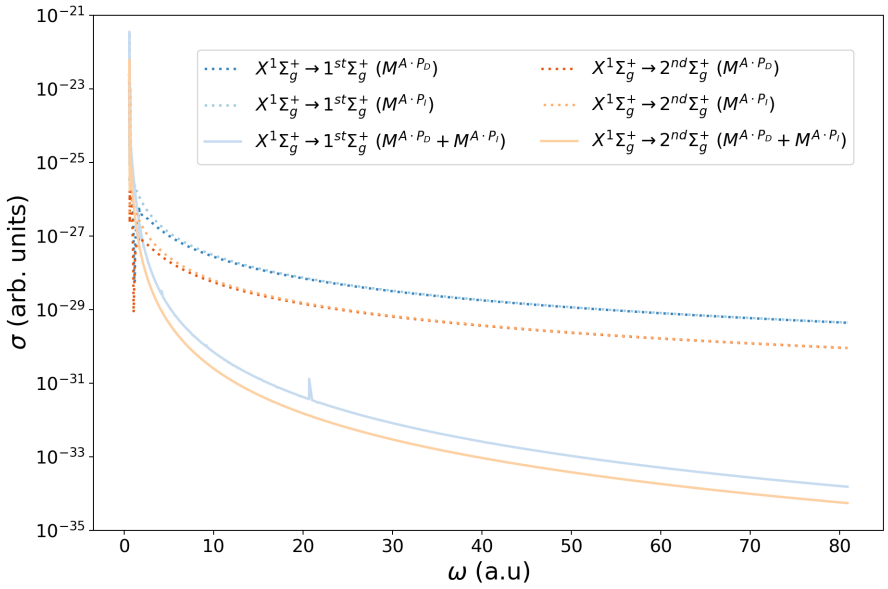

FIGURE 5.5 – Contribution from $\boldsymbol{A} \cdot \boldsymbol{P}$ (solid line) and its direct and inverse components (dotted lines), to the Raman cross-section from the ground state to the first and second excited states of H_2 as a function of the incident photon energy ($\omega \equiv \omega_1$).

5.4 Stimulated Raman scattering with ultrashort pulses

In this section, we present the first SRS calculations in H_2 using ultrashort attosecond pulses. Because of the large bandwidth of the pulse, the case of an ultrashort pulse is parallel to the study of two color SRS with co-propagating fields. Our results are obtained from both perturbative and non-perturbative calculations. We recall the Hamiltonian from equation 2.32 developed for the interaction between the molecule

and an electromagnetic field including retardation effects.

$$\mathcal{H} = \mathcal{H}_0 + \mathcal{V}_{DA}^{(1)} + \mathcal{V}_{RET}^{(2)} \tag{5.17}$$

The first term of the previous equation corresponds to the field-free molecular Hamiltonian from equation 1.3, and the last two correspond to the dipole interaction term, which originates from $\boldsymbol{A} \cdot \boldsymbol{P}$, and the approximation to $\boldsymbol{A}^2$, which introduces retardation effects of order $\mathcal{O}(1/c)$. Explicit expressions to these terms can be found in equation 2.34 at the end of Chapter 2. We have neglected the term $\mathcal{V}_{RET}^{(1)}$, appearing in 2.34b, which also introduces retardation effects of order $\mathcal{O}(1/c)$, as it related to one-photon processes [102] and previous studies have found that this term does not contribute to SRS [97].

We study the interaction between H_2 and a Gaussian-shaped pulse with FWHM of 68 attoseconds (2.8 a.u.) and a peak intensity of 10^{18} W/cm^2 with a central frequency $\omega = 544$ eV (20 a.u.). With a FWHM for the spectral bandwidth of 55 eV (2 a.u.), the laser bandwidth covers all the electronic states of H_2 energetically allowing SRS processes. Even with the high intensity considered here, the Keldysh parameter is still much greater than one due to the high photon energy, justifying the perturbative treatment. For the pulse duration investigated here, we can neglect the effects of both autoionization and nuclear motion as these processes have characteristic times of a few femtoseconds. The final expression for the two-electron interaction Hamiltonian from equation 5.17 for the case of a laser field with polarization along z (parallel to the internuclear axis) and propagation along x results in:

$$\mathcal{H} = \mathcal{H}_{el} + A(t)\sum_i P_{z_i} + \frac{1}{c}A(t)E(t)\sum_i x_i, \tag{5.18}$$

where the electronic Hamiltonian $\mathcal{H}_{el}$ considers fixed nuclei at the equilibrium internuclear distance ($R_{eq} = 1.4$ a.u.).

For the non-perturbative treatment we follow the methodology developed in Chapter 3, the TDFCC method. The perturbative approach relies on time-dependent perturbation theory applied to the above Hamiltonian. Similarly as with the KHW raman cross-section, we treat $\mathcal{V}_{DA}^{(1)}$ in second order and $\mathcal{V}_{RET}^{(2)}$ in first order perturbation theory. This results in the following expressions for the transition amplitudes:

$$\begin{aligned} U_{fi}^{A\cdot P} = (-i)^2 \sum_m \langle\psi_f|P_z|\psi_m\rangle\langle\psi_m|P_z|\psi_i\rangle \\ \times \int_{-T}^{T} dt_1 A(t_1) e^{iE_{fm}t_1} \int_{-T}^{t_1} dt_2 A(t_2) e^{iE_{mi}t_2} \end{aligned} \tag{5.19a}$$

$$U_{fi}^{A^2} = -i\alpha \int_{-T}^{T} dt A(t)E(t)e^{iE_{fi}t}\langle\psi_f|x|\psi_i\rangle \tag{5.19b}$$

where T is the integration time which is chosen long enough so that the vector potential amplitudes $A(T)$ and $A(-T)$ vanish. The same integration time was chosen for the propagation of the TDSE using an explicit time-adaptative Runge-Kutta method. For simplicity, we have replaced the integration over intermediate continuum states by a sum over Kronecker delta normalized states[4].

[4] By approximating the integration to a weighted sum, $\int dm \to \sum_m W_m$, we can simplify the density of states, defined in equation 1.39, by choosing the weights to be those of a Simpson quadrature scheme, $W_m = (E_{m+1} - E_{m-1})/2$.

In our implementation, both perturbative and non-perturbative calculations require the same matrix elements involving the position and momentum operators. The matrix elements associated with the momentum operator result from the $\boldsymbol{A}\cdot\boldsymbol{P}$ term and involve bound-bound and bound-continuum transitions between states of symmetry ${}^1\Sigma_g^+$ and ${}^1\Sigma_u^+$ on account of the selection rules derived from the P_z operator.

$$X^1\Sigma_g^+ \xrightarrow{P_z} {}^1\Sigma_u^+ \xrightarrow{P_z} {}^1\Sigma_g^+ \tag{5.20}$$

These matrix elements are the same ones we used for the calculation of the KHW Raman cross-section after a convergence study. For the case of the position operator matrix element, related to $\boldsymbol{A}^2$, we need to include bound-bound transitions between states of symmetry ${}^1\Sigma_g^+$ and ${}^1\Pi_u$. This term, although related to a two-photon process, is of order one in perturbation theory and does not involve any intermediate state. The different operator also implies different selection rules, in this case, associated with the operator x.

$$X^1\Sigma_g^+ \xrightarrow{x} {}^1\Pi_u \tag{5.21}$$

As a result of the contribution of both $\mathcal{V}_{DA}^{(1)}$ and $\mathcal{V}_{RET}^{(2)}$ to SRS, states of different symmetry get populated depending on which is the dominant term. This fact has important consequences when both terms can populate states with the same energy as we will show in the next chapter when studying SCS.

5.4.1 Dipole contribution to SRS

As seen in equation 5.19a, the expression for the dipole contribution to SRS involves the calculation of a double integral in time at each intermediate state in the perturbative treatment. Larger integration times and basis sets can dramatically scale the computational time, erasing the advantages of perturbative calculation over a direct resolution of the TDSE altogether. For this reason, following the work of Dondera *et al.* [97], we propose a single integral over frequencies scheme by making use of the inverse Fourier transform of the pulse in the frequency domain.

$$A(t) = \frac{1}{\sqrt{2\pi}}\int_{-\infty}^{+\infty} d\omega \tilde{A}(\omega) e^{i\omega t} \tag{5.22}$$

which leads to

$$U_{fi}^{A\cdot P_\omega} = i\int_{-\infty}^{+\infty} d\omega \tilde{A}(\omega)\tilde{A}(E_i - E_f - \omega)\sum_m \frac{\langle\psi_f|P_z|\psi_m\rangle\langle\psi_m|P_z|\psi_i\rangle}{E_m - E_i - \omega}. \tag{5.23}$$

This expression contains the familiar matrix elements $M_{fi}^{A\cdot P}$ from the $\boldsymbol{A}\cdot\boldsymbol{P}$ contribution to the KHW Raman cross-section where the integration over continuum states has been discretized, and the Dirac delta associated with the resonant term has been neglected. We also neglect the contribution of resonant bound states based on the high photon energies considered here. Results obtained from this new form for the transition amplitudes fail to reproduce those obtained from equation 5.19a, as seen in figure 5.6, because of the behaviour near resonance ($E_m - E_i - \omega \sim 0$). This issue is common in perturbative multiphoton calculations using discrete basis sets and has been treated with different schemes over the years. Here we present two different approaches.

In the first one, we suppose that intermediate states high in the continuum do not play a significant role in Raman transitions given the low cross-section for one-photon absorption of high energy photons we previously saw (figures 5.1, 5.2, 5.3, 5.4). The two-photon process is then primarily due to transitions through intermediate bound states or continuum states closer to the threshold. For these states, the energy difference with the ground state is much less than the photon energy $E_m - E_i \ll \omega$, and we can rewrite the expression for the transition amplitude as:

$$U_{fi}^{A\cdot P_\omega} \approx -i \int_{0^+}^{+\infty} d\omega \left[\tilde{A}(\omega)\tilde{A}(E_i - E_f - \omega) - \tilde{A}(-\omega)\tilde{A}(E_i - E_f + \omega)\right] \times \sum_m \frac{\langle \psi_f | P_z | \psi_m \rangle \langle \psi_m | P_z | \psi_i \rangle}{\omega}. \quad (5.24)$$

With this new expression, the singularity appearing for $E_m - E_i - \omega = 0$ has been removed, and we have also eliminated the new singularity at the origin by recasting the integral. As seen in figure 5.6, results obtained from this approach do not agree with those obtained from equation 5.19a. Nonetheless, we observe a significant improvement with respect to the results directly obtained from equation 5.23. This indicates that, although the singularities of $M_{fi}^{A\cdot P}$ are responsible to a large extent for the disagreement between the time-integration and the frequency-integration schemes, the high energy continuum states do play an important role in the outcome of SRS. This fact can be understood due to the interference between direct and indirect amplitudes, as defined by 5.9, where the subtraction of comparable amplitude becomes tedious from the numerical point of view.

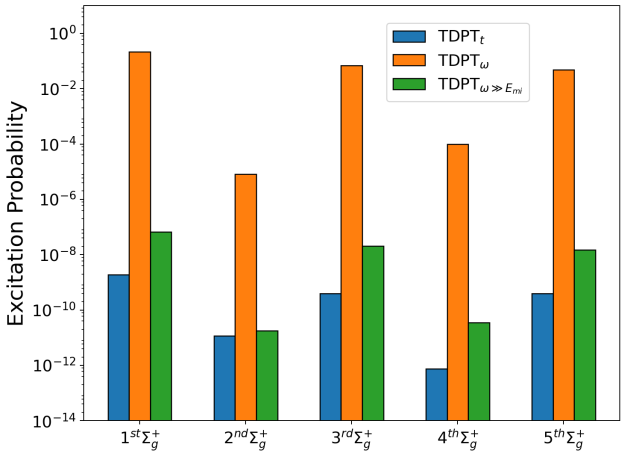

FIGURE 5.6 – Excitation probability from the ground state to the first five excited states of H_2 for a SRS calculation. The results were obtained from TDPT calculations using equations 5.19 (blue), 5.23 (orange) and 5.24 (green).

The other method was developed in [103] for the calculation of N-photon transition amplitudes using discrete basis sets. This method proposes an extrapolation scheme to calculate $M_{fi}^{A\cdot P}$ instead of using the Sokhatsky–Weierstrass theorem, shown

in equation 5.7. We define the transition amplitudes as a function of ε by:

$$U_{fi}^{A\cdot P}(\varepsilon) = i\int_{-\infty}^{+\infty} d\omega \tilde{A}(\omega)\tilde{A}(E_i - E_f - \omega)\sum_m \frac{\langle\psi_f|P_z|\psi_m\rangle\langle\psi_m|P_z|\psi_i\rangle}{E_m - E_i - \omega + i\varepsilon}. \tag{5.25}$$

As a result of our discretization of continuum states, transitions through intermediate states of this type resemble multiphoton processes through resonant states. If this were the case, we would have to take into account their respective widths and energy shifts. In our case, given that these states are not truly bound, we assign an artificial width and perform the calculation of the transition amplitude for ε approaching zero. Figure 5.7 shows results for the real and imaginary part of the transition amplitudes for several values of ε. The results show that, near the origin, the amplitude diverges. Before that point, the dependence of the amplitude with ε behaves smoothly, and extrapolation can be used to calculate the value for $\varepsilon = 0$. Figure 5.8 shows the results for the excitation probability of Raman transitions to different excited states obtained from this frequency-integration scheme using extrapolation. The results are compared against the original time-integration scheme from equation 5.19a and to results obtained from solving the TDSE including only the dipole interaction term $\mathcal{V}_{DA}^{(1)}$. The results from both perturbative approaches agree between each other and with the results obtained from solving the TDSE. We thus confirm the validity of the perturbative treatment of SRS in dipole approximation.

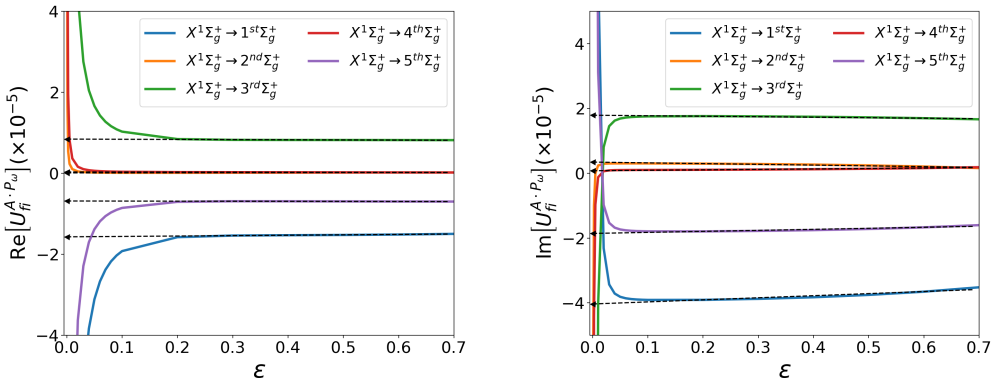

FIGURE 5.7 – Real and imaginary parts of the transition amplitude as a function of ε (solid lines) from a SRS calculation using equation 5.25. The dashed arrow points to the extrapolated value for $\varepsilon \to 0$.

5.4.2 Non-dipole contribution to SRS

The case of the non-dipole contribution to SRS is much simpler since it requires a single matrix element as seen in equation 5.19b. In a similar as with the dipole case, by employing the Fourier transform of the pulse, we obtain an alternative formulation based on a frequency-integration scheme.

$$U_{fi}^{A^2} = -\alpha\int_{-\infty}^{+\infty} d\omega \tilde{A}(\omega)\tilde{A}(E_i - \omega - E_f)(E_i - E_f - \omega)\langle\psi_f|x|\psi_i\rangle \tag{5.26}$$

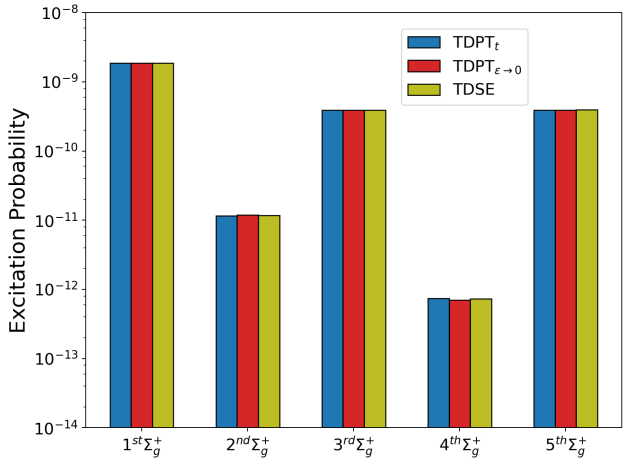

FIGURE 5.8 – Excitation probability from the ground state to the first five excited states of H_2 for a SRS calculation. The results were obtained from TDPT calculations using equation 5.19 (blue) and the extrapolated result from equation 5.25 (orange), and from the resolution of the TDSE (olive).

where we have used the Fourier transform of the electrcic field[5]. In figure 5.9 we show the result for SRS perturbative and non-perturbative calculations for both dipole and non-dipole contributions. The excitation probability is calculated as the sum of the excitation probabilities to the first five bound excited states of each symmetry $^1\Sigma_g^+$ and $^1\Pi_u$. We present a comparison between perturbative and non-perturbative calculations using several schemes developed in this chapter. The non-perturbative results were obtained by solving the TDSE including the $\mathcal{V}_{DA}^{(1)}$ or $\mathcal{V}_{RET}^{(2)}$ interaction terms from equation 2.34 in the Hamiltonian to obtain the dipole and non-dipole contributions respectively.

$$\mathcal{H}_{A\cdot P} = \mathcal{H}_{el} + A(t)\sum_i P_{z_i} \tag{5.27a}$$

$$\mathcal{H}_{A^2} = \mathcal{H}_{el} + \frac{1}{c}A(t)E(t)\sum_i x_i \tag{5.27b}$$

The agreement between perturbative and non-perturbative calculations extends to the non-dipole contribution and validates the use of perturbation theory as a proper tool to study retardation effects in SRS. We also solved the TDSE for several laser intensities and observed a quadratic dependence of the excitation probability for both contributions, thus confirming that SRS is a two-photon process.

For lower photon energies, the dipole contribution dominates, as expected, and we see a transition in the excitation mechanism between 10-20 a.u.. For energy frequencies larger than 20 a.u. non-dipole effects start to be the dominant process, and the difference between the dipole and non-dipole contribution grows with the

[5]To calculate the Fourier transform of the electric field we have used the following property use to calculate the Fourier transform of the derivative of a function

$$\mathcal{F}\left[\frac{d^n f(t)}{dt^n}\right](\omega) = (i\omega)^n \mathcal{F}[f(t)](\omega)$$

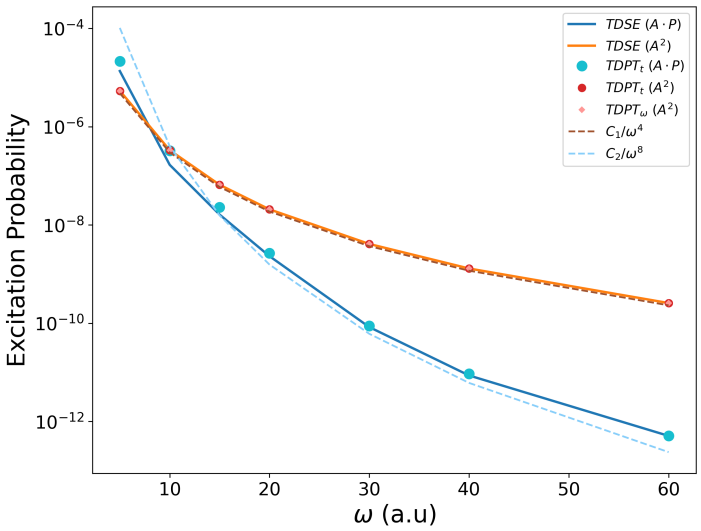

FIGURE 5.9 – Dipole ($\boldsymbol{A} \cdot \boldsymbol{P}$) and non-dipole ($\boldsymbol{A}^2$) contributions to the total excitation probability for a SRS calculation approximated by the sum over the contributions of the first five excited states. Comparison between results obtained from a direct resolution of the TDSE (solid lines) and TDPT calculations using equations 5.19 (blue circle), 5.19 (red circle) and 5.19 (pink circle). The excitation probabilities have been fitted with the power laws commented on the text.

photon energy. As a result of the presence of two different excitation mechanisms, bound states of different symmetries are populated. In the region of lower photon energies, bound states of ${}^1\Sigma_g^+$ symmetry are preferentially populated, whereas states of ${}^1\Pi_u$ symmetry do so for higher photon energies.

We noticed that the non-dipole and dipole excitation probabilities as a function of the photon energies could be fitted to two different power laws. Recalling the expressions from equation 5.10, the total KHW transition amplitude depends on the square of the amplitude of the vector potential. This amplitude scales with the photon energy as $1/\omega$, as shown in A.6, for a constant field intensity. The transition probability associated to the non-dipole contribution can then be fitted to C_1/ω^4 with C_1 constant since it can be shown that $M_{fi}^{A^2}$ does not depend on ω [97]. In the case of the dipole contribution, the partial cancellation of the direct and inverse paths, shown in equations 5.9a and 5.9b respectively, makes $M_{fi}^{A\cdot P} \propto 1/\omega^2$, so the total probability in this case can be fitted to a power law of C_2/ω^8 with C_2 constant. We have included this fitting in figure 5.9.

Chapter 6

Stimulated Compton scattering using ultrashort pulses

Compton scattering was discovered by Arthur Compton almost 100 years ago when studying the inelastic scattering of X-ray radiation in a carbon target [104]. Compton assumed a corpuscular nature of radiation and applied energy and momentum conservation to the collision between a photon and a free electron to explain the longer wavelength of the scattered field as a function of the scattering angle. The Compton effect gave the first proof of Einstein's postulations of the particle nature of electromagnetic waves. It also triggered the development of coincidence measurement techniques when Bothe and Geiger tried to clear doubts on energy conservation in Compton scattering [105]. Understanding of the Compton effect has important implications in radiobiology and is the basis for many techniques used to obtain information on the electron density of molecules and materials [106].

The theoretical description of Compton scattering of X-ray photons by bound electrons was done in the framework of the Impulse Approximation (IA). This approximation considers that the interaction time between a bound electron and an X-ray photon is so short that there is not enough time for the rest of the system to feel the interaction. The photon only interacts with a single electron, and the binding between the different constituents of the system is neglected, effectively treating the electron as quasi-free. The only information considered relative to the rest of the system is through the use of the ground state wave function as an initial momentum distribution. Although this approximation works well when the binding energy of the electron is negligible compared to the momentum $\boldsymbol{Q} = \boldsymbol{k}_1 - \boldsymbol{k}_2$ (where $\boldsymbol{k}_1$ and $\boldsymbol{k}_2$ are the wavevectors of the incident and scattered photons) transferred by the photon to the electron, limits to its applicability have been found. Theoretically, this approximation has long been questioned to explain the scattering of light by deeply bound electrons [107]. Experimentally, recent observations in atoms using FEL have stressed the need for more sophisticated theoretical methods [23].

Techniques based on the interaction of matter with ultrashort X-ray laser pulses can provide valuable information on the inner-shell dynamics of specific atoms in a molecule [24]. The analysis of the temporal evolution of electrons ejected in these kinds of processes can be used to retrieve valuable information on the events that produced them. For example, from the analysis of Auger electrons, one can access information on the decay of a core-hole [82]. In this sense, the analysis of electrons produced by Compton scattering of ultrashort X-ray laser pulses has promising perspectives for the study of ultrafast electron dynamics.

Similarly to SRS, stimulated Compton scattering (SCS) is a non-linear process where a first field induces the absorption of a photon with energy ω_1, and a second field overlapping in time stimulates the emission of a photon with energy ω_2 such that $\omega_1 > \omega_2$. The energy difference $\omega_1 - \omega_2$ is absorbed by the system and leads

to ionization. This phenomenon differs from that studied by Kapitza and Dirac for the particular case of the reflection of free electrons from standing light waves [108]. Observation of SCS using one-color ultrashort pulses is possible, provided that the bandwidth of the pulse is larger than the ionization potential. However, due to the small cross-section of SCS, only XFEL sources will be able to produce attosecond X-ray pulses with enough intensity to be able to observe these kinds of processes. Just like with SRS, due to the short wavelength of these pulses, theoretical approaches beyond the dipole approximation are needed.

In this chapter, we present results of SCS calculations in H_2 using one-color attosecond pulses beyond the impulse approximation and including retardation effects. We follow the same theoretical framework like the one used in the last chapter to study SRS with ultrashort pulses. By solving the TDSE with our TDFCC method, which was explained in Chapter 3, we are able to retrieve PES, integrated MFPADs, and differential in photoelectron energy MFPADs. Special attention is given to these last two, as the appearance of forward/backward asymmetries in the photoelectron angular distributions has been linked to the breakdown of the dipole approximation [28]. Compared to previous studies of this phenomenon performed in atoms [77], H_2 offers a richer perspective due to the presence of two centers and two-active electrons. The loss of spherical symmetry raises the problem of the effect of the relative orientation of the internuclear axis, field propagation direction, and polarization vector. Our study begins with a convergence analysis of the role of higher ionization thresholds in the multichannel description of the states involved in SCS.

6.1 Effect of additional ionization thresholds

In the previous chapter, we performed a convergence analysis on the set of intermediate states needed to calculate the dipole contribution to SRS. We did so by calculating one-photon cross-sections from the ground state to those intermediate states lying in the continuum part of the spectrum. In SCS, the calculation of the second-order transition amplitudes associated with $\boldsymbol{A} \cdot \boldsymbol{P}$ implies transitions between continuum intermediate states and continuum final states. A convergence analysis based on perturbation theory does not work in our case given our approach to calculate continuum states. As explained at the end of section 1.4.1, to ensure ℓ-degeneracy of the different UCSs at a given energy, our implementation effectively changes the box size by including a step potential in the one-electron Hamiltonian. Although the change in box size is small enough to ensure orthogonality between states, each continuum state is in fact calculated with a different basis set. As pointed by Bachau and Dieng [109], for a perturbative calculation involving continuum-continuum couplings in a discretized basis to converge, all states must be calculated using the same B-spline basis set. For this reason, our convergence analysis is based on the resolution of the TDSE.

In this convergence analysis, we focus on the effect of additional ionization thresholds in SCS calculations using ultrashort pulses. In the previous chapter, we showed that, for the dipole contribution to SRS, the inclusion of additional ionization thresholds other than $1s\sigma_g$ was not necessary based on their role as intermediate states and in their effect in the multichannel description of the ${}^1\Sigma_u^+(1s\sigma_g)$ continuum. Although we do not expect higher ionization thresholds to play a significant role as intermediate states in SCS, continuum-continuum couplings are more sensitive to the multichannel description of the continuum compared to bound-continuum couplings.

The role of higher ionization thresholds as final states of SCS processes needs to be addressed as well, in this case, for both dipole and non-dipole transitions.

Following our study of SRS with ultrashort pulses, we use the same total Hamiltonian as the one shown in equation 5.18 including retardation effects for the interaction between H_2 and a pulse with polarization along z and propagation along x.

$$\mathcal{H} = \mathcal{H}_{el} + A(t)\sum_i P_{z_i} + \frac{1}{c}A(t)E(t)\sum_i x_i. \tag{6.1}$$

We also use the same pulse parameters as in the previous chapter, a Gaussian-shaped pulse with a FWHM of 68 as, a central frequency $\omega = 20$ a.u., and a peak intensity of $I = 10^{18}$ W/cm^2. With an ionization potential of $I_p = 0.6$ a.u. at an internuclear distance $R_e = 1.4$ a.u., and a spectral bandwidth for the pulse of 2 a.u., the pulse energetically allows for SCS processes to take place. In the calculations, we have included bound and continuum states of symmetries $^1\Sigma_g^+$ and $^1\Sigma_u^+$ with bound-bound, bound-continuum, and continuum-continuum couplings for the dipole contribution. For the non-dipole contribution, we have included couplings between bound states of symmetry $^1\Sigma_g^+$ and bound and continuum states of symmetry $^1\Pi_u$.

In figure 6.1, we present the PES of two separate calculations. In the first one, the H_2^+ ion can only be left in the $1s\sigma_g$ state, whereas for the second one, the ion can be left in both $1s\sigma_g$ and $2p\sigma_u$ states. We observe three peaks at 20, 40, and 60 a.u., corresponding to one-, two- and three-photon absorption process. After an analysis of the dependence with the intensity of the pulse, we observed a quadratic dependence on the peak close to threshold, indicating a two-photon process; we associated this peak with SCS. The blowup of the SCS peak from figure 6.1 includes the contributions from $\boldsymbol{A}\cdot\boldsymbol{P}$ and $\boldsymbol{A}^2$ obtained from calculations with the partial Hamiltonians $\mathcal{H}_{A\cdot P}$ and $\mathcal{H}_{A^2}$, presented in equation 5.27 of the last chapter, with the corresponding symmetries of the continuum. As it can be seen, non-dipole dominates throughout the SCS peak and only becomes comparable to the dipole for larger photoelectron energies of the SCS region. Regarding the effect of the inclusion of the second ionization threshold, no significant difference is observed between the two calculations and keeping only the first ionization threshold in the calculation leads to converged results for the angle integrated PES.

In contrast with PES, photoelectron angular distributions are much more sensitive to non-dipole corrections. Unlike SRS, where dipole and non-dipole transitions populate states with different symmetries and energies, both contributions populate continuum states with the same electronic energy in SCS, as seen in 6.1. As we discussed in Chapter 4, when states of different symmetry with respect to the inversion center of the molecule are populated, strong asymmetries are produced resulting from the interference between partial waves. The inclusion of additional thresholds in the calculation may result in changes in the MFPADs that do no manifest in the PES. Figure 6.2 shows the total MFPADs integrated in photoelectron energy over the region of the SCS peak ($0 - 2.5$ a.u.) for calculations including one and two ionization thresholds. In both cases, we observe a reflection symmetry in the $x-o-y$ and $x-o-z$ planes and a forward asymmetry in the direction of the propagation of the field. We found this asymmetry to be produced by the interference between $^1\Sigma_g^+$ and $^1\Pi_u$ states, populated by dipole and non-dipole transitions, respectively. No significant difference between the two calculations is observed whatsoever, which brings us to conclude that $2p\sigma_u$ does not play a significant role in SCS. At this point we did not try to perform any additional convergence tests with higher ionization thresholds. Therefore, all the calculations presented in this chapter only take into

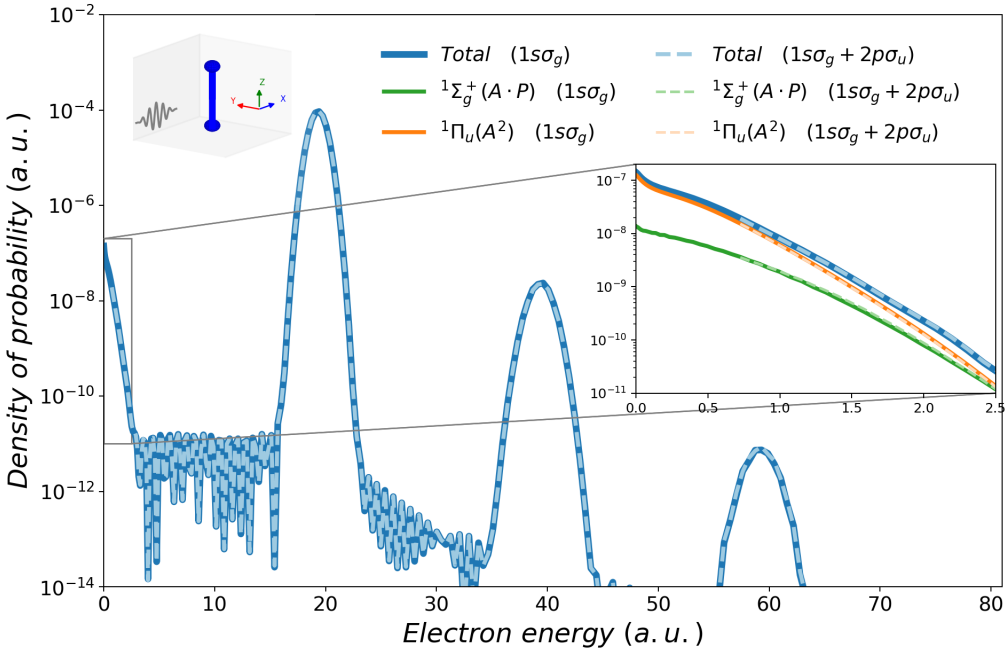

FIGURE 6.1 – PES for SCS calculations performed with the full Hamiltonian from equation equation 6.1 for a pulse with $\omega = 20$ a.u., polarization along the z axis and propagation along x axis. The ionization probabilities represent the cases were H_2^+ can only be left in the $1s\sigma_g$ state (dark colors), or in both $1s\sigma_g$ and $2p\sigma_u$ states (light colors). This last one was calculated as the sum of the individual probabilities of H_2^+ being left in $1s\sigma_g$ and $2p\sigma_u$. The inset shows the zoom on the electron energy range 0-2.0 a.u. with the contributions associated with $\boldsymbol{A}\cdot\boldsymbol{P}$ and $\boldsymbol{A}^2$, and their corresponding symmetries (see legend).

account processes where the ion is left in the first ionic state $1s\sigma_g$. Computation of the continuum-continuum couplings needed for the dipole contribution to SCS scales from two days to almost three weeks when introducing the second ionization threshold, so testing the effect of any additional threshold quickly becomes prohibitively expensive.

It is worth noting that the MFPADs shown here were not calculated satisfying incoming boundary conditions that localize one of the protons in a given center like in Chapter 4. Instead, we use the incoming boundary conditions from equation 3.39 and perform an incoherent summation over the different thresholds of the triply differential probabilities.

6.2 Molecular orientation effect

The loss of spherical symmetry in molecules with respect to atoms opens the possibility to tackle the study of non-dipole effects with a higher degree of freedom, especially in the region where the dipole and non-dipole contributions compete with each other. In this section, we present results for SCS calculations in which we analyze the effect of photon energy and molecular orientation. For convenience, we study the case of three different laser configurations with respect to a molecule oriented with the internuclear axis parallel to the z axis. The three configurations studied are the following:

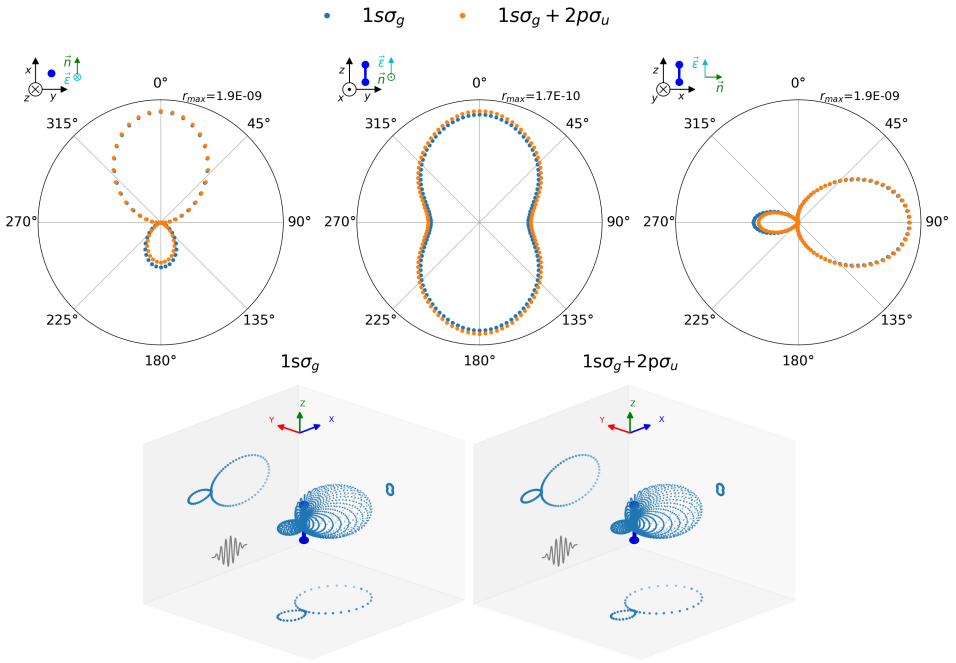

FIGURE 6.2 – Total MFPADs, integrated over photoelectron energies ranging from 0 to 2.5 a.u.) for SCS calculations performed with the full Hamiltonian from equation equation 6.1 for a pulse with $\omega = 20$ a.u., polarization along the z axis and propagation along x axis. The top row shows the 2D-projected MFPADs corresponding to the $x - o - y$ (left), $y - o - z$ (center), and $z - o - x$ (right) planes for the results of calculations including one threshold (blue) and two thresholds (orange). At the top of each 2D-MFPAD, a diagram appears indicating the orientation of the molecule, of the polarization vector ($\vec{\epsilon}$), and the propagation vector ($\vec{n}$) with respect to each projection plane. The lower panels show the 3D MFPADs for the calculation with one threshold (right) and two thresholds (left). As in figure 6.1, the MFPADs for the calculations with two threshold are obtained as the sum of the MFPADs associated with the $1s\sigma_g$ and $2p\sigma_u$ ionic states.

- Case 1: Polarization along z and propagation along $x \rightarrow A(t - \alpha \boldsymbol{n_x} \cdot \boldsymbol{r})\boldsymbol{\epsilon_z}$
- Case 2: Polarization along x and propagation along $z \rightarrow A(t - \alpha \boldsymbol{n_z} \cdot \boldsymbol{r})\boldsymbol{\epsilon_x}$
- Case 3: Polarization along x and propagation along $y \rightarrow A(t - \alpha \boldsymbol{n_y} \cdot \boldsymbol{r})\boldsymbol{\epsilon_x}$

These three configurations of the pulse are equivalent to studying orientations of the molecule along the three Cartesian axes for a fixed pulse configuration. The Hamiltonians representing the interaction between H_2 and a laser pulse including retardation effects of order $\mathcal{O}(1/c)$ for the cases 1, 2, and 3 read as follows:

$$\mathcal{H}^{(1)} = \mathcal{H}_{el} + A(t)\sum_i P_{z_i} + \frac{1}{c}A(t)E(t)\sum_i x_i \tag{6.2a}$$

$$\mathcal{H}^{(2)} = \mathcal{H}_{el} + A(t)\sum_i P_{x_i} + \frac{1}{c}A(t)E(t)\sum_i z_i \tag{6.2b}$$

$$\mathcal{H}^{(3)} = \mathcal{H}_{el} + A(t)\sum_i P_{x_i} + \frac{1}{c}A(t)E(t)\sum_i y_i. \tag{6.2c}$$

From the expressions of these Hamiltonians, we can already foresee some characteristics associated with the different cases. If retardation effects were to be neglected, thus returning to the dipole approximation, cases 2 and 3 would give the same result. The inclusion of non-dipole effects breaks the equivalence between different propagation directions for pulses with polarization perpendicular to the internuclear axis. On the other hand, cases 1 and 3, which have different behaviors in dipole approximation, are expected to become equivalent (save for a rotation of $\pi/2$ of the azimuthal angle) for high photon energies, where non-dipole effects dominate over the dipole contribution. Analogously to the partial Hamiltonians $\mathcal{H}_{A\cdot P}$ and $\mathcal{H}_{A^2}$ shown in equation 5.27, we can build partial Hamiltonians associated with the dipole and non-dipole contributions for each laser configuration. We label these operators as $\mathcal{H}^{(n)}_{A\cdot P}$ and $\mathcal{H}^{(n)}_{A^2}$ with $n = 1, 2, 3$.

Unlike for atoms, where the three previous Hamiltonians would be equivalent, the different orientations of the position and momentum operators produce different matrix elements and have associated different selection rules. For a molecule initially in the ground state, the different possible transitions for the dipole contribution to SCS can be summarized as follows:

$$X^1\Sigma_g^+ \xrightarrow{P_z} {}^1\Sigma_u^+ \xrightarrow{P_z} {}^1\Sigma_g^+ \tag{6.3}$$

$$X^1\Sigma_g^+ \xrightarrow{P_x,P_y} {}^1\Pi_u \xrightarrow{P_x,P_y} {}^1\Sigma_g^+, {}^1\Delta_g \tag{6.4}$$

$$\tag{6.5}$$

and, for non-dipole,

$$X^1\Sigma_g^+ \xrightarrow{x,y} {}^1\Pi_u \tag{6.6}$$

$$X^1\Sigma_g^+ \xrightarrow{z} {}^1\Sigma_u^+. \tag{6.7}$$

Our analysis of the impact of molecular orientation in SCS including retardation effects also examines the relationship between dipole and non-dipole contributions as a function of the photon energy. For each pulse configuration investigated, we studied three different photon energies, $\omega = 20$, 40 and 60 a.u.. The results are presented below.

6.2.1 Photoelectron spectra

In figure 6.3, we present the PES for SCS calculations for the three different pulse configurations, and the three photon energies studied. The results show the region ranging from 0 to 2.5 a.u., which corresponds to the SCS peak. For each pulse configuration, we show the different symmetries that contribute to the total PES. These symmetries are in agreement with the different selection rules associated with $\boldsymbol{A}\cdot\boldsymbol{P}$ and A^2 for a given pulse configuration. For the case 1, dipole transitions populate continuum states of symmetry ${}^1\Sigma_g^+$, and non-dipole transitions populate ${}^1\Pi_u$ states. For the case 2, dipole transitions populate continuum states of symmetry ${}^1\Sigma_g^+$ and ${}^1\Delta_g$, and non-dipole transitions populate ${}^1\Sigma_u^+$ states. Finally, for case 3, dipole transitions populate continuum states of symmetry ${}^1\Sigma_g^+$ and ${}^1\Delta_g$, and non-dipole transitions populate ${}^1\Pi_u$ states. We observed that for cases 2 and 3, dipole transitions have a preference to populate ${}^1\Sigma_g^+$ states, and ${}^1\Delta_g$ states do not contribute in a significant way to the total photoelectron spectrum.

As we anticipated, cases 2 and 3 have similar behavior for low photon energies on account of the dominance of the dipole contribution, same as cases 1 and 3 for high photon energies due to the predominance of the non-dipole contribution. For a given value of ω, all three cases have a density of probability of the same order of magnitude, which rapidly drops as ω increases. When looking at the relative strength of the dipole and non-dipole contributions as a function of photon energy, we see that the non-dipole ionization route becomes more dominant over the dipole route for higher photon energies for all molecular orientations studied. This is explained by the partial cancellation of the second-order transition amplitudes associated with $\boldsymbol{A}\cdot\boldsymbol{P}$ that we already saw for the study of SRS. However, the photon energy at which $\boldsymbol{A}^2$ starts to dominate over $\boldsymbol{A}\cdot\boldsymbol{P}$ is not the same for the three cases studied. Whereas for case 1, non-dipole effects dominate even for $\omega = 20$ a.u., for cases 2 and 3, this happens at higher photon energies, especially for case 2 for which non-dipole effects are not completely dominant even at $\omega = 60$ a.u.. A simple explanation of this trend can be made in terms of whether the internuclear axis is parallel or perpendicular to the polarization or propagation vectors of the field, related to dipole and non-dipole effects, respectively. In dipole approximation, ionization is stronger for pulses with perpendicular polarization to the internuclear axis of diatomic molecules [100]. The non-dipole contribution also exhibits this preference, but this time for perpendicular propagation directions, based on its relation to the dipole matrix elements in length gauge. Observation of non-dipole effects is then easier in case 1 as it has the weakest dipole signal (parallel polarization) and the strongest non-dipole signal (perpendicular propagation). The opposite happens for case 2, which has the strongest dipole signal (perpendicular polarization) and the weakest non-dipole signal (parallel propagation). Case 3 presents an intermediate behavior regarding the onset of non-dipole effects since both dipole and non-dipole contributions are perpendicular to the internuclear axis.

6.2.2 Integrated MFPADs

In figure 6.2 we observed that the inclusion of non-dipole effects results in the appearance of asymmetries in the MFPADs as a consequence of states with *gerade* and *ungerade* symmetries being populated. As we showed in the PES, for all molecular orientations studied, continuum states of these two symmetries are populated, so we expect some degree of asymmetry to appear in all the MFPADs. Before analyzing the results for the calculations with the full Hamiltonian, it is worth showing MFPADs for partial calculations including only the dipole or non-dipole operators in the Hamiltonian.

Because of the cylindrical symmetry of H_2, only two cases are non-equivalent for both $\boldsymbol{A}\cdot\boldsymbol{P}$ and $\boldsymbol{A}^2$ transitions. On this account, four different partial Hamiltonians can be built: $\mathcal{H}^{(1)}_{A\cdot P}(P_z)$, $\mathcal{H}^{(2)}_{A\cdot P}(P_x)$, $\mathcal{H}^{(1)}_{A^2}(z)$, and $\mathcal{H}^{(2)}_{A^2}(x)$. Figure 6.4 shows the corresponding 3D MFPADs with their phases as color map for calculations with these four Hamiltonians for a pulse with $\omega = 20$ a.u.. We have included a calculation with the Hamiltonian $\mathcal{H}^{(3)}_{A^2}(y)$ which, as can be seen, is equivalent to rotate by $\pi/2$ the results obtained from $\mathcal{H}^{(2)}_{A^2}(x)$. The MFPADs are integrated in photoelectron energy in the region between $0-2.0$ a.u., which is efficiently populated by SCS. For dipole transitions, the major contribution to the MFPADs comes from states of symmetry $^1\Sigma^+_g$ for both parallel and perpendicular polarization directions. In comparison, the contribution from states of symmetry $^1\Delta_g$ was found to be negligible. For non-dipole transitions, the MFPADs are associated with $^1\Sigma^+_u$ states for propagation directions

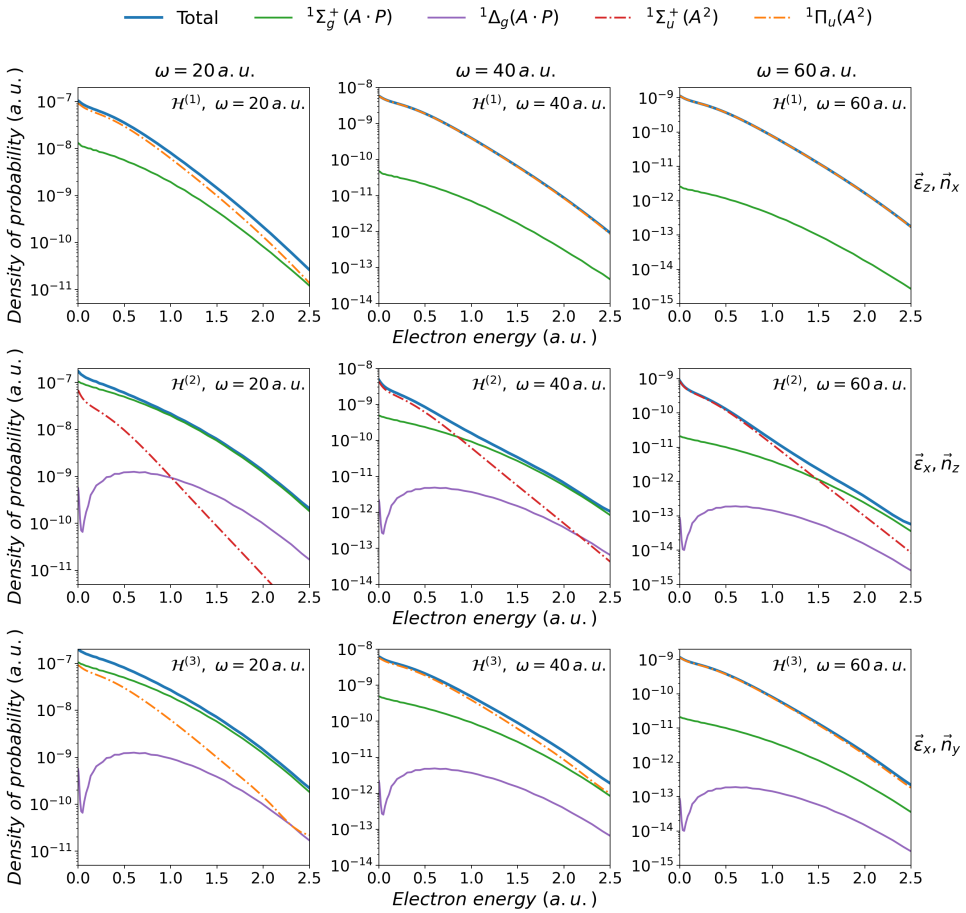

FIGURE 6.3 – PES calculated in the near threshold region for the pulse configurations labeled as case 1 (top row), case 2 (middle row), and case 3 (bottom row). The calculations were performed with $\omega = 20$ a.u. (left columns), $\omega = 40$ a.u. (middle columns), and $\omega = 60$ a.u. (right columns). Calculations are performed with the full Hamiltonians $\mathcal{H}^{(1)}$, $\mathcal{H}^{(2)}$, and $\mathcal{H}^{(3)}$, shown in equation 6.2 (blue line). The contributions associated with $\boldsymbol{A}\cdot\boldsymbol{P}$ and $\boldsymbol{A}^2$, and their corresponding symmetries (see legend), are also shown.

parallel to the internuclear axis, and with $^1\Pi_u$ states for perpendicular propagation. This is in agreement with our observations in the PES.

Neither dipole and non-dipole contributions present asymmetries in the direction of ejection of the electron. This confirms that the asymmetries appearing in figure 6.2 are due to the interference between different partial waves associated with the two contributions. Moreover, the phase relation between the two contributions shown in the upper row of figure 6.4, is consistent with the appearance of a forward asymmetry in the ejection direction of the electron. For both calculations in dipole approximation, there is a strong predominance of the $\ell = 0$ partial wave, as reflected by the spherical or quasi-spherical shape of the MFPADs. For the calculations including only the contribution from $\boldsymbol{A}^2$, we observe the typical two-lobe structure of one-photon absorption resulting from a predominance of the $\ell = 1$ partial wave associated with the operator coupling having the same properties as the dipole operator acting along the propagation axis. It is worth commenting that only a difference in the absolute magnitude of the integrated MFPADs was observed for $\omega = 40$ and 60 a.u. was in the absolute magnitude of the partial MFPADs. The role of photon

energy is then to simply modulate the relative weight between the different contributions shown in figure 6.4. With the phase relation between each contribution of the MFPADs, we can also anticipate that the three molecular orientations will present asymmetries aligned with the propagation of the field.

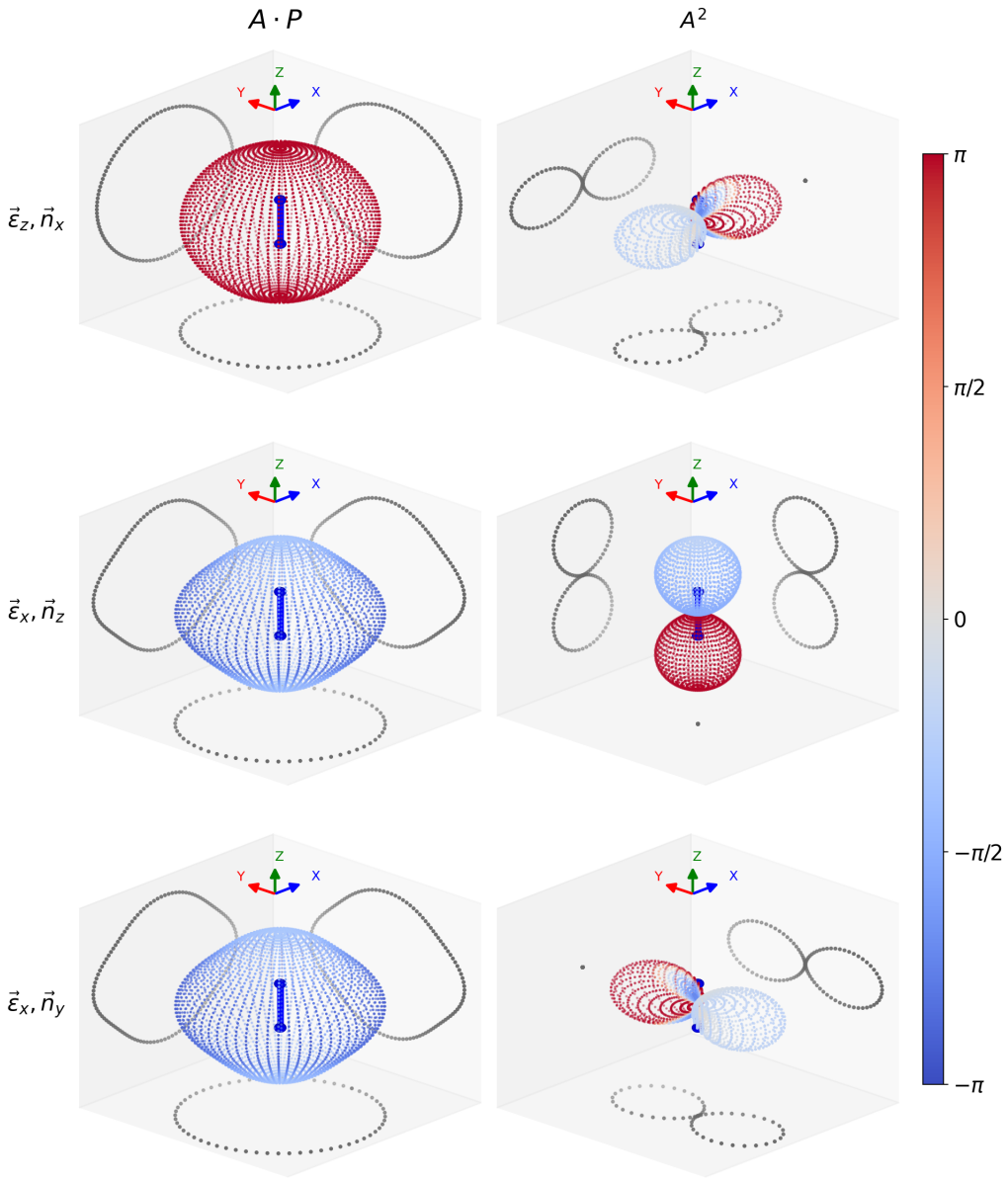

FIGURE 6.4 – Partial MFPADs for $\omega = 20$ a.u. obtained from calculations using $\mathcal{H}^{(1)}_{A\cdot P}$ (top left panel), $\mathcal{H}^{(2)}_{A\cdot P}$ (middle left and bottom left panels), $\mathcal{H}^{(1)}_{A^2}$ (top right panel), $\mathcal{H}^{(2)}_{A^2}$ (middle right panel), and $\mathcal{H}^{(3)}_{A^2}$ (bottom right panel). The figure also shows 2D-projections of the $x-o-y$, $y-o-z$, and $z-o-x$ planes in grey and a color map representing the phase of the differential in angle amplitudes. This figure is not on scale.

In figure 6.5, we show the total 3D MFPADs obtained from calculations considering the full Hamiltonian for the different pulse configurations and photon energies studied. The 2D-projections of the $x-o-y$, $y-o-z$, and $z-o-x$ planes that appear also include the different contributions to the total MFPADs. As with the partial calculations, these MFPADs are integrated in photoelectron energy in the region ranging from 0.0 to 2.0 a.u.. The interference between dipole and non-dipole ionization routes produces asymmetries in the total MFPADs for all cases studied in agreement with the phase relation between the $\boldsymbol{A}\cdot\boldsymbol{P}$ and $\boldsymbol{A}^2$ amplitudes shown in figure 6.4. One of the first things we notice is that non-dipole effects manifest in a more pronounced way in the MFPADs compared to what we observed in the PES. All molecular orientations and photon energies studied show a dominance of the non-dipole contribution in the MFPADs except for case 2 at $\omega = 20$ a.u., for which the two contributions are equivalent.

As a general trend, we observe a decrease in the asymmetry of the MFPADs with photon energy. For high photon energies, the 2D-projections show that the dipole contribution is almost imperceptible so that the total 2D-MFPADs is composed almost entirely of states populated by non-dipole transitions. Since the non-dipole contribution is symmetric, as shown in figure 6.4, when non-dipole effects fully dominate over the dipole contribution, the asymmetries in the ejection of the electron disappear. We then retrieve the typical two-lobe structure of one-photon ionization in dipole approximation but with alignment along the propagation direction of the field. It is worth noting that, to recover symmetric MFPADs, the dipole contribution needs to be negligible with respect to the non-dipole one. For very low dipole but non-negligible contributions, like the ones seen for case 1 at $\omega = 20$ a.u., case 2 at $\omega = 60$ a.u. and case 3 at $\omega = 40$ a.u., asymmetries appear even though the non-dipole contribution is dominant. This confirms the high contrast interference effect between the $\boldsymbol{A}\cdot\boldsymbol{P}$ and $\boldsymbol{A}^2$ amplitudes.

Similar to what we observed for the PES from figure 6.3, the photon energy at which the asymmetry is lost is not the same for every laser configuration. While case 1 has lost much of the asymmetry for $\omega = 40$ a.u., for case 2, there is still a noticeable asymmetry for $\omega = 60$ a.u.. Regarding the direction of the asymmetry, two different cases can be observed. A forward asymmetry is produced when the internuclear axis is contained in the plane formed by the propagation and polarization vectors. In contrast, when the internuclear axis is perpendicular to this plane, a backward asymmetry is observed. This can be explained by the opposite phase relation between the dipole and non-dipole contributions in the direction of propagation of the laser, as shown in 6.4, unlike for the two other cases studied. It is worth recalling that, for $\omega = 20$ a.u., the PES of cases 2 and 3 are practically identical given the general dominance of the dipole contribution throughout the energy interval of SCS. However, the corresponding MFPADs in figure 6.5 clearly differ. This shows the crucial effect of the molecule orientation relative to the propagation and polarization directions.

6.2.3 Differential in photoelectron energy MFPADs

The study of MFPADs as a function of photoelectron energy (E_e) reveals many aspects of the formation of asymmetries, caused by the interference between dipole and non-dipole ionization routes, which hidden in the integrated MFPADs. Figures 6.6, 6.7, and 6.8 show 2D-projections of the total MFPADs for cases 1, 2, and 3 respectively, with its contributions, in the plane containing the polarization and propagation vectors. We show results for $\omega = 20$, 40 and 60 a.u. (columns), and for

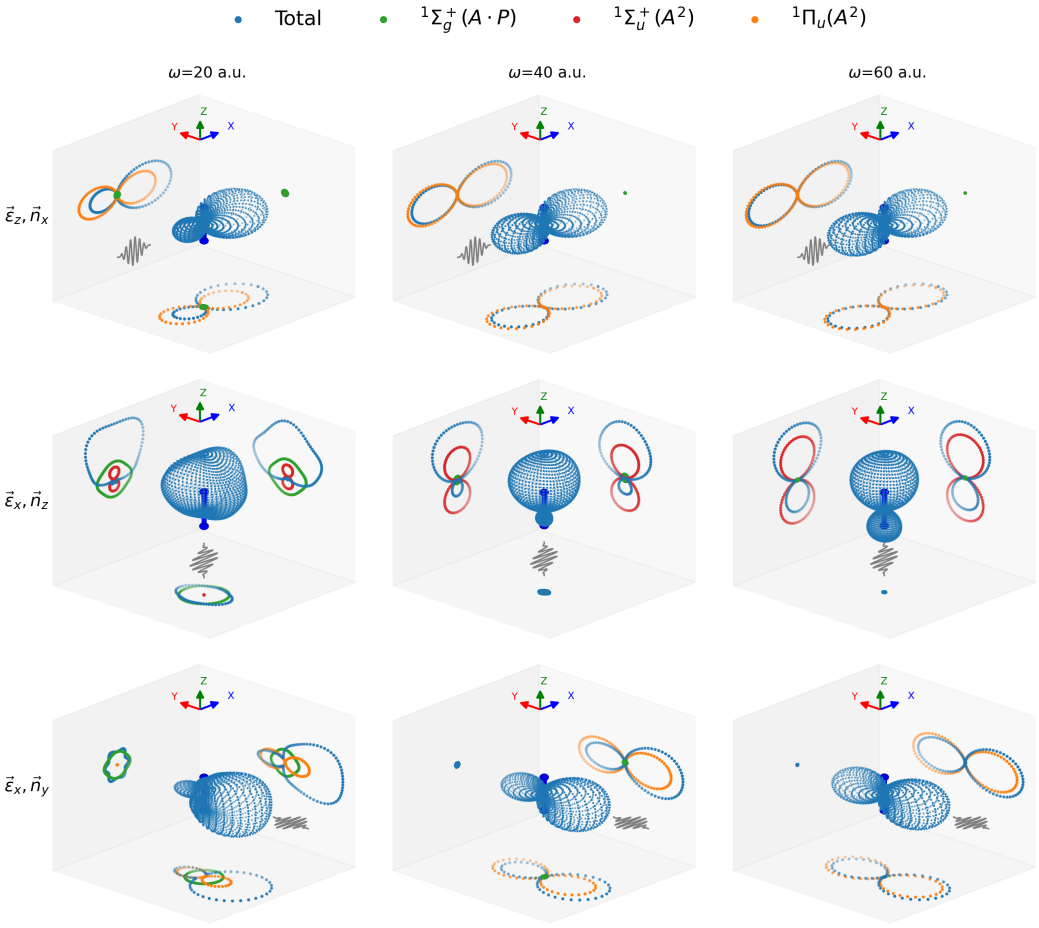

FIGURE 6.5 – Total 3D MFPADs integrated in the region of photoelectron energy near threshold for the pulse configurations labeled as case 1 (top row), case 2 (middle row), and case 3 (bottom row). The calculations were performed with $\omega = 20$ a.u. (left columns), $\omega = 40$ a.u. (middle columns), and $\omega = 60$ a.u. (right columns). The figure also shows 2D-projections of the $x - o - y$, $y - o - z$, and $z - o - x$ planes for the full calculation (blue) and for the contributions associated with $\boldsymbol{A} \cdot \boldsymbol{P}$ and $\boldsymbol{A}^2$, and their corresponding symmetries (see legend).

photoelectron energies close to 0.1, 0.9 and 1.6 a.u. (rows). A common feature that all cases share is the resemblance between the differential MFPADs for low photoelectron energies, represented in the first row of each figure, and the corresponding integrated MFPAD. This is due to the dominant contribution of lower E_e values in the latter, as seen in the PES.

Regarding the distribution magnitude, labeled as r_{max}, we observe a rapid decrease as E_e or ω increases for all contributions involved, also in agreement with the PES. The decrease of the magnitude of the MFPADs with photoelectron energy is steeper for the non-dipole contribution compared to the dipole one. In case 2, for $\omega = 20$ and 40 a.u., we even observe MFPADs dominated by the dipole contribution for large values of E_e, which was not observed in the integrated distributions.

For MFPADs corresponding to case 1, depicted in figure 6.6, we observe a general

dominance of non-dipole effects for all photon energies and photoelectron energies considered. No significant evolution of the asymmetry is observed with the photoelectron energy. This is expected as this case presents the strongest non-dipole contribution (perpendicular propagation) and the weakest dipole contribution (parallel polarization).

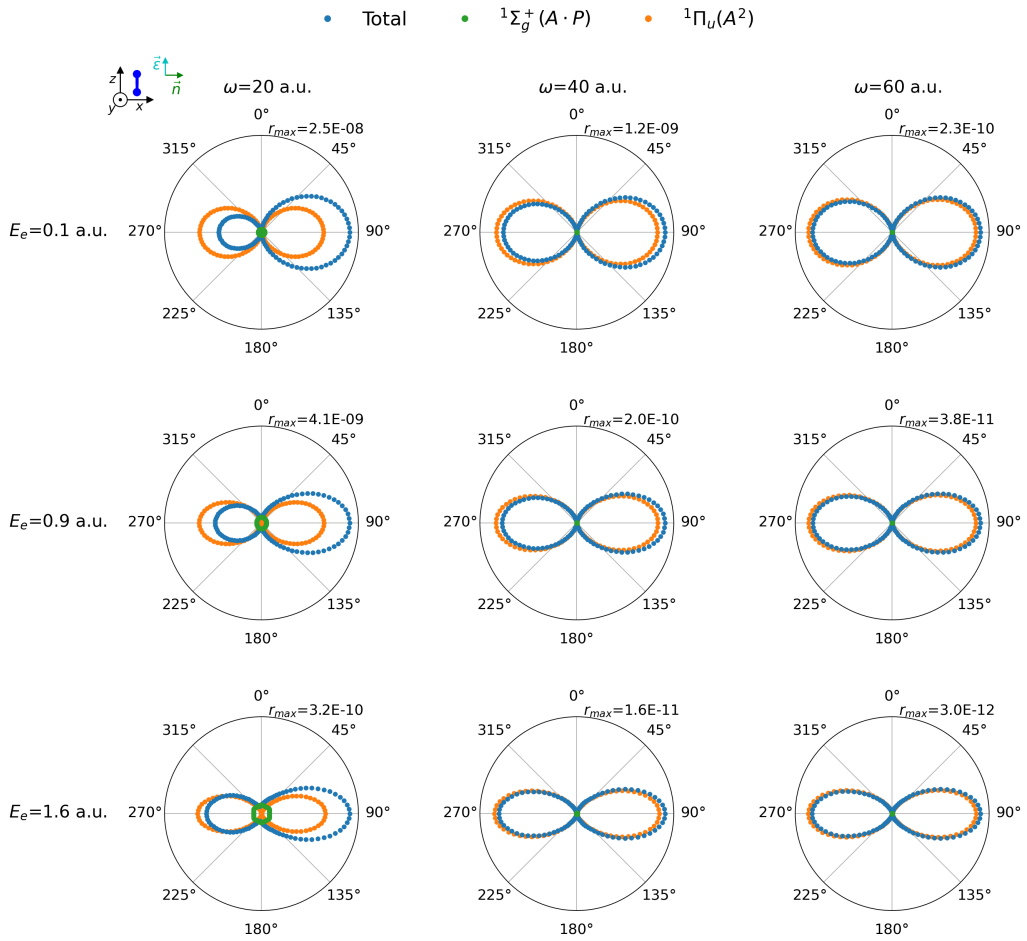

FIGURE 6.6 – 2D-MFPADs differential in photoelectron energy calculated for the pulse configuration corresponding to case 1 with $\omega = 20$ a.u. (left columns), $\omega = 40$ a.u. (middle columns), and $\omega = 60$ a.u. (right columns). The MFPADs correspond to the photoelectron energies $E_e = 0.1$ a.u. (top row), $E_e = 0.9$ a.u. (middle row), and $E_e = 1.6$ a.u. (bottom row) for the full calculation (blue) and for the contributions associated with $\boldsymbol{A} \cdot \boldsymbol{P}$ and $\boldsymbol{A}^2$, and their corresponding symmetries (see legend). The 2D projection is performed in the $z - o - x$ plane defined by the polarization ($\vec{\varepsilon} \equiv \boldsymbol{\epsilon}$) and propagation ($\vec{n} \equiv \boldsymbol{n}$) vectors as indicated in the diagram appearing at the top of the figure.

The analysis of the MFPADs corresponding to case 2, shown in figure 6.7, reveals many aspects of the interference between dipole and non-dipole contribution. Since this case has the weakest non-dipole contribution (parallel propagation) and the strongest dipole contribution (perpendicular polarization), it is possible to observe strong interference between the two different ionization paths at several photoelectron energies. For this case, the enhancement of the dipole relative contribution with E_e becomes clear for all photon energies, especially for $\omega = 20$ and 40 a.u. where it becomes dominant. This creates different regimes regarding the evolution of the

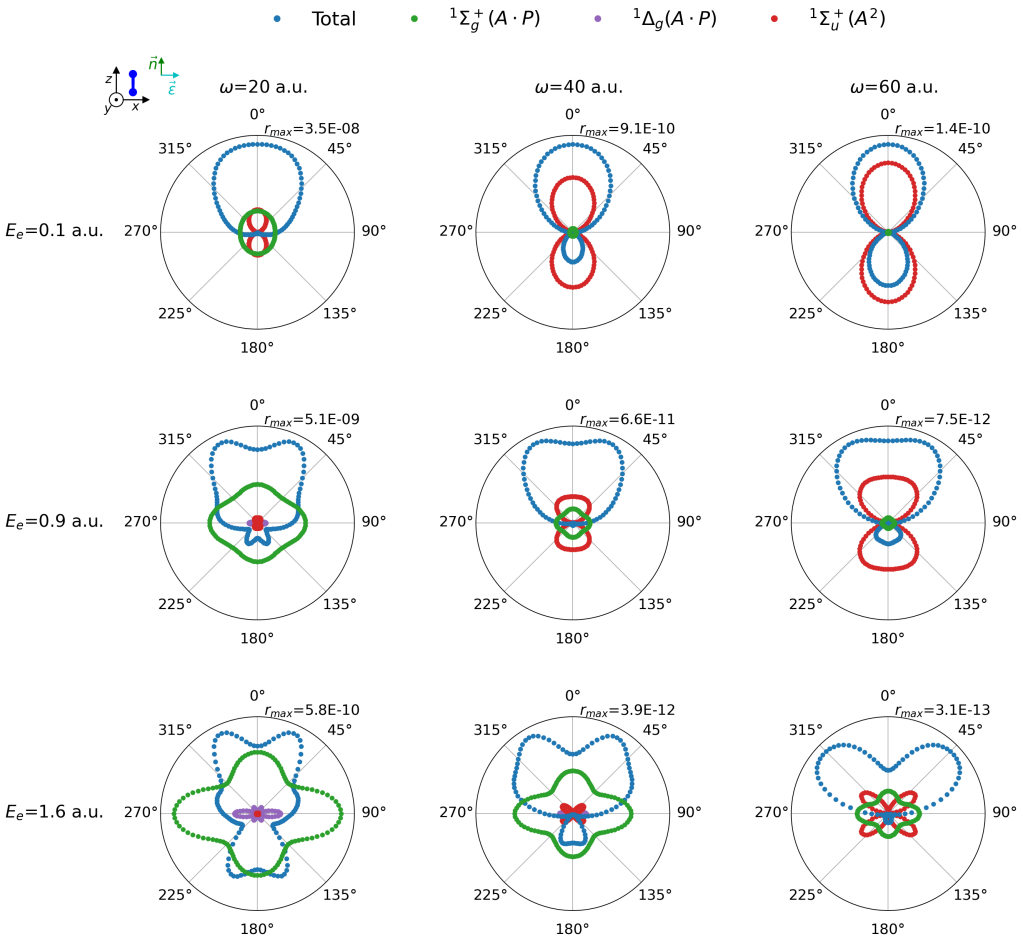

FIGURE 6.7 – 2D-MFPADs differential in photoelectron energy calculated for the pulse configuration corresponding to case 2 with $\omega = 20$ a.u. (left columns), $\omega = 40$ a.u. (middle columns), and $\omega = 60$ a.u. (right columns). The MFPADs correspond to the photoelectron energies $E_e = 0.1$ a.u. (top row), $E_e = 0.9$ a.u. (middle row), and $E_e = 1.6$ a.u. (bottom row) for the full calculation (blue) and for the contributions associated with $\boldsymbol{A}\cdot\boldsymbol{P}$ and $\boldsymbol{A}^2$, and their corresponding symmetries (see legend). The 2D projection is performed in the $z-o-x$ plane defined by the polarization ($\vec{\varepsilon} \equiv \boldsymbol{\epsilon}$) and propagation ($\vec{n} \equiv \boldsymbol{n}$) vectors as indicated in the diagram appearing at the top of the figure.

asymmetry for the different photon energies studies. For $\omega = 20$ a.u. we observe a decrease of the asymmetry with E_e, while the opposite is observed for $\omega = 60$ a.u.. At high photoelectron energies, we are also able to observe the appearance of higher partial waves for both contributions, which results in the appearance of a dip in the center of the upper lobe of the MFPAD. This shape is not observed for propagation directions along x or y. One may therefore surmise that it is an effect related to the collinearity of the molecular axis and propagation direction.

For case 3, shown in figure 6.8, we observe a pronounced decrease in the asymmetry with E_e for $\omega = 20$ a.u.. For $\omega = 40$ and 60 a.u., no significant variation of the asymmetry is observed. As in case 2, we observe an increase of the relative dipole contribution with E_e, especially at low ω, which results in a loss of the asymmetry. Comparing the relative strengths between dipole and non-dipole contributions at $\omega = 20$ a.u., we noticed that, while for both $E_e = 0.1$ and 1.6 a.u. the

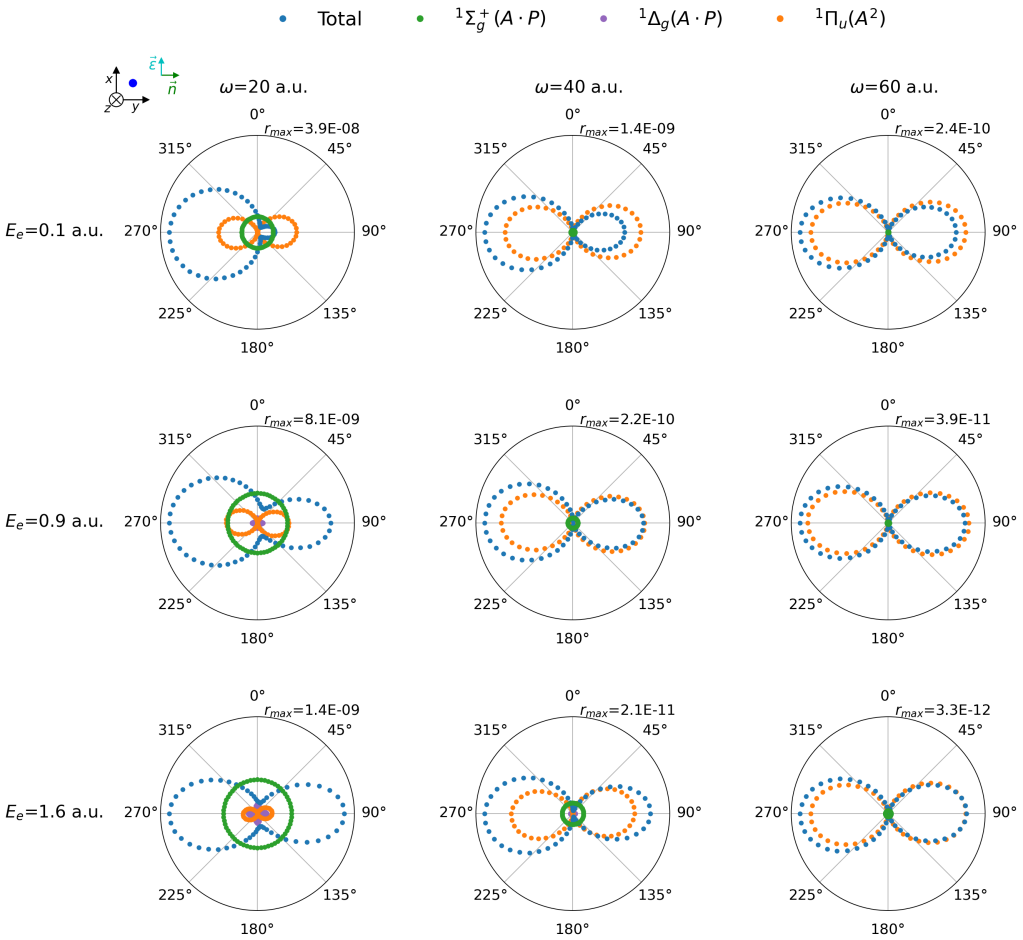

FIGURE 6.8 – 2D-MFPADs differential in photoelectron energy calculated for the pulse configuration corresponding to case 3 with $\omega = 20$ a.u. (left columns), $\omega = 40$ a.u. (middle columns), and $\omega = 60$ a.u. (right columns). The MFPADs correspond to the photoelectron energies $E_e = 0.1$ a.u. (top row), $E_e = 0.9$ a.u. (middle row), and $E_e = 1.6$ a.u. (bottom row) for the full calculation (blue) and for the contributions associated with $\boldsymbol{A}\cdot\boldsymbol{P}$ and $\boldsymbol{A}^2$, and their corresponding symmetries (see legend). The 2D-projection is performed in the $x-o-y$ plane defined by the polarization ($\vec{\epsilon}\equiv\boldsymbol{\epsilon}$) and propagation ($\vec{n}\equiv\boldsymbol{n}$) vectors as indicated in the diagram appearing at the top of the figure.

leading contribution is approximately two times stronger than the other, the asymmetry almost disappears if the dominant contribution is the dipole one. We found that when the non-dipole contribution relative to the dipole is between 0.5 and 20 times, asymmetries appear. In any other case, we obtain symmetric distributions. This stresses the important role of dipole effects in the formation of asymmetries in the MFPADs. For MFPADs dominated by non-dipole effects, a small contribution from the dipole amplitudes is able to produce strong asymmetries. On the other hand, if the MFPADs is dominated by the dipole contribution, non-dipole effects are not as capable of producing asymmetries. It is therefore of major importance to evaluate accurately the dipole contribution.

Conclusions

In this part of the thesis, we have presented results for the study of inelastic scattering of X-ray photons by the H_2 molecule beyond the dipole approximation. The H_2 molecule was treated in the non-relativistic approximation with frozen nuclei at the equilibrium distance. For this study, we have reviewed two different processes, SRS and SCS. Chapter 5 focused on the perturbative treatment of SRS. We have investigated the relative role of the dipole ($\boldsymbol{A}\cdot\boldsymbol{P}$) and non-dipole ($\boldsymbol{A}^2$) interaction terms through the study of the Raman cross-section. We have derivated the KHW matrix elements necessary to calculate the Raman cross-section in the framework of TDPT. We have shown that the partial cancellation of the dipole contribution is produced by the interference between the second-order transition amplitudes associated with direct and inverse excitation paths. We have also performed convergence tests in order to achieve a good description of the high energy continuum states relevant to describe SRS and SCS. We were able to correctly reproduce the continuum wave function up to 80 a.u. of electron energy. In the last part of this chapter, we have presented SRS results from calculations using a Gaussian-shaped pulse with a FWHM of 68 as, an intensity of 10^{18} W/cm^2, propagation direction along x, polarization direction along z, and frequencies ranging from 5 a.u. to 60 a.u. in the context of TDPT. Several perturbative schemes have been presented, which required the development of a new set of computational tools. Special attention has been given to the numerical problems associated with intermediate continuum resonant states. We successfully extended the TDFCC method to study retardation effects and have presented results for non-perturbative calculations in SRS. The agreement between results obtained by solving the TDSE and our scheme based on TDPT validates the use of perturbation theory as a proper tool for studying retardation effects in SRS. We have observed two different excitation mechanisms, one at low photon energies dominated by the dipole contribution and one at high energies dominated by non-dipole effects. As a result of the presence of two different excitation mechanisms, bound states of different symmetries are populated. The resulting excitation probabilities have been fitted to two different power laws in terms of the photon energy.

In Chapter 6 we have presented a study on SCS beyond the dipole approximation using ultrashort pulses based on the resolution of the TDSE. Our analysis of the results has focused on the examination of PES, integrated in photoelectron energy MFPADs, and differential in photoelectron energy MFPADs. As a continuation of the convergence tests performed in the previous chapter, we have conducted an analysis of the effect of higher ionization thresholds in the close-coupling expansion of the electronic continuum. For this analysis, we performed calculations using a Gaussian-shaped pulse with the same parameters as in the previous chapter with a frequency of 20 a.u.. Particular attention has been given to the energy region E_e ranging from 0 to 2.5 a.u., associated with Compton scattering. We have shown that the non-dipole contribution dominates the PES over the whole range of the SCS peak for this particular pulse configuration. As a result of the interference between dipole and non-dipole ionization routes, we observed asymmetries in the integrated MFPADs. We have shown that the inclusion of the first ionization threshold already

leads to converged results for both PES and MFPADs integrated for photoelectron energies in the region efficiently populated by SCS. This is not surprising if we take into account the difference between the cross-section to the first and second ionization thresholds presented in last the chapter.

Finally, we have presented an analysis of molecular orientation effects in the study of SCS. We performed calculations with three different pulse configurations equivalent to studying orientations of the molecule along the three Cartesian axes for a fixed pulse configuration. For each pulse configuration investigated, we used the same Gaussian-shaped pulse as before, and we have presented results for three different photon energies, $\omega = 20$, 40, and 60 a.u.. By studying the PES, we have shown that the non-dipole ionization route becomes more dominant over the dipole route for higher photon energies for all molecular orientations studied. This was associated with the partial cancellation of the dipole contribution. For the cases with perpendicular polarization, we found that the dipole transitions preferentially populate ${}^1\Sigma_g^+$, so the contribution of ${}^1\Delta_g$ can be neglected. We have observed a different evolution of the dominance of the non-dipole contribution as a function of photon energies in the PES for the different molecular orientations studied. An explanation of this trend in terms of the larger weight of the perpendicular components has been given. We have presented total MFPADs, integrated in the energy region associated with SCS, and its contributions from the different dipole and non-dipole contributions for the three different orientations studied. We have observed that non-dipole effects manifest in the MFPADs in a stronger way compared to the PES, thus producing asymmetries aligned with the propagation direction for all orientations studied, even for small contributions from dipole transitions. We have noticed a decrease of the asymmetry with photon energy due to the increase with photon energy of the relative weight of non-dipole effects over the dipole contribution. A forward asymmetry is produced for the cases where the plane formed by the propagation and polarization vectors contains the internuclear axis. In contrast, when this plane is perpendicular to the internuclear axis, a backward asymmetry is produced. We have associated this fact with the relative phase of the dipole and non-dipole contributions to the MFPADs. When analyzing the differential in photoelectron energy MFPADs, we have noticed a decrease in the magnitude with E_e and ω in agreement with the PES. For the case of the pulse propagation parallel to the internuclear axis with polarization perpendicular to it, we have shown that, due to strong dipole contribution and the weak non-dipole one, the evolution of the asymmetry with photoelectron energy is not consistent for all photon energies. This case, in particular, allows observing the appearance of higher partial waves for both contributions. After analyzing the MFPADs corresponding to the case where both polarization and propagation are perpendicular to the internuclear axis, we have concluded that, when dipole and non-dipole contributions compete, stronger asymmetries are produced if the dominant contribution comes from non-dipole effects.

General conclusions and perspectives

In this thesis, we have provided a theoretical description of the photoionization process using ultrashort laser pulses in the XUV and X-ray regimes. The theoretical toolbox used for this study has proven in the past to effectively treat the interaction between XUV and IR pulses and the H_2 molecule. We have laid the basic principles of this theoretical method, starting by describing the field-free molecular states. This part focused on building the two-electron wave function including electron correlation and nuclear motion with special attention on the description of resonant states and the electronic continuum. Specifically, in order to obtain electronic continuum states fulfilling asymptotic boundary conditions, our approach makes use of multichannel scattering theory. In the description of the electromagnetic field, the spatial dependence of the vector potential generally poses a challenge in actual calculations which is circumvented with the use of the dipole approximation. However, there are limits to the applicability of this approximation which depend on the specific conditions of the laser-matter interaction, mainly, the intensity and frequency of the field. In order to study photoionization in the soft X-ray regime going beyond the dipole approximation becomes mandatory. For that purpose, we have added to our theoretical toolbox the capacity to take into account retardation effects up to $\mathcal{O}(1/c)$ in a non-relativistic regime. This set of tools then allows to study photoionization of H_2 in its full dimensionality by analyzing the coupled electron-nuclear dynamics beyond the dipole approximation including autoionization. To test the capabilities of this set of tools we have performed a study in which we have been able to demonstrate the possibility of control of the one- and two-photon ionization yields by filtering the higher harmonics in an XUV pump-UV probe scheme using an APT in dipole approximation.

In the second part of the thesis results, we have studied non-dipole effects in the interaction of X-ray radiation with the H_2 molecule focusing on two emblematic processes, SRS and SCS. The purpose of our SRS study was to analyze the relative role of the dipole and non-dipole ionization routes through perturbative calculations from newly developed codes.

We have verified that, for photon energies larger than 10 a.u., non-dipole effects need to be taken into account and that, for photon energies of 60 a.u. or larger, non-dipole effects fully dominate the excitation mechanism in SRS due to the partial cancellation of the second-order transition amplitudes associated with the dipole contribution. This analysis has also confirmed the validity of the perturbative treatment in this regime by comparing with results obtained from non-perturbative calculations. In our study of SCS using ultrashort we have analyzed the effect of molecular orientation with respect to the pulse propagation. Due to the complexity of this kind of calculations in molecules with respect to atoms from the numerical point of view, to our knowledge, this is the first time that the effect of molecular orientation has been studied in SCS with such detail. As in the case of atoms, the interference between the two competing quantum paths (dipole and non-dipole) results in the

appearance of asymmetries in the MFPADs. Nonetheless, the difference between the strength of the dipole (non-dipole) couplings for parallel or perpendicular polarization (propagation) direction results in a strong evolution of this asymmetry with molecular orientation and photon energy. One of the main differences with respect to the atomic case is the appearance of backwards asymmetries with respect to the propagation directions when the molecular axis is perpendicular to both the polarization and propagation directions.

Due to the great computational effort involved in calculating all the couplings needed to describe two-photon transitions in the X-ray regime, our study of non-dipole effects has been restricted to the FNA. It is expected that, in the near future, XFELs facilities will be capable of producing intense X-ray pulses short enough to study non-dipole effects at ultrashort time scales. Our goal is to take advantage of the full potential of our theoretical toolbox to give the most accurate theoretical description of these phenomena by studying the effects of nuclear motion and autoionization beyond the dipole approximation.

With the theoretical tools developed during the thesis, we were also able to produce preliminary results on SCS using two-color pulses. This brings interesting perspectives due to the possibility of comparison with calculations in atoms [76], and the recent capabilities of XFELs sources in producing two-color X-ray pulses [110, 111]. In figures C.1 and C.2 we present the first SCS calculations using two colors in H_2. We have begun studying the case of pulses with propagation directions perpendicular to the internuclear axis with one of the pulses propagating along x with $\omega_1 = 20$ a.u. and the other with an angle β with respect to the first with $\omega_2 = 21$ a.u. and 25 a.u.. For the case with a color separation of 5 a.u., we observe two peaks, one associated with each pulse bandwidth and another resulting from $\omega_1 - \omega_2$. Due to the large spectral bandwidth of these pulses, for the case with a color separation of 1 a.u., only one peak is observed, but the signal is significantly larger. In both cases, for the region close to threshold for a color separation of 1 a.u. and at 4.5 a.u. for a color separation of 5 a.u., the signal significantly increases with the relative angle β with a maximum for counter-propagating pulses ($\beta = \pi$). However, this increase in the signal is more pronounced for lower relative propagation angles. This goes in agreement with what has been observed in atoms [76]. In the MFPADs shown in figure C.2, barely any asymmetry appears, in contrast with the case of one pulse with the same photon energy, due to the enhancement of the non-dipole contribution with the propagation angle.

The study of retardation effects beyond $\mathcal{O}(1/c)$ also presents interesting future perspectives, especially for two-color schemes like the one presented. For counter-propagating pulses, the momentum transfer $\boldsymbol{Q} = \boldsymbol{k_1} - \boldsymbol{k_2}$, calculated as the difference between the wavevectors of the two fields, significantly increases and higher-order terms might be necessary to correctly account for non-dipole effects.

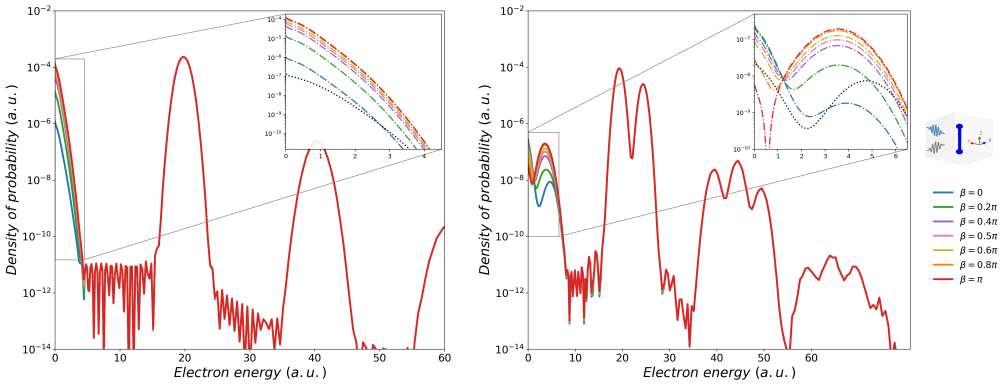

FIGURE C.1 – Total PES obtained from SCS calculations using two-color. The calculations were performed using two pulses of the same intensity and duration as those used in Part III with polarization along z and propagation perpendicular to the internuclear axis. The results correspond to a color separation between the pulses of 1 a.u. (left panel) and 5 a.u. (right panel). In the inset the different non-dipole contributions are shown in color lines and the dipole contribution is shown in black.

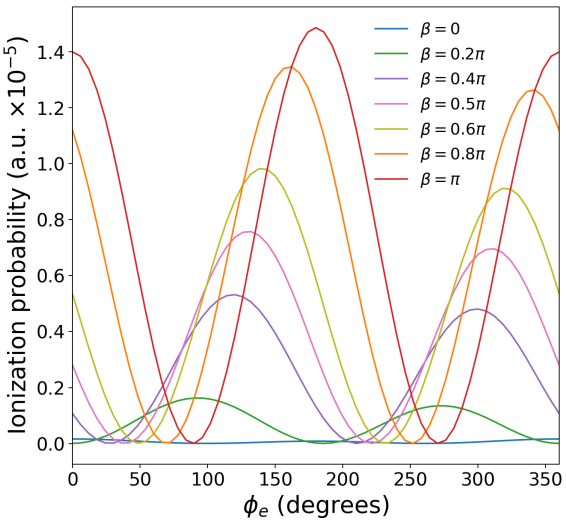

FIGURE C.2 – 2D-projections in the $x - o - y$ plane of the total MF-PADs for a color separation of 1 a.u. integrated between 0 and 2 a.u. of photoelectron energy. The abscissa ϕ_e corresponds to the angle of ejection of the electron with respect to the positive axis x in the projection plane.

Conclusiones generales

En esta tesis, hemos presentado una descripción teórica del proceso de fotoionización utilizando pulsos láser ultracortos en un régimen de energías entre el EUV y los rayos X. Hemos utilizado un conjunto de herramientas teórica con probada eficacia en el tratamiento de la interacción entre pulsos EUV e IR y la molécula de H_2. Hemos establecido los principios básicos de este método teórico comenzando con la descripción de los estados cuánticos de la molécula aislada. En esta parte, nos hemos centrado en construir la función de onda bielectrónica incluyendo correlación electrónica y movimiento nuclear. Se ha prestado especial atención a la descripción de los estados resonantes y el continuo electrónico. Para éstos últimos, hemos detallado nuestro enfoque multicanal para obtener estados del continuo que cumplan las condiciones de frontera asintóticas. En la descripción del campo electromagnético, nos hemos centrado en la dependencia espacial del potencial vectorial y hemos discutido los límites de aplicabilidad de la aproximación dipolar en función de la intensidad y frecuencia del campo. A continuación, hemos desarrollado el Hamiltoniano asociado a la interacción entre la molécula de H_2 y la radiación, incluyendo efectos de retardo hasta orden $\mathcal{O}(1/c)$ en un régimen no relativista. Finalmente, hemos descrito los diferentes métodos de propagación empleados para calcular las amplitudes de ionización de las que obtenemos diferentes observables físicos. Hemos probado este conjunto de herramientas estudiando el efecto del filtrado de armónico sen un esquema de pump UV-probe XUV utilizando un APT. En este estudio, hemos examinado la fotoionización de la molécula de H_2 incluyendo todos los grados de libertad mediante un análisis de la dinámica electrónica-nuclear acoplada, incluyendo la autoionización y en la aproximación dipolar.

En la segunda parte de los resultados de la tesis, hemos estudiado los efectos más allá de la aproximación dipolar en la interacción de rayos X y la molécula H_2. Nos hemos centrado en dos procesos emblemáticos de este régimen, SRS y SCS. Nuestro estudio de SRS ha servido para analizar el papel relativo de las rutas de ionización dipolar y no dipolar a través de cálculos perturbativos utilizando códigos desarrollados durante la tesis. Hemos verificado la cancelación parcial de las amplitudes de transición de segundo orden asociadas con la contribución del dipolar. Nuestro análisis también ha servido para parametrizar la función de onda de los continuos de alta energía y confirmar la validez del tratamiento perturbativo en este régimen. Hemos presentado resultados para cálculos de SCS utilizando pulsos ultracortos en los que hemos analizado el efecto de la orientación molecular con respecto a la propagación del pulso. Hemos analizado los diferentes roles de las rutas de ionización dipolar y no dipolar en función de la orientación molecular, la energía fotónica y la energía fotoelectrónica. Hemos examinado también los MFPAD, que revelan la formación de asimetrías como resultado de la interferencia coherente entre los dos caminos cuánticos en competencia.

Appendix A

Modeling the pulse amplitude

We use Gaussian-shaped pulses to represent the time-dependent amplitude of both single attosecond pulses (SAPs) and attosecond train pulses (APTs) throughout this thesis. The main reason to choose this kind of pulse is that we can obtain analytical expressions for both the temporal profile of the pulse and its Fourier transform, which, in addition, are both Gaussian. Using this property, we can build the spectrum of a pulse and, by calculating its inverse Fourier transform, we obtain the corresponding temporal profile. Our scheme is devised to produce APTs if the spectrum contains several harmonics and SAPs if there is only one harmonic. For the APTs, we represent each harmonic by a Gaussian function centered at the corresponding harmonic frequency ω_n and multiply all the harmonics by a spectral envelope centered at the carrier frequency of the wave ω_0. With the addition of the spectral phase $\Phi(\omega)$ the resulting Fourier transform of the amplitude of the vector potential reads as follows:

$$\tilde{A}(\omega) = \mathcal{F}\left[A(t)\right](\omega) = \mathcal{N} \sum_{\substack{n=1 \\ n \text{ odd}}}^{N_h} \Big[F_{\text{env}}(\omega-\omega_0) g_n(\omega-\omega_n) \exp\left(-i\Phi(\omega-\omega_0)\right) + F_{\text{env}}(\omega+\omega_0) g_n(\omega+\omega_n) \exp\left(i\Phi(\omega+\omega_0)\right) \Big] \quad \text{(A.1)}$$

with

$$F_{\text{env}}(\omega) = \exp\left(-\frac{\omega^2}{2\sigma_{\omega e}^2}\right) \quad \text{(A.2a)}$$

$$g_n(\omega) = \exp\left(-\frac{\omega^2}{2\sigma_{\omega h}^2} \mp s_h i \frac{\pi}{2}\right) \quad \text{(A.2b)}$$

$$\Phi(\omega) = \phi_0 + \phi_1 \omega \pm \frac{1}{2}\phi_2 \omega^2. \quad \text{(A.2c)}$$

where $\mathcal{N}$ is a normalization constant, $\sigma_{\omega e}$ is the width of the spectral envelope, $\sigma_{\omega h}$ is the width of each harmonic. N_h represents the number of harmonics in the spectrum, and s_h, with possible values ± 1, creates a phase difference of π between consecutive harmonics to emulate an APT obtained from HHG. This same scheme can be used to generate SAPs by simply setting to zero the components associated with each harmonic ($g_n(\omega)$. The spectral phase $\Phi(\omega)$ is defined through its Taylor series truncated at third order, which makes ϕ_0, ϕ_1, and ϕ_2 the zeroth-, first- and second-order coefficients of the expansion. To obtain a real function when performing the inverse Fourier transform of a function, it has to be hermitian ($\tilde{A}(-\omega) = \tilde{A}^*(\omega)$). For this reason, we have included positive- and negative-frequency components in

the above expression, although, in practice, only positive frequencies can be measured. The resulting inverse Fourier transform of $\tilde{A}(\omega)$ can be written as:

$$A(t) = \mathcal{F}^{-1}\left[\tilde{A}(\omega)\right](t) = \mathcal{N}\sum_{\substack{n=1\\ n\ \text{odd}}}^{N_h}\left[\frac{1}{\sqrt{2a^+}}\exp\left(\frac{(b_n^+ - it)^2}{4a^+} - c_n^+\right) + \frac{1}{\sqrt{2a^-}}\exp\left(\frac{(b_n^- - it)^2}{4a^-} - c_n^-\right)\right] \tag{A.3}$$

with

$$a^{\pm} = \frac{1}{2\sigma_{\omega e}^2} + \frac{1}{2\sigma_{\omega h}^2} \pm i\frac{\phi_2}{2} \tag{A.4a}$$

$$b_n^{\pm} = \frac{\omega_0}{\sigma_{\omega e}^2} \pm \frac{\omega_n}{\sigma_{\omega h}^2} \mp i(\phi_1 \mp \phi_2\omega_0) \tag{A.4b}$$

$$c_n^{\pm} = \frac{\omega_0^2}{2\sigma_{\omega e}^2} + \frac{\omega_n^2}{2\sigma_{\omega h}^2} \pm i(\mp s_h\frac{\pi}{2} + \phi_0 \mp \phi_1\omega_0 + \frac{1}{2}\phi_2\omega_0^2) \tag{A.4c}$$

Thanks to the Fourier transform properties, and especially the Fourier transform of Gaussian functions, we can manipulate the temporal profile of the pulse by modifying its spectral properties. In figure A.1 we show the temporal profile of an APT with its corresponding Fourier transform, were we depict the relationship between the widths of the harmonics ($\sigma_{\omega h}$) and the spectral envelope ($\sigma_{\omega e}$), with the widths of the temporal envelope ($\sigma_{te} = \sigma_{\omega h}^{-1}$) and the individual pulses ($\sigma_{tp} = \sigma_{\omega e}^{-1}$) respectively.

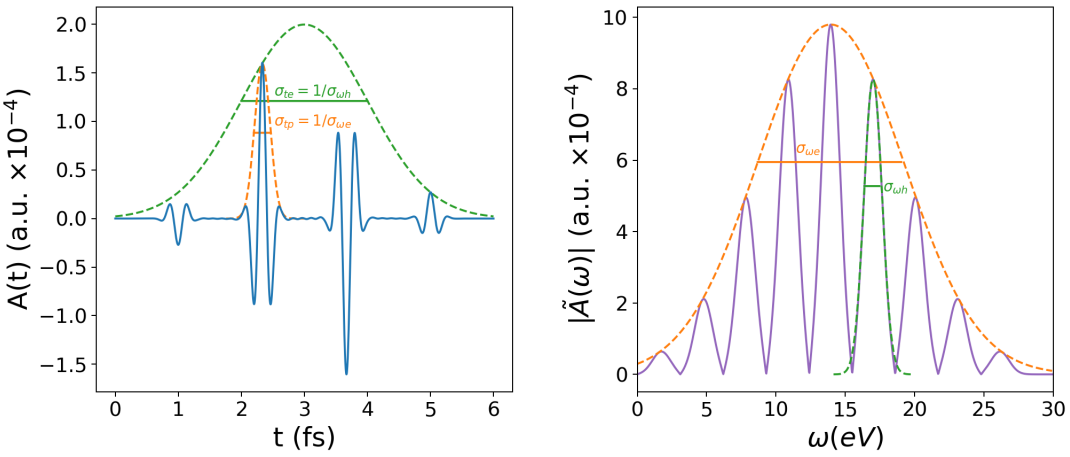

FIGURE A.1 – Temporal profile (left panel) and absolute value of the Fourier transform (right panel) of the vector potential of an APT. The Gaussian functions plotted show the relationship between the spectral envelope and the width of each individual pulse (in orange), and between the temporal envelope and the spectral width of each harmonic (in green).

Although Gaussian-shaped pulses tend to 0 for $t \to \pm\infty$, there will always be a non-zero value for the pulse amplitude. However, it is useful to define a pulse duration T such that:

$$\boldsymbol{A}(t) = \begin{cases} A(t)\boldsymbol{\epsilon}, & 0 < t < T \\ 0, & \text{elsewhere} \end{cases} \tag{A.5}$$

where $\boldsymbol{\epsilon}$ is the polarization vector. In this thesis we have defined the pulse duration using the width of the temporal envelope of the pulse as $T = n\sigma_{te}$ where n is any positive real number. Generally, choosing $n = 5 - 6$ is good enough for the amplitudes $A(t = 0)$ and $A(t = T)$ to be considered negligible. Nonetheless, this condition may be too loose for very intense pulses which require a more restricted criterion.

The different coefficients of the spectral phase can also be used to manipulate the temporal properties of the pulse. The zeroth-order coefficient ϕ_0 describes the absolute phase in the time domain, which can be used to control the carrier-envelope phase (CEP) of the pulse. The first-order term ϕ_1 leads to a translation of the temporal envelope of the laser, which we use to establish delays between different pulses. Finally, the quadratic term $\frac{1}{2}\phi_2\omega^2$ also leads to a quadratic term in the temporal phase and therefore to a linearly chirped pulse.

The normalization constant $\mathcal{N}$ that appears in equations A.1 and A.3 is related to the intensity of the pulse. In our scheme, we choose this normalization constant to define the peak amplitude of the vector potential, which is related with the pulse intensity by the following identity:

$$E_0 = A_0\omega = \sqrt{\frac{I}{I_0}} \tag{A.6}$$

where E_0 is the field amplitude, A_0 is the vector potential amplitude, ω is the carrier frequency, I is the intensity in units of W/cm^2, and $I_0 = 3.5095 \times 10^{16}$ W/cm^2 is the atomic unit of intensity. The relationship between the vector potential and the electric field has already been defined in equation 2.9 from Chapter 2.

$$\boldsymbol{E} = -\frac{\partial \boldsymbol{A}}{\partial t} \tag{A.7}$$

Bibliography

[1] Hentschel, M. *et al.* Attosecond metrology. *Nature* **414**, 509–513 (2001). URL http://www.nature.com/articles/35107000.

[2] Paul, P. M. Observation of a Train of Attosecond Pulses from High Harmonic Generation. *Science* **292**, 1689–1692 (2001). URL https://www.sciencemag.org/lookup/doi/10.1126/science.1059413.

[3] Sansone, G. *et al.* Isolated Single-Cycle Attosecond Pulses. *Science* **314**, 443–446 (2006). URL https://www.sciencemag.org/lookup/doi/10.1126/science.1132838.

[4] Gaumnitz, T. *et al.* Streaking of 43-attosecond soft-X-ray pulses generated by a passively CEP-stable mid-infrared driver. *Opt. Express* **25**, 27506 (2017). URL https://www.osapublishing.org/abstract.cfm?URI=oe-25-22-27506.

[5] Eppink, A. T. J. B. & Parker, D. H. Velocity map imaging of ions and electrons using electrostatic lenses: Application in photoelectron and photofragment ion imaging of molecular oxygen. *Review of Scientific Instruments* **68**, 3477–3484 (1997). URL https://aip.scitation.org/doi/10.1063/1.1148310.

[6] Dörner, R. *et al.* Cold target recoil ion momentum spectroscopy: a 'momentum microscope' to view atomic collision dynamics. *Physics Reports* **330**, 95 – 192 (2000). URL http://www.sciencedirect.com/science/article/pii/S037015739900109X.

[7] Schultze, M. *et al.* Delay in Photoemission. *Science* **328**, 1658–1662 (2010). URL https://www.sciencemag.org/lookup/doi/10.1126/science.1189401.

[8] Drescher, M. *et al.* Time-resolved atomic inner-shell spectroscopy. *Nature* **419**, 803–807 (2002). URL http://www.nature.com/articles/nature01143.

[9] Nisoli, M., Decleva, P., Calegari, F., Palacios, A. & Martín, F. Attosecond Electron Dynamics in Molecules. *Chem. Rev.* **117**, 10760–10825 (2017). URL https://pubs.acs.org/doi/10.1021/acs.chemrev.6b00453.

[10] Siu, W. *et al.* Attosecond control of dissociative ionization of O_3 molecules. *Phys. Rev. A* **84**, 063412 (2011). URL https://link.aps.org/doi/10.1103/PhysRevA.84.063412.

[11] Nagaya, K. *et al.* Ultrafast Dynamics of a Nucleobase Analogue Illuminated by a Short Intense X-ray Free Electron Laser Pulse. *Phys. Rev. X* **6**, 021035 (2016). URL https://link.aps.org/doi/10.1103/PhysRevX.6.021035.

[12] Kuleff, A. I., Breidbach, J. & Cederbaum, L. S. Multielectron wave-packet propagation: General theory and application. *J. Chem. Phys.* **123**, 044111 (2005). URL http://aip.scitation.org/doi/10.1063/1.1961341.

[13] Calegari, F. *et al.* Ultrafast electron dynamics in phenylalanine initiated by attosecond pulses. *Science* **346**, 336–339 (2014). URL https://www.sciencemag.org/lookup/doi/10.1126/science.1254061.

[14] Carpeggiani, P. A. *et al.* Disclosing intrinsic molecular dynamics on the 1-fs scale through extreme-ultraviolet pump-probe measurements. *Phys. Rev. A* **89**, 023420 (2014). URL https://link.aps.org/doi/10.1103/PhysRevA.89.023420.

[15] González-Castrillo, A., Palacios, A., Bachau, H. & Martín, F. Clocking Ultrafast Wave Packet Dynamics in Molecules through UV-Induced Symmetry Breaking. *Phys. Rev. Lett.* **108**, 063009 (2012). URL https://link.aps.org/doi/10.1103/PhysRevLett.108.063009.

[16] Singh, K. P. *et al.* Control of electron localization in deuterium molecular ions using an attosecond pulse train and a many-cycle infrared pulse. *Phys. Rev. Lett.* **104**, 1–4 (2010). URL https://link.aps.org/doi/10.1103/PhysRevLett.104.023001.

[17] Sansone, G. *et al.* Electron localization following attosecond molecular photoionization. *Nature* **465**, 763–766 (2010). URL http://www.nature.com/articles/nature09084.

[18] Ergler, T. *et al.* Quantum-phase resolved mapping of ground-state vibrational d_2 wave packets via selective depletion in intense laser pulses. *Phys. Rev. Lett.* **97**, 103004 (2006). URL https://link.aps.org/doi/10.1103/PhysRevLett.97.103004.

[19] Corkum, P. B. Plasma perspective on strong field multiphoton ionization. *Phys. Rev. Lett.* **71**, 1994–1997 (1993). URL https://link.aps.org/doi/10.1103/PhysRevLett.71.1994.

[20] Hemsing, E., Stupakov, G., Xiang, D. & Zholents, A. Beam by design: Laser manipulation of electrons in modern accelerators. *Rev. Mod. Phys.* **86**, 897–941 (2014). URL https://link.aps.org/doi/10.1103/RevModPhys.86.897.

[21] Duris, J. *et al.* Tunable isolated attosecond X-ray pulses with gigawatt peak power from a free-electron laser. *Nat. Photonics* **14**, 30–36 (2020). URL http://www.nature.com/articles/s41566-019-0549-5. 1906.10649.

[22] Doumy, G. *et al.* Nonlinear Atomic Response to Intense Ultrashort X Rays. *Phys. Rev. Lett.* **106**, 083002 (2011). URL https://link.aps.org/doi/10.1103/PhysRevLett.106.083002.

[23] Fuchs, M. *et al.* Anomalous nonlinear X-ray Compton scattering. *Nat. Phys.* **11**, 964–970 (2015). URL http://www.nature.com/articles/nphys3452.

[24] Young, L. *et al.* Roadmap of ultrafast X-ray atomic and molecular physics. *J. Phys. B At. Mol. Opt. Phys.* **51**, 032003 (2018). URL https://iopscience.iop.org/article/10.1088/1361-6455/aa9735.

[25] Florescu, V., Budriga, O. & Bachau, H. Two-photon above-threshold ionization of hydrogen over the photon energy range from 15 eV to 50 keV. *Phys. Rev. A* **84**, 033425 (2011). URL https://link.aps.org/doi/10.1103/PhysRevA.84.033425.

[26] Kircher, M. *et al.* Kinematically complete experimental study of Compton scattering at helium atoms near the threshold. *Nat. Phys.* **16**, 756–760 (2020). URL http://www.nature.com/articles/s41567-020-0880-2.

[27] Reiss, H. R. Dipole-approximation magnetic fields in strong laser beams. *Phys. Rev. A* **63**, 013409 (2000). URL https://link.aps.org/doi/10.1103/PhysRevA.63.013409.

[28] Wang, M.-X., Chen, S.-G., Liang, H. & Peng, L.-Y. Review on non-dipole effects in ionization and harmonic generation of atoms and molecules. *Chinese Phys. B* **29**, 013302 (2020). URL https://iopscience.iop.org/article/10.1088/1674-1056/ab5c10.

[29] Pérez-Torres, J. F. *et al.* Circular dichroism in molecular-frame photoelectron angular distributions in the dissociative photoionization of H_2 and D_2 molecules. *Phys. Rev. A* **90**, 043417 (2014). URL https://link.aps.org/doi/10.1103/PhysRevA.90.043417.

[30] Palacios, A., Gonzalez-Castrillo, A. & Martin, F. Molecular interferometer to decode attosecond electron-nuclear dynamics. *Proc. Natl. Acad. Sci.* **111**, 3973–3978 (2014). URL http://www.pnas.org/cgi/doi/10.1073/pnas.1316762111.

[31] Palacios, A., Rivière, P., González-Castrillo, A. & Martín, F. XUV Lasers for Ultrafast Electronic Control in H_2. In *Ultrafast Phenom. Mol. Sci.*, vol. 107, 25–48 (2014). URL http://link.springer.com/10.1007/978-3-319-02051-8_2.

[32] Ranitovic, P. *et al.* Attosecond vacuum UV coherent control of molecular dynamics. *Proc. Natl. Acad. Sci.* **111**, 912–917 (2014). URL http://www.pnas.org/cgi/doi/10.1073/pnas.1321999111. 1401.0021.

[33] Bachau, H., Cormier, E., Decleva, P., Hansen, J. E. & Martín, F. Applications of B-splines in atomic and molecular physics. *Reports Prog. Phys.* **64**, 1815–1943 (2001). URL https://iopscience.iop.org/article/10.1088/0034-4885/64/12/205.

[34] Hunter, G. & Pritchard, H. O. Born-Oppenheimer Separation for Three-Particle Systems. II. Two-Center Wavefunctions. *J. Chem. Phys.* **46**, 2146–2152 (1967). URL http://aip.scitation.org/doi/10.1063/1.1841016.

[35] Coulson, C. A. & Joseph, A. A constant of the motion for the two-centre Kepler problem. *Int. J. Quantum Chem.* **1**, 337–347 (1967). URL https://onlinelibrary.wiley.com/doi/10.1002/qua.560010405.

[36] Salin, A. Calculation of wave-functions and collision matrix elements for one-electron diatomic molecules. *Comput. Phys. Commun.* **14**, 121–132 (1978). URL https://linkinghub.elsevier.com/retrieve/pii/0010465578900553.

[37] Power, J. D. Fixed nuclei two-centre problem in quantum mechanics. *Philos. Trans. R. Soc. London. Ser. A, Math. Phys. Sci.* **274**, 663–697 (1973). URL https://royalsocietypublishing.org/doi/10.1098/rsta.1973.0079.

[38] Martín, F. Ionization and dissociation using B-splines: photoionization of the hydrogen molecule. *J. Phys. B At. Mol. Opt. Phys.* **32**, R197–R231 (1999). URL https://iopscience.iop.org/article/10.1088/0953-4075/32/16/201.

[39] Palacios, A., Bachau, H. & Martín, F. Resonant effects in the Coulomb explosion of H_2^+ by ultrashort laser pulses. *J. Phys. B At. Mol. Opt. Phys.* **38**, L99–L105 (2005). URL https://iopscience.iop.org/article/10.1088/0953-4075/38/6/L03.

[40] R., J. & de Boor, C. A Practical Guide to Splines. *Math. Comput.* **34**, 325 (1980). URL https://www.jstor.org/stable/2006241?origin=crossref.

[41] Froese-Fischer, C. *The Hartree-Fock method for atoms : a numerical approach* (Wiley, New York, 1977).

[42] Feshbach, H. Unified theory of nuclear reactions. *Ann. Phys. (N. Y).* **5**, 357–390 (1958). URL https://linkinghub.elsevier.com/retrieve/pii/0003491658900071.

[43] Feshbach, H. A unified theory of nuclear reactions. II. *Ann. Phys. (N. Y).* **19**, 287–313 (1962). URL https://linkinghub.elsevier.com/retrieve/pii/000349166290221X.

[44] O'Malley, T. F. Theory of Dissociative Attachment. *Phys. Rev.* **150**, 14–29 (1966). URL https://link.aps.org/doi/10.1103/PhysRev.150.14.

[45] Bardsley, J. N. Configuration interaction in the continuum states of molecules. *J. Phys. B At. Mol. Phys.* **1**, 303 (1968). URL https://iopscience.iop.org/article/10.1088/0022-3700/1/3/303.

[46] Hazi, A. U., Rescigno, T. N. & Kurilla, M. Cross sections for resonant vibrational excitation of N_2 by electron impact. *Phys. Rev. A* **23**, 1089–1099 (1981). URL https://link.aps.org/doi/10.1103/PhysRevA.23.1089.

[47] Cortes, M. & Martin, F. Multichannel close-coupling method with $\mathcal{L}^2$-integrable bases. *J. Phys. B At. Mol. Opt. Phys.* **27**, 5741–5760 (1994). URL https://iopscience.iop.org/article/10.1088/0953-4075/27/23/017.

[48] Martín, F. *et al.* Single photon-induced symmetry breaking of H2 dissociation. *Science* **315**, 629–633 (2007). URL http://www.ncbi.nlm.nih.gov/pubmed/17272717.

[49] Palacios, A., Sanz-Vicario, J. L. & Martín, F. Theoretical methods for attosecond electron and nuclear dynamics: applications to the H_2 molecule. *J. Phys. B At. Mol. Opt. Phys.* **48**, 242001 (2015). URL https://iopscience.iop.org/article/10.1088/0953-4075/48/24/242001.

[50] Starace, A. F. Behavior of partial cross sections and branching ratios in the neighborhood of a resonance. *Phys. Rev. A* **16**, 231–242 (1977). URL https://link.aps.org/doi/10.1103/PhysRevA.16.231.

[51] Taylor, J. R. *Scattering Theory: The quantum Theory on Nonrelativistic Collisions* (Wiley, New York, 1972).

[52] Dill, D. & Dehmer, J. L. Electron-molecule scattering and molecular photoionization using the multiple-scattering method. *J. Chem. Phys.* **61**, 692–699 (1974). URL http://aip.scitation.org/doi/10.1063/1.1681947.

[53] Cormier, E., Bachau, H. & Zhang, J. Discretization techniques applied to the study of multiphoton excitation of resonances in helium. *J. Phys. B At. Mol. Opt. Phys.* **26**, 4449–4463 (1993). URL https://iopscience.iop.org/article/10.1088/0953-4075/26/23/016.

[54] Macías, A., Martín, F., Riera, A. & Yáñez, M. A practical solution to the "unknown normalization" problem. *Int. J. Quantum Chem.* **33**, 279–300 (1988). URL http://doi.wiley.com/10.1002/qua.560330404.

[55] Park, H. & Zare, R. N. Molecular-orbital decomposition of the ionization continuum for a diatomic molecule by angle- and energy-resolved photoelectron spectroscopy. I. Formalism. *J. Chem. Phys.* **104**, 4554–4567 (1996). URL http://aip.scitation.org/doi/10.1063/1.471204.

[56] Fano, U. & Rau, A. *Atomic Collisions and Spectra* (Academic Press, Orlando, Florida, 1986).

[57] Decleva, P., Lisini, A. & Venuti, M. Multichannel continuum states by a least-squares approach in a spline basis: application to He and H^- photoionization. *J. Phys. B At. Mol. Opt. Phys.* **27**, 4867–4889 (1994). URL https://iopscience.iop.org/article/10.1088/0953-4075/27/20/007.

[58] Stener, M. & Decleva, P. Photoionization of CH_4, SiH_4, BH_3 and AlH_3 by the B-spline one-centre expansion density functional method. *J. Electron Spectros. Relat. Phenomena* **104**, 135–144 (1999). URL https://linkinghub.elsevier.com/retrieve/pii/S0368204899000109.

[59] Sánchez, I. & Martn, F. Photoionization of He above the n=2 threshold. *Phys. Rev. A* **44**, 7318–7334 (1991). URL https://link.aps.org/doi/10.1103/PhysRevA.44.7318.

[60] Sánchez, I. & Martín, F. Photoionization of He above the N=2 threshold. II. Angular distribution of photoelectrons and asymmetry parameter. *Phys. Rev. A* **45**, 4468–4475 (1992). URL https://link.aps.org/doi/10.1103/PhysRevA.45.4468.

[61] Martín, F. Completely $\mathcal{L}^2$-integrable method for strong-coupling multichannel photoionization: Photoelectron emission of He between the N=3 and 4 thresholds. *Phys. Rev. A* **48**, 331–337 (1993). URL https://link.aps.org/doi/10.1103/PhysRevA.48.331.

[62] Sakurai, J. J. *Advanced Quantum Mechanics* (Pearson Education, Reading, Mass., 1967).

[63] Heitler, W. *The Quantum Theory of Radiation* (Dover Publ., New York, 1984).

[64] Orfanos, I. *et al.* Attosecond pulse metrology. *APL Photonics* **4**, 080901 (2019). URL http://aip.scitation.org/doi/10.1063/1.5086773.

[65] Hädrich, S. *et al.* High photon flux table-top coherent extreme-ultraviolet source. *Nat. Photonics* **8**, 779–783 (2014). URL http://www.nature.com/articles/nphoton.2014.214. 1403.4631.

[66] Feynman, R. P., Leighton, R. B. & Sands, M. L. *The Feynman lectures on physics (Vol. 2)* (Basic Books, New York, 2015).

[67] Aharonov, Y. & Bohm, D. Significance of Electromagnetic Potentials in the Quantum Theory. *Phys. Rev.* **115**, 485–491 (1959). URL https://link.aps.org/doi/10.1103/PhysRev.115.485.

[68] Cormier, E. & Lambropoulos, P. Optimal gauge and gauge invariance in non-perturbative time-dependent calculation of above-threshold ionization. *J. Phys. B At. Mol. Opt. Phys.* **29**, 1667–1680 (1996). URL https://iopscience.iop.org/article/10.1088/0953-4075/29/9/013.

[69] Hau-Riege, S. P. *Nonrelativistic Quantum X-Ray Physics* (Wiley-VCH Verlag GmbH Co. KGaA, Weinheim, Germany, 2014). URL http://doi.wiley.com/10.1002/9783527664498.

[70] Barut, A. O. *Quantum Electrodynamics and Quantum Optics* (Springer US, Boston, MA, 1984). URL http://link.springer.com/10.1007/978-1-4613-2783-7.

[71] Shakeshaft, R. Multiphoton ionization of an atom; the choice of gauge. *Z. Phys. D. Atom Mol. Cl.* **8**, 47–50 (1988). URL http://link.springer.com/10.1007/BF01384522.

[72] Reiss, H. R. The tunnelling model of laser-induced ionization and its failure at low frequencies. *J. Phys. B At. Mol. Opt. Phys.* **47**, 204006 (2014). URL https://iopscience.iop.org/article/10.1088/0953-4075/47/20/204006. 1403.0568.

[73] Ludwig, A. *et al.* Breakdown of the Dipole Approximation in Strong-Field Ionization. *Phys. Rev. Lett.* **113**, 243001 (2014). URL https://link.aps.org/doi/10.1103/PhysRevLett.113.243001. 1408.2336.

[74] Cohen-Tannoudji, C., Diu, B. & Laloë, F. *Quantum Mechanics (Vol. 2)* (New York Wiley, New York, 1991).

[75] Jackson, J. D. *Classical Electrodynamics* (Wiley, Chichester, 1999).

[76] Bachau, H., Dondera, M. & Florescu, V. Stimulated Compton Scattering in Two-Color Ionization of Hydrogen with keV Electromagnetic Fields. *Phys. Rev. Lett.* **112**, 073001 (2014). URL https://link.aps.org/doi/10.1103/PhysRevLett.112.073001.

[77] Dondera, M. & Bachau, H. Exploring above-threshold ionization of hydrogen in an intense X-ray laser field through nonperturbative calculations. *Phys. Rev. A* **85**, 013423 (2012). URL https://link.aps.org/doi/10.1103/PhysRevA.85.013423.

[78] Silver, B. & Silver, F. *Irreducible Tensor Methods: An Introduction for Chemists*. Mathematics in Science and Engineering (Academic Press, New York, 1976). URL https://books.google.es/books?id=B4EpAQAAMAAJ.

[79] Brandsen, B. H. & Joachain, C. J. *Physics of Atoms and Molecules* (Prentice Hall, Harlow, 2010). URL https://iopscience.iop.org/article/10.1088/0031-9112/24/10/032.

[80] Johnsson, P., Mauritsson, J., Remetter, T., L'Huillier, A. & Schafer, K. J. Attosecond Control of Ionization by Wave-Packet Interference. *Phys. Rev. Lett.* **99**, 233001 (2007). URL https://link.aps.org/doi/10.1103/PhysRevLett.99.233001.

[81] Sturm, F. P. *et al.* Mapping and controlling ultrafast dynamics of highly excited H_2 molecules by VUV-IR pump-probe schemes. *Phys. Rev. A* **95**, 012501 (2017). URL https://link.aps.org/doi/10.1103/PhysRevA.95.012501.

[82] Krausz, F. & Ivanov, M. Attosecond physics. *Rev. Mod. Phys.* **81**, 163–234 (2009). URL https://link.aps.org/doi/10.1103/RevModPhys.81.163.

[83] Brumer, P. & Shapiro, M. Control of unimolecular reactions using coherent light. *Chem. Phys. Lett.* **126**, 541–546 (1986). URL https://linkinghub.elsevier.com/retrieve/pii/S0009261486801713.

[84] Brumer, P. & Shapiro, M. Laser Control of Molecular Processes. *Annu. Rev. Phys. Chem.* **43**, 257–282 (1992). URL http://www.annualreviews.org/doi/10.1146/annurev.pc.43.100192.001353.

[85] Sturm, F. P. *et al.* Time resolved 3D momentum imaging of ultrafast dynamics by coherent VUV-XUV radiation. *Rev. Sci. Instrum.* **87**, 063110 (2016). URL http://aip.scitation.org/doi/10.1063/1.4953441.

[86] González-Castrillo, A., Palacios, A., Catoire, F., Bachau, H. & Martín, F. Reproducibility of Observables and Coherent Control in Molecular Photoionization: From Continuous Wave to Ultrashort Pulsed Radiation. *J. Phys. Chem. A* **116**, 2704–2712 (2012). URL https://pubs.acs.org/doi/10.1021/jp2078049.

[87] Sánchez, J. & Campos, J. Radiative lifetime measurements for H_2 molecule. *J. Phys.* **49**, 445–449 (1988). URL http://www.edpsciences.org/10.1051/jphys:01988004903044500.

[88] Eckhardt, G. *et al.* Stimulated Raman Scattering From Organic Liquids. *Phys. Rev. Lett.* **9**, 455–457 (1962). URL https://link.aps.org/doi/10.1103/PhysRevLett.9.455.

[89] Hellwarth, R. W. Theory of Stimulated Raman Scattering. *Phys. Rev.* **130**, 1850–1852 (1963). URL https://link.aps.org/doi/10.1103/PhysRev.130.1850.

[90] Saar, B. G. *et al.* Video-Rate Molecular Imaging in Vivo with Stimulated Raman Scattering. *Science* **330**, 1368–1370 (2010). URL https://www.sciencemag.org/lookup/doi/10.1126/science.1197236.

[91] Batignani, G. *et al.* Electronic resonances in broadband stimulated Raman spectroscopy. *Sci. Rep.* **6**, 18445 (2016). URL http://www.nature.com/articles/srep18445.

[92] Prince, R. C., Frontiera, R. R. & Potma, E. O. Stimulated Raman Scattering: From Bulk to Nano. *Chem. Rev.* **117**, 5070–5094 (2017). URL https://pubs.acs.org/doi/10.1021/acs.chemrev.6b00545.

[93] Biggs, J. D., Zhang, Y., Healion, D. & Mukamel, S. Multidimensional X-ray spectroscopy of valence and core excitations in cysteine. *J. Chem. Phys.* **138**, 144303 (2013). URL http://aip.scitation.org/doi/10.1063/1.4799266.

[94] Miyabe, S. & Bucksbaum, P. Transient Impulsive Electronic Raman Redistribution. *Phys. Rev. Lett.* **114**, 143005 (2015). URL https://link.aps.org/doi/10.1103/PhysRevLett.114.143005.

[95] Kramers, H. A. & Heisenberg, W. Über die Streuung von Strahlung durch Atome. *Z. Phys.* **31**, 681–708 (1925). URL http://link.springer.com/10.1007/BF02980624.

[96] Waller, I. Über eine verallgemeinerte Streuungsformel. *Z. Phys.* **51**, 213–231 (1928). URL http://link.springer.com/10.1007/BF01343197.

[97] Dondera, M., Florescu, V. & Bachau, H. Stimulated Raman scattering of an ultrashort XUV radiation pulse by a hydrogen atom. *Phys. Rev. A* **95**, 023417 (2017). URL https://link.aps.org/doi/10.1103/PhysRevA.95.023417.

[98] Georges, A. & Lambropoulos, P. Aspects of Resonant Multiphoton Processes. In *Adv. Electron. Electron Phys.*, vol. 54, 191–240 (1980). URL https://linkinghub.elsevier.com/retrieve/pii/S0065253908600992.

[99] Gavrila, M. Compton Scattering by K-Shell Electrons. I. Nonrelativistic Theory with Retardation. *Phys. Rev. A* **6**, 1348–1359 (1972). URL https://link.aps.org/doi/10.1103/PhysRevA.6.1348.

[100] Fojón, O. A., Fernández, J., Palacios, A., Rivarola, R. D. & Martín, F. Interference effects in H_2 photoionization at high energies. *J. Phys. B At. Mol. Opt. Phys.* **37**, 3035–3042 (2004). URL https://iopscience.iop.org/article/10.1088/0953-4075/37/15/003.

[101] Samson, J. A. R. & Haddad, G. N. Total photoabsorption cross sections of H2 from 18 to 113 eV. *J. Opt. Soc. Am. B* **11**, 277 (1994). URL https://www.osapublishing.org/abstract.cfm?URI=josab-11-2-277.

[102] Førre, M. & Simonsen, A. S. Nondipole ionization dynamics in atoms induced by intense XUV laser fields. *Phys. Rev. A* **90**, 053411 (2014). URL https://link.aps.org/doi/10.1103/PhysRevA.90.053411.

[103] Cormier, E. & Lambropoulos, P. Extrapolation method for the evaluation of above threshold ionization cross sections for one- and two-electron systems. *J. Phys. B At. Mol. Opt. Phys.* **28**, 5043–5055 (1995). URL https://iopscience.iop.org/article/10.1088/0953-4075/28/23/013.

[104] Compton, A. H. A Quantum Theory of the Scattering of X-rays by Light Elements. *Phys. Rev.* **21**, 483–502 (1923). URL https://link.aps.org/doi/10.1103/PhysRev.21.483.

[105] Bothe, W. & Geiger, H. Ein Weg zur experimentellen Nachprüfung der Theorie von Bohr, Kramers und Slater. *Z. Phys.* **26**, 44–44 (1924). URL http://link.springer.com/10.1007/BF01327309.

[106] Cooper, M. Compton scattering and electron momentum distributions. *Adv. Phys.* **20**, 453–491 (1971). URL http://www.tandfonline.com/doi/abs/10.1080/00018737100101291.

[107] Eisenberger, P. & Platzman, P. M. Compton Scattering of X-Rays from Bound Electrons. *Phys. Rev. A* **2**, 415–423 (1970). URL https://link.aps.org/doi/10.1103/PhysRevA.2.415.

[108] Kapitza, P. L. & Dirac, P. A. M. The reflection of electrons from standing light waves. *Math. Proc. Cambridge Philos. Soc.* **29**, 297–300 (1933). URL https://www.cambridge.org/core/product/identifier/S0305004100011105/type/journal_article.

[109] Bachau, H. & Dieng, M. Compton scattering of keV photons at helium atom near the He^+(1s) threshold for small momentum transfer. *Eur. Phys. J. D* **75**, 34 (2021). URL https://doi.org/10.1140/epjd/s10053-021-00048-0http://link.springer.com/10.1140/epjd/s10053-021-00048-0.

[110] Lutman, A. A. *et al.* Experimental demonstration of femtosecond two-color x-ray free-electron lasers. *Phys. Rev. Lett.* **110**, 134801 (2013). URL https://link.aps.org/doi/10.1103/PhysRevLett.110.134801.

[111] Serkez, S. *et al.* Opportunities for Two-Color Experiments in the Soft X-ray Regime at the European XFEL. *Appl. Sci.* **10**, 2728 (2020). URL https://www.mdpi.com/2076-3417/10/8/2728.